Aus dem Neurowissenschaftlichen Forschungszentrum
der Medizinischen Fakultät Charité – Universitätsmedizin Berlin

DISSERTATION

The roles of RIM and Munc13 in the presynaptic terminal of murine hippocampal neurons

zur Erlangung des akademischen Grades
Doctor of Philosophy (PhD)

vorgelegt der Medizinischen Fakultät
Charité – Universitätsmedizin Berlin

von

Fereshteh Zarebidaki
aus Mashhad, Iran

Datum der Promotion: 26.06.2022

Contents

Abstract

Neurons communicate via chemical synapses through the exocytosis of neurotransmitter-filled vesicles at the presynaptic active zone. Before exocytosis, synaptic vesicles are recruited to the presynaptic active zone membrane and become membrane-docked by a network of presynaptic proteins. The efficiency of exocytosis is determined by molecular priming factors that reduce the energy barrier between the synaptic vesicles and the presynaptic membrane, and couple Ca^{2+} channels to the primed synaptic vesicles. Rab3 interacting molecule (RIM) is a multidomain scaffolding protein in the active zone that participates in all steps of neurotransmission. RIM tethers synaptic vesicles to the presynaptic membrane and at the same time interacts with Ca^{2+} channels to modulate their function and to recruit them to the release sites. In addition, RIM activates the core of synaptic vesicle docking and priming, Munc13. Munc13 isoforms determine the number of readily-releasable synaptic vesicles and different forms of short-term plasticity. Due to the tightly overlapping, yet partially independent functions of RIM and Munc13, the RIM's direct contribution to synapse functions is still unclear. Here, we investigated how RIM individually determines the synapse ultrastructure and function. For this purpose, we altered the expression of RIM and/or Munc13 isoforms in primary mouse hippocampal neurons and performed high-pressure freezing for electron microscopy, as well as electrophysiological recordings in autaptic cultures. We showed that RIM, independent from Munc13-1, localizes synaptic vesicles close to the AZ membrane and regulates the efficiency of synaptic vesicle release. However, both RIM and Munc13-1 contribute to synaptic vesicle docking and priming. Notably, in the absence of RIM and Munc13-1, the brain-specific isoform of Munc13-2 determines the size of the readily releasable synaptic vesicle pool at rest and after high frequency stimulation. Considering the critical role of RIM and Munc13 in different neurotransmission steps, this study deepens our understanding of how these molecules work in the presynaptic terminal to fulfill neurotransmission.

Zusammenfassung

Neuronen kommunizieren über chemische Synapsen durch den Vorgang der Exozytose, welcher die Fusion von Neurotransmittern gefüllten Vesikeln mit der präsynaptischen Membran beschreibt. Damit Vesikel mit der Membrane fusionieren können, müssen sie über ein präsynaptisches Proteinen-Netzwerk zur Membran rekrutiert und gebunden werden. Ebenfalls muss für eine effiziente Exozytose die Energiebarriere zwischen den synaptischen Vesikeln und der präsynaptischen Membran verringert werden, was durch zusätzliche „Priming"-Faktoren und die Rekrutierung von Kalzium-Kanäle geschieht. Ein wichtiges Molekül in der Rekrutierung von Vesikeln ist das Rab3-interagierende Molekül (RIM), welches Vesikel an die präsynaptische Membran bindet und gleichzeitig Kalzium-Kanälen rekrutiert. Zusätzlich steigert RIM die Rekrutierung und Anlagerung von Vesikeln an die präsynaptische Membran durch die Aktivierung des präsynaptischen Proteins Munc13. Dabei kann die Wahrscheinlichkeit der Exozytose durch die Expression verschiedener Munc13-Isoformen bestimmen werden. Aufgrund der eng überlappenden, jedoch teilweise unabhängigen Funktionen von RIM und Munc13 ist der direkte Beitrag von RIM in der Rekrutierung von Vesikeln bisher unklar. In dieser Arbeit untersuchten wir den individuellen Beitrag von RIM auf die Exozytose, indem wir den Einfluss von RIM auf die synaptische Funktion und Ultrastruktur untersuchten. Zunächst haben wir die Expression von RIM- und / oder Munc13-Isoformen in primären hippokampalen Neuronen der Maus variiert und die Veränderungen in synaptischer Struktur und Funktion mit Hilfe der Elektronenmikroskopie und Elektrophysiologie charakterisiert. Die Analyse ergab, dass RIM unabhängig von Munc13-1 synaptische Vesikel in der Nähe der AZ-Membran lokalisiert und somit die Effizienz der Freisetzung synaptischer Vesikel reguliert. Ebenfalls konnten wir Unterschiede zwischen den Munc13-Isoformen aufzeigen. Dabei ist von besonderem Interesse, dass in Abwesenheit von RIM und Munc13-1, Munc13-2 die Effizienz der Freisetzungswahrscheinlichkeit synaptischer Vesikel in Ruhe und nach Hochfrequenzstimulation bestimmt. In Anbetracht der entscheidenden Rolle von RIM und Munc13 in verschiedenen Schritten der Neurotransmitterfreisetzung vertieft diese Studie unser Verständnis wie diese Moleküle im präsynaptischen Terminal arbeiten, um effiziente Neurotransmission zu ermöglichen.

1. Introduction

The central nervous system (CNS) predominantly consists of neurons that perceive, process, and respond to the environment. A typical neuron is comprised of dendrites that arborise from the soma to receive information and an axon that extends from the soma to transfer the information to the next neuron through chemical synapses. At resting conditions, the membrane potential of a neuron is typically at -60 to -70 mV. Once a neuron receives a stimulus, the membrane undergoes depolarization and repolarization processes, known as action potential (AP). The AP propagates to the nerve terminal and causes the opening of Ca^{2+} channels in the presynaptic terminal. An inward Ca^{2+} current triggers several molecular processes that lead to neurotransmitter release.

Mechanistically, neurotransmission requires the formation of membranous vesicles that carry the respective neurotransmitter. The vesicles are then recruited to the presynaptic membrane. This process can be detected as filaments (tethers) that connect vesicles to the presynaptic membrane (Landis et al., 1988). In the next step, the vesicles "dock" at the presynaptic membrane and "prime" through a molecular mechanism which makes them "readily releasable" (Sudhof, 2004). Upon AP-driven Ca^{2+} influx, the primed vesicles fuse to the presynaptic membrane and release their content. Neurotransmitters reach the postsynaptic receptors and initiate molecular processes that depolarize the postsynaptic neuron, eliciting a postsynaptic current. Sustained release upon consecutive stimulations requires a reliable vesicle recycling process which takes place by the endocytosis of excess membrane as a source of new vesicles (Heuser and Reese, 1973). The properties, fidelity, and efficiency of neurotransmission depend on the molecular interactions that coordinate the synaptic vesicle cycle. Thus, understanding the processes that take place in the presynaptic terminal is the key to decipher neuronal behavior.

What molecular components regulate neurotransmission at the presynaptic terminal? Specific regions in the presynaptic area contain a dense protein network near to the release sites, termed as cytomatrix of the active zone (CAZ; Gundelfinger et al. (2003)). In mammals, the main proteins that comprise the CAZ, such as RIM, Munc13, RIM-binding protein (RIM-BP), α-Liprins, ELKS, Piccolo, and Bassoon, regulate the neurotransmitter release (Sudhof, 2012). Downstream of this network, soluble N-ethylmaleimide-sensitive factor attachment protein receptor (SNARE) complexes, with the help of Ca^{2+} sensors, reduce the energy barrier for the fusion of synaptic vesicles (Rizo et al., 2006). The function of CAZ proteins in conjunction with their partners can be hierarchical, redundant, exclusive, or independent (Sudhof, 2012; Brockmann et al., 2020). This complicates the understanding of each protein's contribution to different stages

of neurotransmitter release. Therefore, a comparison of single and multiple genetic ablations using the same system is required to identify the role of individual CAZ proteins in synapse.

RIM is one of the CAZ proteins that has been broadly investigated because of its multidomain structure and interconnected functions (Fig. 1). Initially, RIM was recognized as a protein that binds to small vesicle-bound Rab3A GTP molecules (Wang et al., 1997; Fukuda, 2003) to bring synaptic vesicles close to the membrane (Dulubova et al., 2005; Gracheva et al., 2008; Fernandez-Busnadiego et al., 2013). Biochemical experiments revealed that RIM recruits Ca^{2+} channels to the release sites by a direct interaction with Ca^{2+} channels and an interaction with RIM-BP which in turn also binds to Ca^{2+} channels (Han et al., 2011; Kaeser et al., 2011). Moreover, the Zinc-finger domain of RIM interacts with C2A domain of Munc13 (Betz et al., 2001), monomerizing the constitutively homodimeric Munc13 (Deng et al., 2011). As a result, RIM recruits Munc13 to the release sites (Andrews-Zwilling et al., 2006) and activates Munc13's docking and priming functions (Stevens et al., 2005; Deng et al., 2011; Camacho et al., 2017). Since the interplay of RIM and Munc13 is essential to produce the membrane-attached and fusion-competent vesicles (Augustin et al., 1999a; Bohme et al., 2016; Sakamoto et al., 2018), deletion of RIM severely impairs vesicle docking, priming, and ultimately Ca^{2+}-dependent fusion (Deng et al., 2011; Kaeser, 2011). The interconnected phenotypes of RIM and Munc13, hinder our understandings of Munc13-independent effects of RIM on synapse functions.

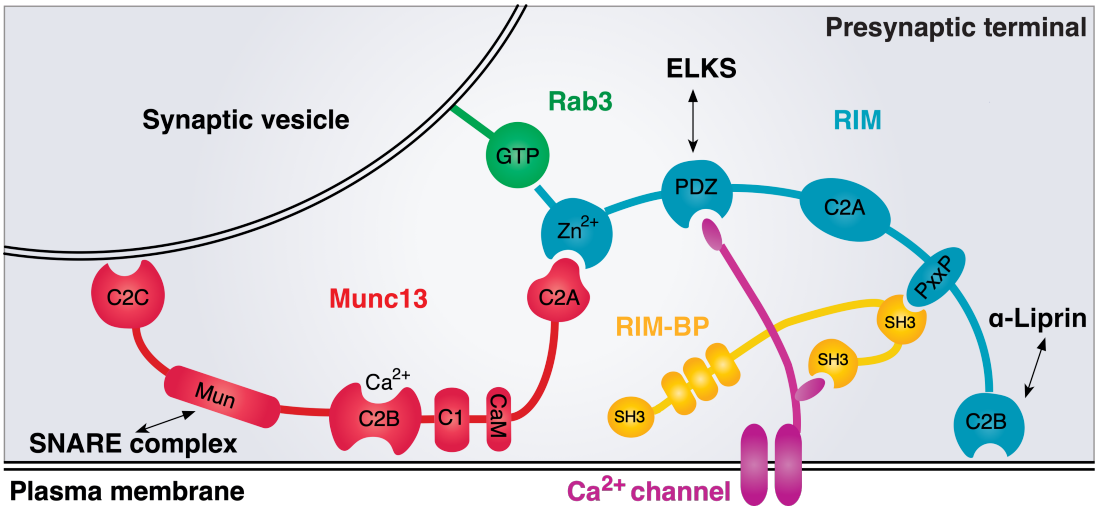

Figure 1. Domain structure and interaction sites of key active zone proteins: RIM, Munc13, and RIM-BP. This complex is important to sustain AZ assembly, vesicle priming, AP-evoked release, Ca^{2+} channel recruitment, Ca^{2+} influx, vesicular release probability, and short-term plasticity.

It is important to consider that some Munc13 isoforms may act on vesicle priming independent from RIM. There are two main isoforms of Munc13 in mammalian cerebrum, Munc13-1 and Munc13-2 (Augustin et al., 1999b). Both Munc13-1 and a ubiquitously expressed

splice variant of Munc13-2 (ubMunc13-2) are capable of binding to RIM. However, only Munc13-1 operates as the most abundant isoform in the brain (Augustin et al., 1999b). On the other hand, the brain specific splice variant of Munc13-2 (bMunc13-2), the second most abundant isoform, is constitutively monomerized, which makes it eligible to prime vesicles independent of RIM (Kawabe et al., 2017). Nevertheless, despite the well characterized structure of Munc13s, their relative contribution to synaptic function, in respect to their putative interaction with RIM, is still enigmatic.

1.1 Objectives

Due to the complex multiprotein interactions in the presynaptic AZ, the individual role of RIM in neurotransmission has been masked, which makes it difficult to distinguish the direct influence of RIM on the performance of the presynaptic AZ function. Since the functions of RIM and Munc13 are interconnected, we aim to identify the roles of RIM that are mediated independent of Munc13. First, we explore the relative contribution of the RIM-dependent and -independent Munc13 isoforms to synapse functions. For this purpose, we rescue Munc13 isoforms in constitutive knockout neurons lacking both Munc13-1 and Munc13-2 (Munc13-1/2 DKO) and perform electrophysiological recordings. Second, we take advantage of a conditional double knockout (cDKO) mouse line in which the presynaptic isoforms of RIM, RIM1 and RIM2, can be deleted by Cre-recombinase (Kaeser et al., 2011). In this neuronal system, we remove Munc13-1 with the knockdown (KD) approach either in the presence of RIM1/2 or in RIM1/2 cDKO neurons. Using high-pressure freezing for electron microscopy (EM) and electrophysiological recordings, we investigate the ultrastructural and electrophysiological impact of RIM1/2 and/or Munc13-1 deletions. This approach enables us to deconvolve the role of RIM1/2 and Munc13-1 in the synapse, which has not been feasible to identify by comparing single knockout lines.

2. Materials and Methods

2.1 Animals and maintenance

Animal Welfare Committee of Charité—Universitätsmedizin and the Berlin state government agency for Health and Social Services approved all animal experiments and maintenance (license no. T 0220/09). *RIM1^{flox}/RIM2^{flox}* mice (called RIM1/2^{flox}) were generated from crossing C57BL6/N mice with *RIM1^{flox}/ RIM2^{flox} /RBP1^{flox}/RBP2^{flox}* mouse line (a gift from Prof. Thomas C. Südhof laboratory (Acuna et al., 2016)). For the experiments, RIM1/2^{flox} mice were used at postnatal (P) days 0 to 2. In addition, *Munc13-1$^{-/-}$/Munc13-2$^{-/-}$* (called Munc13-1/2 double knockout (DKO)) embryos were produced by interbreeding *Munc13-1$^{+/-}$/Munc13-2$^{-/-}$* mice on a FVB/N background (Camacho et al., 2017). Since the Munc13-1/2 DKO animals die immediately

after birth, the embryos at day 18 (E18) were used for the experiments. For the embryonic culture preparation, first the pregnant mice were anaesthetized to perform cervical dislocation and second, with the cesarian method, embryos were extracted to be used in the experiments. In none of the experiments the sex of animals was distinguished.

2.2 Cell culture

2.2.1 Astrocyte preparation

Prior to the astrocyte preparation, coverslips were alkalized (with 1N NaOH) and sterilized. For the mass cultures, the entire surface of the coverslips (sapphires for EM experiments) was covered with coating a solution containing acetic acid, collagen (ThermoFischer Scientific), and Poly-D lysine (Sigma Aldrich). For the micro-islands, the entire coverslips were covered with 0.15% agarose and the coating solution was printed onto the agarose-coated 30 mm coverslips with a custom-built stamp to obtain 200 μm diameter micro-islands.

Two weeks before the neuronal seeding, astrocytes for micro-islands and continental feeder layers were generated from cortices of C57BL6/N mice at P0-P1. Briefly, the newborn mice were decapitated and the brain was cleaned from meninges. Once the two cortical hemispheres were dissected, they were digested in 0.05% Trypsin (Gibco 25-300-054) for 18 min. Subsequently, the cortices were triturated and cultured for 1-2 weeks in T75 flasks containing Dulbecco's Modified Eagle's Medium (DMEM). By the end of the second week, the astrocytes were vortexed to detach from the flask, washed with phosphate buffer saline (PBS), and dissociated with 0.05% Trypsin. Finally, the astrocytes were triturated and counted. 50,000 cells for 6-well microdot plates (electrophysiology and immunocytochemistry), 75,000 cells for 6-well continental plates (Western blot), and 47,000 cell for 12-well continental plates with sapphires (EM experiments) were added to the media on the coated coverslips. After 7 days, FUDR solution (8 μM 5-fluoro-2`-deoxyuridine (Sigma F0503) and 20 μM Uridine) was added to the plates to stop proliferation. Prior to neuronal seeding, media was exchanged with Neurobasal-A medium (NBA) supplemented with B21, Glutamax, 50 IU/ml Penicillin, and 50 μg/ml Streptomycin.

2.2.2 Neuronal cultures

The neuronal cultures were prepared from the hippocampi of the postnatal or embryonic mice (refer to section 2.1). Immediately following the hippocampal dissection, the cells were digested with the 25 U/ml papain (Worthington) for 50-60 min. To isolate the neurons, the samples were gently triturated, and the neurons were counted. For the autaptic cultures, 3500 neurons were seeded on astrocytic micro-islands. For the mass cultures and sapphires, 100,000 cells were seeded on the astrocytic feeder layers.

2.3 Lentiviral particles and infection

The lentiviral constructs were provided by the viral core facility of the Charité – Universitätsmedizin Berlin. All hippocampal neurons were transduced on days *in vitro* (DIV) 1-2. To provide RIM1/2 control and conditional double knockout (cDKO), the RIM1/2^{flox} neurons were infected with lentiviral particles expressing EGFP-Cre recombinase (Cre) and EGFP-inactivated-Cre recombinase (ΔCre) tagged with nuclear localization sequence (Kaeser et al., 2011). For the Munc13-1 knockdown (KD) experiments, short hairpin RNA (shRNA) target sequence (5′-GCCTGAGATCTTCGAGCTTAT-3′) was used, as it was shown to successfully remove Munc13-1 from the synapse (Deng et al., 2011). The sequence was driven by a U6 promoter and was tagged to a nuclear localization sequence and RFP. For Munc13-1/2 DKO rescue experiments, lentiviral particles containing Munc13-1 construct were generated from rat *Unc13a* (NM_022861) with some modifications (Camacho et al., 2017). Moreover, bMunc13-2 and ubMunc13-2 isoforms were generated from rat *Unc13b* transcript variant 1 (NM_022862) and rat *Unc13b* transcript variant 2 (NM_001042579), respectively. All Munc13 constructs contained a synapsin-1 promoter and were tagged with a fluorescent protein.

To generate lentiviral particles, HEK293T cells were transfected with FUGW shuttle vector (10 µg), the helper plasmids, pCMVdR8.9 (7.5 µg), and pVSV.G (5 µg) in coated T75 flasks. Subsequently, the transfected cells were incubated at 32°C for 72 h. The supernatant with the lentiviral particles were collected, purified, and stored at -80°C.

2.4 Electrophysiology

The electrophysiological recordings were performed by whole-cell voltage clamp in autaptic hippocampal neurons on DIV 14 to 20. We used autaptic cultures (Fig. 2A-B), as it provides a simple model system to study synaptic transmission without interfering inputs from network activity (Bekkers and Stevens, 1991). The recordings were performed using Clampex 10.5 software that controlled Multiclamp 700B amplifier (Molecular devices). Axon Digidata 1550 digitizer (Axon instruments) was used to collect data at 10 kHz sample rate with a low-pass Bessel filter at 3 KHz. For recordings, coverslips were transferred into a chamber with extracellular solution containing (in mM): 140 NaCl, 2.4 KCl, 10 HEPES, 10 glucose, 2 $CaCl_2$ and 4 $MgCl_2$ (~300 mOsm and pH 7.4). The extracellular solution was continuously exchanged with a perfusion system. Borosilicate glass pipettes with resistance between 2.5-4.5 MΩ were pulled with a micropipette puller device (Sutter instruments). The pipettes were filled with intracellular solution containing (in mM): 136 KCl, 17.8 HEPES, 1 EGTA, 4.6 $MgCl_2$, 4 Na_2ATP, 0.3 Na_2GTP,

12 creatine phosphate and 50 U ml^{-1} phosphocreatine kinase (~300 mOsm and pH 7.4). Electrophysiological recordings were analyzed using Axograph X (Axograph Scientific).

The recordings were performed at room temperature at holding potential of -70 mV. During the recording, access resistance was compensated at 70%. Only neurons with a series resistance of <10 MΩ were kept for further analysis. The postsynaptic currents were elicited by 2 ms depolarization to 0 mV (Fig. 2C). In order to distinguish excitatory neurons from the inhibitory ones, an AMPA receptor antagonist, 2,3-dioxo-6-nitro-7-sulfamoyl-benzo[f]quinoxaline (NBQX) (Tocris Bioscience), was applied at 3 µM concentration in extracellular solution. We only recorded and analyzed excitatory neurons. Peak responses of average excitatory postsynaptic currents (EPSCs) were quantified as EPSC amplitude (Fig. 2C). To estimate the readily releasable pool (RRP) size, 500 mM sucrose was applied for 5 s in extracellular solution (Fig. 2D). The resulting transient charge was quantified to determine the RRP size (Rosenmund and Stevens, 1996). The ratio of EPSC to RRP charge defines the vesicular release probability (P_{vr}; represented in %). The RRP augmentation was assessed by calculating the ratio of the RRP charge 2 s after 10Hz stimulation at 50 APs to the baseline RRP charge.

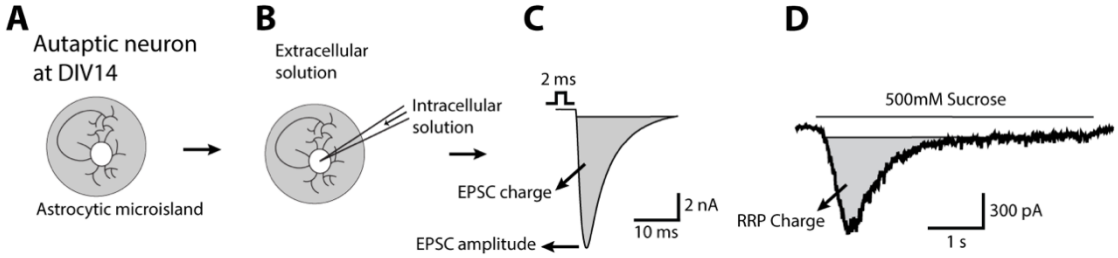

Figure 2. Electrophysiology. **A**-**B**, Schematic representation of an autaptic neuron (**A**) and the patch-clamp recording of the soma (**B**). **C**, Trace of the EPSC induced by 2 ms depolarization. **D**, Trace of Sucrose-induced postsynaptic current. **C**-**D**, gray area represents the charge.

2.5 High-pressure freezing and transmission electron microscopy

The 6 mm carbon-coated sapphire glasses containing neurons (DIV 14-16; Fig. 3A) were transferred into extracellular solution (same extracellular solution as described in section 2.4) and the experiments were performed at room temperature. Following the freezing with high-pressure freezing device (Leica EM ICE or HPM100; Fig. 3B) the sapphires were immersed in liquid nitrogen and were moved inside an AFS2 automated freeze-substitution device (Leica) programmed at -90°C (Fig. 3C). Inside the device, sapphires were transferred in cryovials with the following solution: 1% osmium tetroxide, 1% glutaraldehyde, and 1% ddH_2O in anhydrous acetone. The device was programmed for a two days protocol with a stepwise heating starting at -90°C for 4-5 h, -90°C to -20°C for 14 h, -20°C for 12 h, and -20°C to +20°C for 8 h. At the end of the program, samples were washed three times (each 15 min) in anhydrous acetone.

Subsequently, samples were treated for 1 h with 0.1% uranyl acetate to get contrast enhancement and then again were washed three times (each 15 min) in anhydrous acetone. Embedding was performed in EPON by a stepwise increase in concentration from 30% and 70%, each for 2 h, and 90% overnight. Finally, the samples were baked at 60°C for 48 h to polymerize.

The serial sectioning was performed with an ultramicrotome (Leica) to obtain 40 nm sample thickness. Samples were collected in formvar-coated single-slot grids (Science Services GmbH). Just before the imaging, samples were counterstained for 3-5 min with 2% uranyl acetate and for 30 s in 0.3% lead citrate in double-distilled H_2O. Images were obtained with a FEI Tecnai G20 transmission electron microscopy operating at 200 keV (Fig. 3D). Synapses were selected based on detectable postsynaptic density (PSD) (Fig. 3E). For each experiment, approximately 50 profiles per group were imaged with (2,048 × 2,048 pixels) CCD camera (Olympus) at 0.73 nm pixel size. The analysis was performed using ImageJ software and Matlab. Active zone (AZ) length was defined as the membrane opposite to the PSD (Fig. 3E). Synaptic vesicles were identified as visible circular membranous structures with a diameter of ~25-50 nm in a single plane of a 2D micrograph. To avoid bias, the analysis for each experiment was performed by one person who was blind to the experimental groups. The synaptic vesicles whose membrane was in direct contact with the AZ membrane were marked as docked SVs (Fig. 3E). The shortest distance of non-docked vesicles up to 20 nm from the AZ membrane were also analyzed (Fig. 3E).

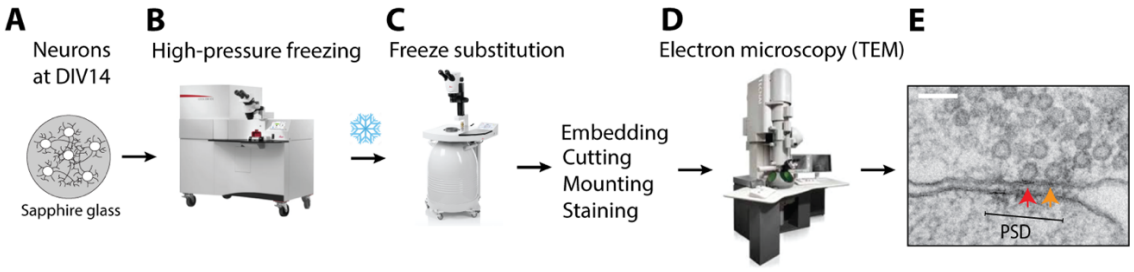

Figure 3. High-pressure freezing and TEM. **A**-**E**, Summary diagram illustrating high-pressure freezing fixation followed by freeze substitution, and transmission electron microscopy. In the representative EM image of the synapse (**E**), PSD is the postsynaptic density, red arrow indicates a docked vesicle, and orange arrow indicates a non-docked vesicle within 20 nm distance from the AZ membrane. Scale bar, 100 nm.

2.6 Immunocytochemistry and confocal microscopy

The autaptic neurons at DIV 14-20 were fixed in 4% paraformaldehyde (PFA) in PBS for 10 min (pH 7.4) at room temperature. Neurons were subsequently washed 3 times with PBS (each for 5 min). The permeabilization process was done with 0.1% PBS-Tween (PBST) solution for 10 min and blocking was performed with 5% normal goat serum in PBST for 1 h. Fixed neurons were incubated at 4°C overnight with the following primary antibodies: Rabbit anti-VGLUT1 (SYSY 135302; 1:2000), and Guinea-pig anti-Munc13-1 (SYSY 126104; 1:1000). VGLUT1 is a synaptic

vesicle marker that is used to detect the presynaptic area. After washing 3 times with PBST (each for 10 min), secondary antibodies conjugated with Alexa Fluor 488 and Alexa Fluor 647 (Jackson immunoresearch; 1:500), in donkey serum and 1 h at room temperature, were used to label VGLUT1 and Munc13-1 primary antibodies. Followed by washing three times with PBST (each for 10 min), the coverslips were mounted on glass slides with Mowiol (Sigma-Aldrich).

Single neurons in the astrocytic micro-islands were imaged using a Nikon scanning confocal microscopy (A1Rsi+) at optical magnification of ×60 with an oil immersion objective (numerical aperture (NA) = 1.4). Overexposure was eliminated by avoiding the fluorescence signal saturation in synapses. The *z*-series images at 0.3 µm depth were obtained at equal exposure times and 3-4 µm *z*-axis range. Images were taken at 1024 × 1024 pixel resolution and at the pixel size of 0.2 µm. Sum of intensity projections were used for the analysis. Analysis was performed blind using ImageJ software by marking synapses (VGLUT1 signals) as regions of interest (ROIs) for 50 synapses per neuron. For each ROI, the Munc13-1 fluorescence intensity was divided to the corresponding fluorescence intensity of VGLUT1. Approximately 20 neurons per group were analyzed in two independent cultures and the data were normalized to the control group.

2.7 Western-blot

Protein lysates for western-blot were obtained from mass cultured hippocampal neurons at DIV 14-20. To prepare the lysis buffer, 4% Complete Protease Inhibitor (Roche Diagnostics) was added to a buffer containing 50 mM Tris/HCl, pH 7.6, 150 mM NaCl, 1% Nonidet P-40, 0.5% sodium deoxycholate. Neurons were washed with Dulbecco's PBS (DPBS; Gibco) and 80 µl of lysis buffer per well was added. Neurons were scrubbed from the plates, and were incubated in ice for 30 min. Lysed cells were centrifuged for 15 min at 4°C. The supernatant was separated, and the protein concentration was quantified using BCA assay (ThermoFisher scientific).

A 3x Laemmli sample buffer was prepared with 150 mM Tris-HCl (pH 6.8), 6% SDS, 0.3% Bromophenol blue, 30% glycerol, and 300 mM DTT. The buffer was added to 30 µg of lysates and the samples were boiled at 95°C for 5 min. Next, the samples were mixed and centrifuged shortly. 30µl of the samples were loaded to SDS-polyacrylamide gel. After the electrophoresis, proteins were transferred onto a nitrocellulose membrane (Bio-Rad) for 3 h at 300 mA. Followed by blocking in 5% skim milk in PBST for 1 h, the proteins were labeled during overnight incubation with primary antibodies in the blocking solution. The primary antibodies included mouse anti-tubulin III (Sigma T8660, 1:2000) as a loading control, and either mouse anti-pan Munc13 (BD 610998, 1:500) or rabbit anti-RIM1/2 (SYSY 140203, 1:1000). Membranes were washed 3 times with PBST (each for 10 min), and Goat IgG Horseradish Peroxidase-

conjugated antibody (Jackson ImmunoResearch, 1:10000) was used for the labeling of primary antibodies. Finally, the proteins were detected by ECL (GE Healthcare Biosciences).

2.8 Statistical analysis

All data were analyzed with GraphPad Prism 7 and were represented as mean ± SEM. Sample sizes were not predetermined but were matched to those in similar studies (Camacho et al., 2017; Brockmann et al., 2020). The normality of data distribution was assessed with D'Agostino-Pearson test. In case of nonparametric distribution, group analysis was performed with Kruskal-Wallis test followed by Dunn's *post hoc* test and two data sets were compared with Mann-Whitney *U* test. In case of normal distribution, group analysis was performed with one-way ANOVA followed by Tukey's *post hoc* test and two data sets were compared with Student's t-test. The α level was set at 0.05. In the results section, data are shown as absolute values (mean ± SEM) unless otherwise specified. Also n refers to the total number of data points, and KW refers to Kruskal-Wallis test.

3. Results

In this section, I present a selection of important findings of my PhD project. Data from Fig. 5-8 can be found in Zarebidaki et al. (2020) (attached manuscript). Data from Fig. 4 have not been published yet.

3.1 Munc13 isoforms differentially contribute to the synapse function

The interaction of RIM and Munc13 is essential for the formation of the readily releasable pool of synaptic vesicles and fusion (Betz et al., 2001). However, not all Munc13 isoforms contain a RIM-interaction site (Fig. 4A; C2A domain). Thus, we investigated the extent to which RIM-interacting Munc13 isoforms (Munc13-1 and ubMunc13-2) and a Munc13 isoform that do not contain a RIM-binding site (bMunc13-2) contribute to synapse functions in hippocampal neurons. For this purpose, we took advantage of Munc13-1/2 double knockout (DKO) mouse hippocampal neurons and expressed the main cerebral Munc13 isoforms (Munc13-1, ubMunc13-2, and bMunc13-2) using lentiviral transduction (Fig. 4A). Since western blot revealed a successful expression of the Munc13 isoforms in DKO neurons (Fig. 4B), we proceeded to voltage-clamp recordings in autaptic cultures (Fig. 4C-F). Application of hypertonic sucrose on neurons induces a transient current, which corresponds to the readily releasable pool (RRP) of vesicles (Rosenmund and Stevens, 1996) (Fig. 4C). In addition, we analyzed the excitatory postsynaptic current (EPSC) which was elicited by 2 ms depolarization (Fig. 4D). As previously reported (Varoqueaux et al., 2002b; Varoqueaux et al., 2005), we confirmed that Munc13-1/2 DKO totally arrests vesicle priming and Ca^{2+}-dependent release (Fig. 4C-D). Thus, DKO data shown in Figure 4C and D basically correspond to the baseline noise.

Lentiviral Munc13-1 expression in DKO neurons rescued both RRP charge and EPSC amplitude more efficiently than ubMunc13-2 or bMunc13-2 (Fig 4C; Munc13-1: 0.36 ± 0.06 nC, n = 35; ubMunc13-2: 0.14 ± 0.03 nC, n = 39, $p = 0.0008$; bMunc13-2: 0.08 ± 0.02 nC, n =38, $p < 0.0001$, KW test; Fig. 4D; Munc13-1: 2.5 ± 0.36 nA, n = 46; ubMunc13-2: 1.13 ± 0.2 nA, n = 51, $p = 0.05$; bMunc13-2: 0.12 ± 0.03 nA, n = 46, $p < 0.0001$, KW test). This confirms that Munc13-1 is the main isoform that constitutes the core of priming process (Augustin et al., 1999a). Surprisingly, although bMunc13-2 and ubMunc13-2 structurally differ in RIM-binding capability (Fig. 4A; C2A domain), the RRP charge was not different between the two groups ($p = 0.26$, KW test). Nevertheless, ubMunc13-2 partially restored the AP-evoked release compared to bMunc13-2 ($p < 0.0001$, KW test). We next calculated the vesicular release probability (P_{vr}) by quantifying the ratio of EPSC charge to the sucrose-evoked charge. As a result of differential control of priming and AP-evoked release, P_{vr} was substantially diminished in bMunc13-2-expressing neurons compared with the other two isoforms (bMunc13-2: 1.42 ± 0.32 %, n = 38, ubMunc13-2: 8.44 ± 1.46 %, n = 39, $p < 0.0001$; Munc13-1: 5.78 ± 0.93 %, n = 35, $p < 0.0001$). This suggests that bMunc13-2 only primes low release efficient synaptic vesicles.

Studies have shown that in the absence of Munc13-1 in glutamatergic neurons, the RRP charge transiently increases by 2-3 fold shortly after high frequency stimulation (HFS) (Rosenmund et al., 2002). This phenotype of Munc13-1 knockout (KO) neurons has been correlated to an activity-dependent increase in residual Ca^{2+}, triggering Munc13-2-dependent transient augmentation of vesicle priming (Rosenmund et al., 2002; Lipstein et al., 2012). To examine how Munc13s differentially contribute to the activity-dependent RRP dynamics, we assessed the RRP size by applying hypertonic sucrose application before, and 2 s after HFS trains (50 trains at 10 Hz) and quantified the ratio of the second RRP size to the first (Fig. 4F). As expected, Munc13-1 rescue showed an RRP ratio of 0.99 ± 0.06 (n = 25). However, both bMunc13-2 and ubMunc13-2 revealed post-HFS RRP augmentation (ubMunc13-2: 1.65 ± 0.16, n = 29; bMunc13-2: 2.15 ± 0.18, n = 27) when compared to the Munc13-1 rescue ($p < 0.001$, KW test). This agrees with the notion that Munc13-2, in contrast to Munc13-1, contributes to post-train RRP augmentation (Rosenmund et al., 2002). Taken together, our results demonstrated that the structural variability of Munc13 isoforms differentially affects their function in the synapse.

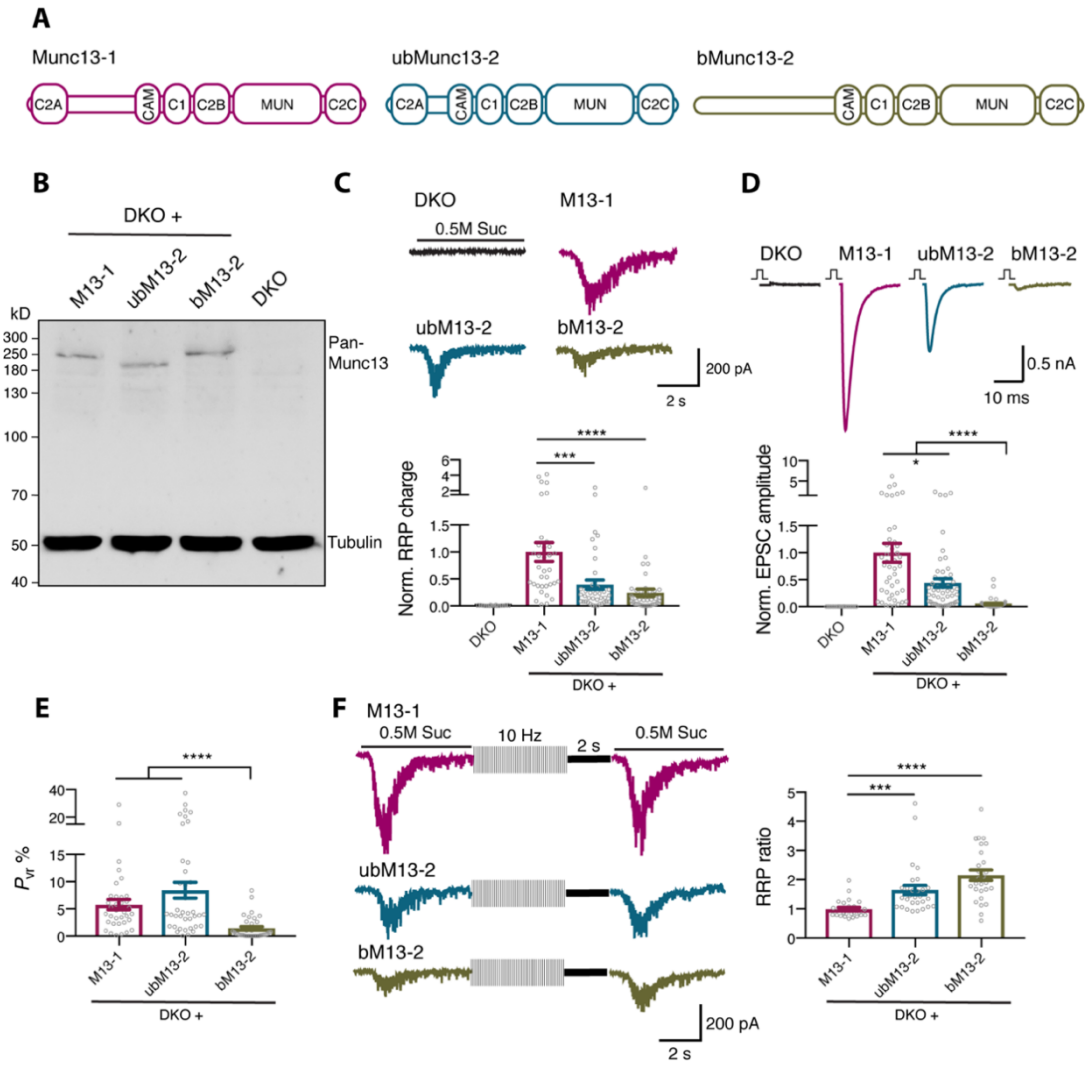

Figure 4. Differential rescue of Munc13 isoforms in Munc13-1/2 DKO hippocampal autaptic neurons. **A**, Scheme illustrating the domain structure of Munc13 isoforms. Munc13-1 and ubMunc13-2 share similar domain structures. bMunc13-2 does not contain the RIM1/2 binding motif (C2A) but has higher molecular weight than the other two isoforms. **B**, Western blot showing the expression of Munc13 isoforms in Munc13-1/2 DKO neurons. Left, molecular weight markers. **C**-**D** (top), Sample traces representing the readily releasable pool (RRP) of synaptic vesicles (**C**) and excitatory postsynaptic currents (EPSC) (**D**). **C**-**D** (bottom), Scatter bar plots showing the RRP charge (**C**) and EPSC amplitude (**D**) normalized to Munc13-1 group. **E**, Scatter bar graph demonstrating the vesicular release probability (P_{vr}) in %. **F** (left), Sample traces representing the RRP augmentation protocol. **F** (right), Scatter bar plot showing the RRP charge 2 s after HFS divided by the initial RRP charge. Data are from 3 independent cultures and indicate mean ± SEM; Kruskal Wallis test followed by Dunn's *post hoc* test. $p \leq 0.05$ (*), $p \leq 0.001$ (***), and $p \leq 0.0001$ (****). Data from this figure were not published before.

3.2 Deficiency in RIM1 and 2 impairs synaptic vesicle localization, neurotransmission, and Munc13-1 expression in the synapse

We showed that Munc13-1 is the main isoform that primes synaptic vesicles and is essential for efficient synaptic vesicle fusion. Since RIM also activates and stabilizes Munc13-1 in the presynaptic terminal (Andrews-Zwilling et al., 2006; Deng et al., 2011), we speculated a loss of

Munc13-1 in RIM-deficient neurons. Hence, we tested the effect of RIM on Munc13-1 localization in the synapses. We transduced mouse hippocampal RIM1/2^{flox} neurons at DIV1-2 with either inactive-Cre recombinase (ΔCre) or with Cre recombinase (Cre) to create RIM1/2 control and conditional double knockout (cDKO) neurons, respectively (Fig. 5A). We examined the efficiency of the knockout in hippocampal mass cultures by western blot (Fig. 5B refers to Fig. 1A in Zarebidaki et al. (2020)). As expected, expressing Cre recombinase eliminated RIM1/2 successfully from the hippocampus (Fig. 5B). We assessed the effect of RIM1/2 cDKO on the expression of Munc13-1 in the autaptic neurons by staining for VGLUT1, a synaptic vesicle marker, and Munc13-1 (Fig. 5C refers to Fig. 3A in Zarebidaki et al. (2020)). The normalized ratio of Munc13-1 fluorescence intensity to the corresponding VGLUT1 fluorescence intensity revealed a prominent loss of presynaptic Munc13-1 localization in RIM1/2 cDKO hippocampal neurons (Fig. 5D refers to Fig. 3B in Zarebidaki et al. (2020)), confirming the role of RIM in Munc13-1 recruitment to the presynaptic terminal.

Given that loss of RIM is accompanied by loss of Munc13-1, we expected an altered synapse ultrastructure and function in RIM1/2 cDKO neurons because Munc13-1/2-deficient neurons lack dock and primed synaptic vesicles (Varoqueaux et al., 2002a; Siksou et al., 2009). Electron microscopy studies on aldehyde-fixed RIM1/2 cDKO synapses have suggested a role for RIM in synaptic vesicle docking at the AZ membrane (Kaeser et al., 2011; Acuna et al., 2016). However, these results were inconclusive because a similar technique did not show any ultrastructural effect in Munc13-1 KO neurons (Augustin et al., 1999a). We eliminated the restrictions of aldehyde fixation by cryopreserving RIM control and cDKO synapses with high-pressure freezing technique. Using transmission electron microscopy (TEM), we imaged synapses with clear postsynaptic density (PSD) and we defined the membrane opposite to the PSD as the active zone (AZ) membrane (Fig. 5E; Fig. 5F refers to Extended data Fig. 1-2 in Zarebidaki et al. (2020)). Moreover, the vesicles whose outer leaflet was in contact with the inner leaflet of AZ membrane were defined as docked synaptic vesicles (Fig. 5E-F). In line with previous reports (Han et al., 2011; Kaeser et al., 2011), loss of RIM1/2 resulted in 0.28 ± 0.03 (n = 161) number of docked vesicles per 100 nm of AZ length, which was significantly less than the controls (ΔCre: 0.47 ± 0.04, n = 153, p = 0.0006, Mann-Whitney test) (Fig. 5G refers to the number of docked vesicles in Fig. 1H in Zarebidaki et al. (2020) in 100 nm of AZ length). In addition, we analysed the shortest distance of non-docked SVs from the AZ membrane, and observed a reduction of non-docked vesicles only up to 20 nm from the AZ membrane (ΔCre: 1.80 ± 0.12, n = 153; Cre: 1.28 ± 0.10, n = 161, p = 0.0004, Mann Whitney test) (Fig 5H refers to Fig. 1J in Zarebidaki et al.

(2020)). But we did not see differences in number of vesicles further away from the AZ membrane (Zarebidaki et al., 2020). This may implicate the action of RIM on localization of SV only within membrane-proximal regions (Fernandez-Busnadiego et al., 2013).

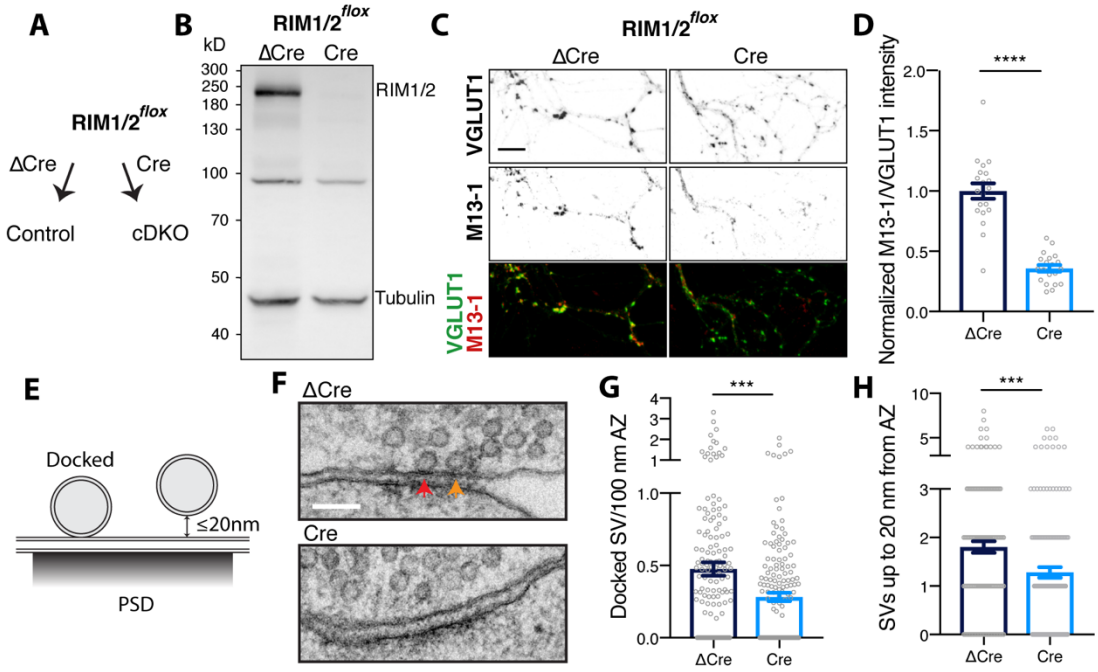

Figure 5. RIM is required for synaptic vesicle docking in mouse hippocampal neurons. **A**, Scheme illustrates the production of RIM1/2 control and cDKO neurons by infecting RIM1/2^{flox} neurons with inactivated Cre recombinase or Cre recombinase, respectively. **B**, Blot showing the protein expression of RIM1/2 in control and cDKO lysates. Left; molecular weight markers. **C**, Exemplary confocal microscopy images representing the fluorescence projection of VGLUT1 and Munc13-1. Scale bar, 10 µm. **D**, Scatter bar plot showing the normalized presynaptic fluorescence intensity of Munc13-1 in RIM1/2 control and cDKO neurons relative to VGLUT1 fluorescence intensity (2 independent cultures). **E**, Scheme illustrates a docked vesicle and a non-docked vesicle up to 20 nm from the AZ membrane. **F**, Example transmission electron micrographs of RIM1/2 control and cDKO synapses; docked vesicles (red arrow), vesicles ≤ 20 nm of the AZ membrane (orange arrow). Scale bar, 100 nm. **G-H**, Scatter bar plots showing the number of docked vesicles per 100 nm length of the AZ membrane (**G**) and non-docked vesicles up to 20 nm distance of the AZ membrane (**H**) from 3 independent cultures. Data indicate mean ± SEM. Statistics are performed by Mann-Whitney test except in **D** (Student's t test). $p \leq 0.001$ (***), $p \leq 0.0001$ (****). Reference to Zarebidaki et al. (2020): **B** refers to Fig. 1A; **C** and **D** refer to Fig. 3A, B; **F** is from Extended Data Fig. 1-2; **G** refers to the number of docked vesicles in Fig. 1H in 100 nm of AZ length; **H** refers to Fig. 1J; Order and layout of graphs are different from the paper.

In order to examine whether the loss of docked vesicles in RIM1/2 cDKO synapses is accompanied by impaired vesicle priming and release, we performed electrophysiological recordings on RIM1/2 control and cDKO in autaptic neurons. We detected an impaired RRP charge upon deletion of RIM1/2 (ΔCre: 0.7 ± 0.1 nC, n = 41; Cre: 0.08 ± 0.01 nC, n = 51, $p <$ 0.0001, Mann-Whitney test) (Fig. 6A refers to Fig. 3C, D in Zarebidaki et al. (2020)). This effect

was more drastic than vesicle docking impairment. Moreover, the Ca^{2+}-dependent exocytosis was almost completely abolished in RIM1/2 cDKO neurons (ΔCre: 6.3 ± 0.72 nA, n = 59; Cre: 0.18 ± 0.05 nA, n = 56, $p < 0.0001$, Mann-Whitney test) (Fig. 6B refers to Fig. 3E, F in Zarebidaki et al. (2020)). Due to the more severe loss of EPSC charge than RRP charge, the P_{vr} in RIM1/2 cDKO neurons was dramatically impaired (ΔCre: 6.4 ± 0.56 %, n = 41; Cre: 1.11 ± 0.3 %, n = 50, $p <$ 0.0001, Mann-Whitney test) (Fig. 6C refers to absolute P_{vr} values in Fig. 3G in Zarebidaki et al. (2020)). These data confirm the role of RIM1/2 in Ca^{2+} channel recruitment and function (Kaeser et al., 2011). The ultrastructural and electrophysiological characterization of RIM1/2 cDKO underscores a critical role of RIM both in synapse ultrastructure and function.

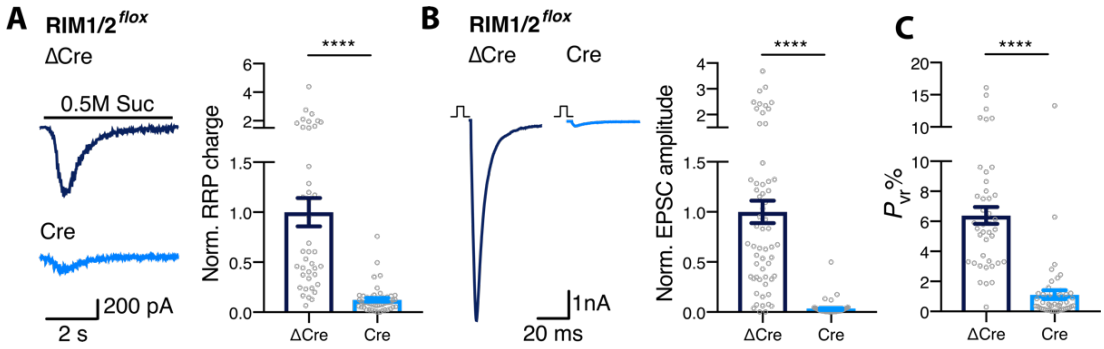

Figure 6. RIM is required for the priming process and Ca^{2+}-dependent release. **A**-**B**, Sample traces of RRP (**A**; left) and EPSC (**B**; left) and the scatter bar plots depicting the normalized RRP size (**A**; right) and the normalized EPSC amplitude (**B**; right). **C**, Scatter bar plot showing the P_{vr} (%). Data are from 5 independent cultures and indicate mean ± SEM; Mann-Whitney test. $p \leq 0.0001$ (****). Reference to Zarebidaki et al. (2020): **A** and **B** are from Fig. 3 C-F; **C** refers to absolute P_{vr} values in Fig. 3G; Order and layout of graphs are different from the paper.

3.3 The role of RIM and Munc13-1 in synapse functions

Due to the effect of RIM1/2 on Munc13-1 localization and function, our knowledge about Munc13-1-independent functions of RIM in synapses is restricted. To overcome this barrier, we produced neurons deficient for either RIM1/2, Munc13-1, or both, using a Cre-mediated RIM knockout as well as Munc13-1 knockdown (KD) (Fig. 7A). We have shown that KD of Munc13-1 in both control and RIM1/2 cDKO neurons successfully diminishes 95% of Munc13-1 (Zarebidaki et al., 2020). Next, we assessed the cooperation of these two proteins in synaptic vesicle localization. To achieve this goal, once more, we used high-pressure freezing followed by ultrastructural analysis. We reproduced our previous observation (Fig. 5G) by showing that removal of RIM impairs vesicle docking (ΔCre + Scr.: 0.65 ± 0.03, n =157; Cre + Scr.: 0.48 ± 0.03, n = 168, $p = 0.0008$, KW test) (Fig. 7B; Fig. 7C refers to the number of docked vesicles in Fig. 2F in Zarebidaki et al. (2020) in 100 nm length of AZ). We also observed a reduced number of non-docked SVs in RIM1/2 cDKO synapses up to 20 nm from the AZ membrane (ΔCre + Scr.:

2.53 ± 0.13, n =157; Cre + Scr.: 1.95 ± 0.13, n = 168, $p = 0.002$, KW test) (Fig. 7D refers to Fig. 2G in Zarebidaki et al. (2020)).

Similar to RIM1/2 cDKO neurons, Munc13-1 KD synapses showed an impaired vesicle docking (0.48 ± 0.03, n = 148) compared to the control ($p = 0.0007$, KW test) (Fig. 7C). Interestingly, elimination of Munc13-1 from RIM1/2 cDKO neurons revealed only 0.34 ± 0.03 (n = 167) docked vesicles per 100 nm of AZ, which was less than individual RIM1/2 or Munc13-1 deletions ($p < 0.01$, KW test) (Fig. 7C). This indicates that a simultaneous presence of both RIM1/2 and Munc13-1 in the synapse is required for vesicle docking. On the other hand, while deletion of RIM1/2 reduced the number of vesicles within 20 nm distance from the AZ membrane, Munc13-1 KD alone did not affect the vesicle number within this area (ΔCre + Munc13-1 shRNA: 2.95 ± 0.18, n = 148, $p > 0.999$, KW test) (Fig. 7D). Moreover, Munc13-1 KD in RIM1/2 cDKO synapses resulted in 1.98 ± 0.14 (n = 167) vesicles up to 20 nm from AZ membrane, similar to RIM1/2 cDKO neurons in presence of Munc13-1 ($p > 0.999$, KW test) (Fig. 7D). These data demonstrate that RIM does not require Munc13-1 for near-membrane localization of synaptic vesicles.

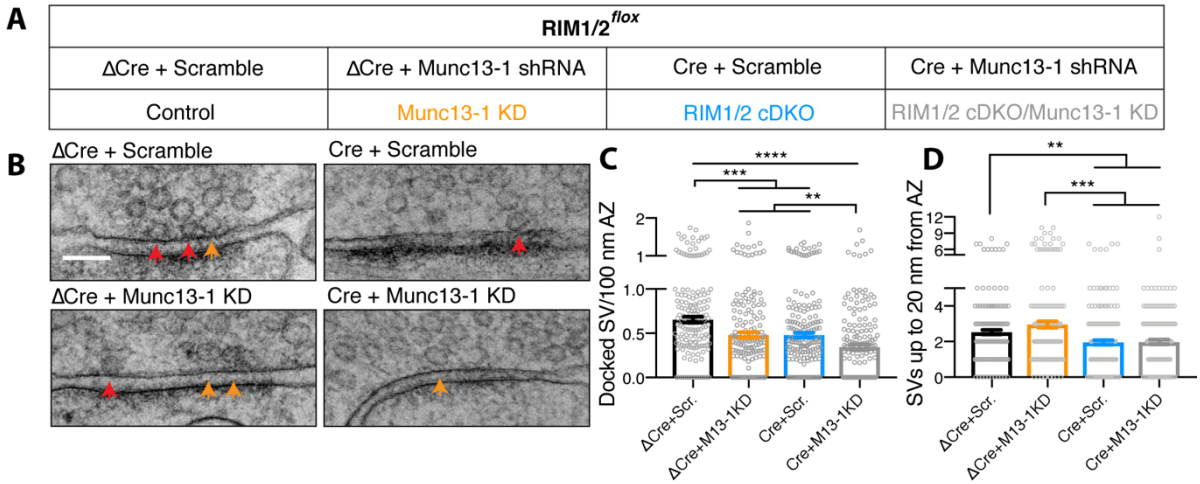

Figure 7. The role of RIM and Munc13-1 in synapse ultrastructure. **A**, Scheme illustrating the system where either or both of RIM and Munc13-1 were abolished from the synapses. **B**, Example electron micrographs of the groups as in **A**; docked vesicles (red arrows), vesicles up to 20 nm of AZ membrane (orange arrows). Scale bar, 100 nm. **C**-**D**, Scatter bar plots representing the normalized docked vesicles per 100 nm length of AZ (**C**), and number of non-docked vesicles up to 20 nm distance from AZ membrane (**D**). Data were analyzed from 3 independent cultures and indicate mean ± SEM; Kruskal Wallis test followed by Dunn's *post hoc* test. $p \leq 0.01$ (**), $p \leq 0.001$ (***), and $p \leq 0.0001$ (****). Reference to Zarebidaki et al. (2020): **B** refers to Fig. 2C; **C** refers to the number of docked vesicles in Fig. 2F in 100 nm of AZ length; **D** refers to Fig. 2G; Order and layout of graphs are different from the paper.

To separate the relative roles of RIM1/2 and Munc13-1 in synaptic vesicle priming and release, we conducted recordings of the autaptic hippocampal cultures from RIM1/2 and/or Munc13-1-deficient neurons (Fig. 8). Consistent with the vesicle docking phenotype, individual deletions of RIM1/2 or Munc13-1 impaired vesicle priming compared to the control (ΔCre + Scr.:

0.42 ± 0.04 nC, n = 60, Cre + Scr.: 0.12 ± 0.03 nC, n = 61, $p < 0.0001$; ΔCre + Munc13-1 shRNA: 0.08 ± 0.009 nC, n = 50, $p < 0.0001$, KW test) (Fig. 8A refers to Fig. 6A, B in Zarebidaki et al. (2020)). But in neurons that lacked both RIM1/2 and Munc13-1, RRP charge was at 0.05 ± 0.008 nC (n = 54), which was significantly less than Munc13-1 KD neurons in the presence of RIM ($p = 0.015$, KW test) (Fig. 8A). Thus, both RIM and Munc13-1 are required for vesicle priming. Also, our results from vesicle docking and priming (Fig. 7C; Fig. 8A), showed that vesicle priming is more sensitive to RIM and Munc13-1 expression.

We next examined how the Ca^{2+}-evoked release is modified by loss of RIM1/2 and/or Munc13-1 (Fig. 8B). We found that deletion of RIM1/2 drastically reduces the Ca^{2+}-evoked release (0.23 ± 0.06 nA, n = 72) compared with either the control (4.06 ± 0.48 nA, n = 72, $p < 0.0001$, KW test) or the Munc13-1 KD (0.75 ± 0.12 nA, n = 60, $p < 0.0001$, KW test) (Fig. 8B refers to Fig. 6C, D in Zarebidaki et al. (2020)). The more severely impaired EPSC in RIM1/2 cDKO than Munc13-1 KD indicates that loss of Ca^{2+}-dependent release in RIM1/2 cDKO neurons is not just caused by reduced RRP size. Due to the drastic loss of EPSC in RIM1/2 cDKO neurons, KD of Munc13-1 in these neurons did not further worsen the EPSC amplitude (Cre + Munc13-1 shRNA: 0.13 ± 0.04 nA, n = 63, $p = 0.74$, KW test) (Fig. 8B). Also, by analyzing the P_{vr}, we showed that Munc13-1 KD alone does not significantly affect the P_{vr} compared with the control, whereas RIM affects the P_{vr} regardless of Munc13-1 presence in the neurons (ΔCre + Scr.: 6.19 ± 0.65 %, n = 60; ΔCre + Munc13-1 shRNA: 4.16 ± 0.44 %, n = 50, $p = 0.45$; Cre + Scr.: 0.8 ± 0.11 %, n = 58, $p < 0.0001$; Cre + Munc13-1 shRNA: 0.95 ± 0.29, n = 47, $p < 0.0001$, KW test) (Fig. 8C refers to absolute P_{vr} in Fig. 6G in Zarebidaki et al. (2020)). These data underline the Munc13-1-independent role of RIM in modulating Ca^{2+}-dependent release efficacy.

Previously, we showed that ubMunc13-2 and bMunc13-2 contribute to activity-dependent RRP augmentation (Fig. 4F). It is not known whether RIM helps Munc13-2 to regulate this process. Therefore, we probed the RRP augmentation protocol (Fig. 8D corresponds to Fig. 7A, B in Zarebidaki et al. (2020)). The RRP ratio in controls was 0.89 ± 0.03 (n = 31). By comparing all of the groups with the control, we observed that the RRP size in Munc13-1 KD neurons was augmented by ~1.5 fold after HFS (1.33 ± 0.08, n = 28, $p < 0.0001$, KW test). Surprisingly, the RRP ratio in RIM1/2 cDKO neurons was similar to the control (1.07 ± 0.08, n = 29, $p = 0.854$, KW test). However, additional KD of Munc13-1 in RIM1/2 cDKO neurons again augmented the RRP by ~1.5 fold after HFS (1.45 ± 0.11, n = 23, $p < 0.0001$, KW test). These data suggest that, indeed, activity-induced RRP augmentation requires a complete abolishment of Munc13-1 regardless of RIM's expression.

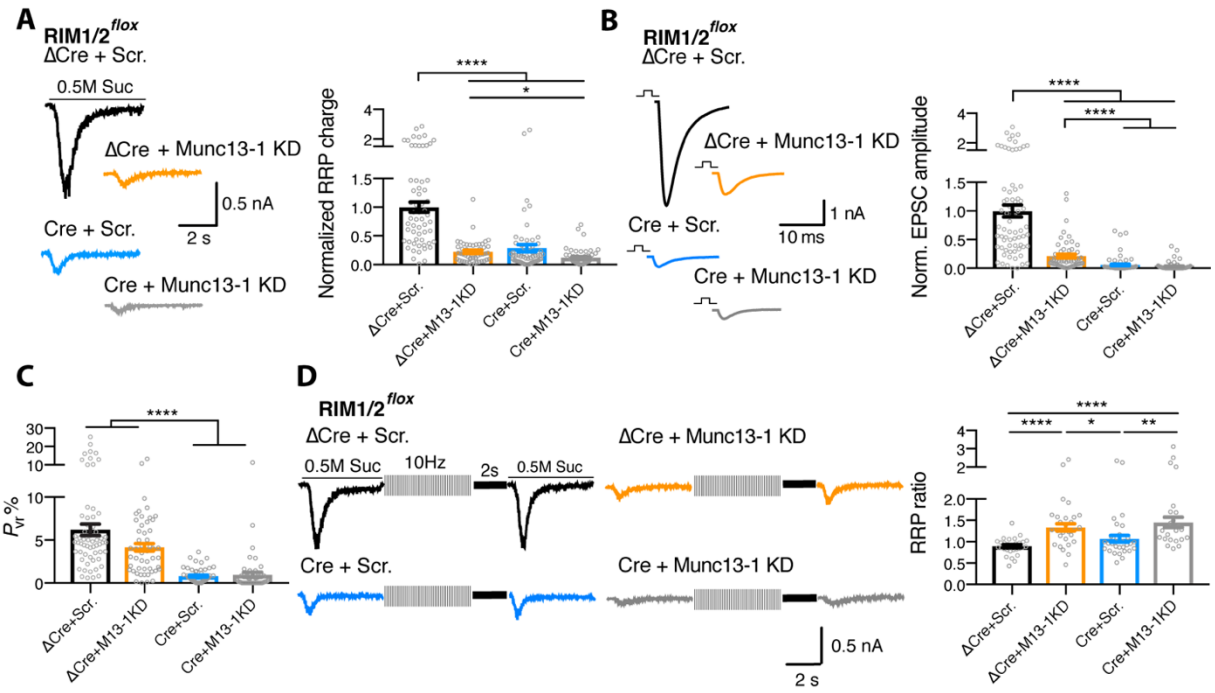

Figure 8. Relative contribution of RIM and Munc13-1 to synapse functions. **A-D**, Electrophysiological analysis of neurons where RIM and/or Munc13-1 were abolished from the synapse. **A-B**, Sample traces (left) of RRP (**A**) and EPSC (**B**) and the scatter bar plots (right) showing the normalized RRP charge (**A**) and EPSC amplitude (**B**). **C**, Scatter bar plot representing the P_{vr} (%). **A-C**, Data are from 5 independent cultures. **D** (left), Sample traces of RRP augmentation protocol. RRP charge was measured before, and 2 s after 50 APs at 10 Hz. **D** (right), Scatter bar plot demonstrating the RRP charge 2 s after HFS divided by the first RRP charge from 4 independent cultures. Data indicate mean ± SEM; Kruskal Wallis test followed by Dunn's *post hoc* test. $p \leq 0.05$ (*), $p \leq 0.01$ (**), and $p \leq 0.0001$ (****). Reference to Zarebidaki et al. (2020): **A** and **B** refer to Fig. 6A-D; **C** shows absolute P_{vr} in Fig. 6G; **D** refers to Fig. 7A, B; Order and layout of graphs are different from the paper.

4. Discussion

Since many brain diseases are associated with the dysfunction of synaptic proteins, it is important to understand how these proteins operate alone and with their interaction partners to accomplish their functions. However, the overlapping, redundant, or hierarchical interactions of proteins in the presynaptic terminal makes it difficult to define the direct impact of proteins on the synaptic vesicle cycle. As a solution, previous studies (Mukherjee et al., 2010; Acuna et al., 2016; Wang et al., 2016) along with our recent work (Brockmann et al., 2020) explored the independent and redundant function of AZ proteins by combining several protein deletions in one animal line and then consecutively re-expressing and investigating a single protein function. In this project, we used this valuable approach, as well as parallel comparison of different genetically modified systems, to dissect the role of RIM and Munc13 in vesicle docking, priming, and release in excitatory mouse hippocampal neurons. First, we assessed the role of Munc13 isoforms in respect to their putative interaction with RIM. We showed that Munc13 isoforms contribute to different

degrees of priming, vesicular release probability, and activity-dependent RRP dynamics. Also, we identified Munc13-1 as the key element for presynaptic AZ functions. Second, we examined the role of RIM and Munc13-1 individually and together in the ultrastructure and the physiology of the synapse. We found that (1) the presence of both RIM and Munc13-1 is required to dock and prime synaptic vesicles, (2) RIM/Munc13-1-dependent docking and priming are nonlinearly correlated, (3) RIM regulates the vesicular release probability and near-membrane synaptic vesicle localization independent of Munc13-1, and (4) Munc13-2-dependent post-train RRP augmentation does not require the presence of RIM. Our approach and findings provide a new perspective on how RIM and Munc13 operate to achieve efficient neurotransmission.

4.1 The role of RIM and Munc13-1 in the synapse ultrastructure

Advances in the characterization of how RIM1/2 and Munc13-1 impact on the synaptic ultrastructure have been made by EM analysis of aldehyde fixed neurons (Augustin et al., 1999a; Han et al., 2011; Kaeser et al., 2011; Acuna et al., 2016). Although this technique provides a broad knowledge on the synapse ultrastructure, it does not reliably detect the synaptic vesicle localization and docked vesicles (Korogod et al., 2015). However, high-pressure freezing fixation for EM circumvents the limitations of aldehyde fixation by immobilizing and cryopreserving the synapses and brings an opportunity to address the ultrastructural equivalents of synapse functions. Following this aim, Siksou et al. (2009) cryopreserved priming-incompetent Munc13-1/2 DKO neurons and found a total abolishment of membrane-docked vesicles in these neurons. This study suggested that vesicle docking and priming are directly correlated processes. In the current project, we provide a powerful system to re-examine the correlation of docking and priming procedures, as RIM1/2 and Munc13-1 interaction constitutes the core of priming process (Deng et al., 2011; Camacho et al., 2017). First, we confirm that in RIM1/2 cDKO synapses the membrane-docked vesicles are reduced (Gracheva et al., 2008; Han et al., 2011; Kaeser et al., 2011; Wang et al., 2016). Second, we demonstrate that vesicle docking is impaired in Munc13-1 KD hippocampal neurons, which was masked in the previous study using the aldehyde-fixed Munc13-1 KO neurons (Augustin et al., 1999a). Despite the ~30-40% docking deficit in RIM1/2 cDKO and Munc13-1 KD synapses, both show a severe loss of primed vesicles by ~80-90%. We reason that fewer numbers of RIM/Munc13-1 molecules are needed for vesicle docking compared to the downstream priming process. However, we do not exclude that the priming process may occur at subnanometer vesicle-AZ membrane distances, which cannot be resolved in our analysis. Therefore, we conclude that the docking and priming are related procedures, but the relative differences between the two functions depend on the stoichiometry of the contributing molecules.

We demonstrate that RIM localizes synaptic vesicles near to the AZ membrane, which implicates a possible role of RIM in vesicle tethering (Fernandez-Busnadiego et al., 2013). Importantly, we reveal that RIM does not require Munc13-1 for near-membrane vesicle localization. In the related publication of this study (Zarebidaki et al., 2020), we showed that the deletion of RIM1/2 or Munc13-1 do not affect the vesicle number at further distances from the AZ membrane or the AZ length. Hence, the specific impact of RIM1/2 cDKO on localization of membrane-proximal vesicles cannot be influenced by ultrastructural variables. Together, our results emphasize on a Munc13-1-independent role of RIM in localization of vesicles close to the AZ membrane, whereas the docking and priming functions of RIM and Munc13 are correlated.

4.2 Differential control of synapse functions by RIM and Munc13 isoforms

Munc13-2 KO neurons or Munc13-1 rescue in Munc13-1/2 DKO neurons exhibit high initial P_{vr} and synaptic depression (Rosenmund et al., 2002; Junge et al., 2004). Also, ubMunc13-2 rescue in Munc13-1/2 DKO neurons induces high initial P_{vr}, but in contrast to Munc13-1, displays synaptic facilitation and post-train RRP augmentation. We now show that bMunc13-2 barely primes vesicles and that primed vesicles cannot efficiently release their neurotransmitters. However, bMunc13-2 induces post-train RRP augmentation similar to ubMunc13-2. One possibility for the unique function of bMunc13-2 is the absence of RIM-binding domain. Because also a constitutive monomerized Munc13-1 mutant that lacks RIM-binding site, cannot fully prime vesicles in Munc13-1/2 DKO neurons (Camacho et al., 2017). Another possibility is the structural specificity of the CaM binding site in bMunc13-2 that partially inhibits both vesicle priming and P_{vr} at rest but enhances post-train RRP augmentation (Lipstein et al., 2012). In general, the CaM-binding, C2B, and C1 domains of Munc13 isoforms differentially regulate the activity-dependent RRP dynamics (Junge et al., 2004; Basu et al., 2007; Lipstein et al., 2012), a process which we demonstrate does not require the presence of RIM. Thus, it is notable that the structural variabilities of Munc13 isoforms and their putative interaction with RIM shape their functions in different directions.

We show that although both ubMunc13-2 and Munc13-1 share similar domain structures and both interact with RIM, the ubMunc13-2 primes half of the vesicles compared to Munc13-1. The differential effect of these two isoforms on vesicle priming is interesting and needs to be further investigated. Despite the different priming function of Munc13-1 and ubMunc13-2, both isoforms contribute to high P_{vr}, and the presence of RIM is required for an efficient vesicle fusion. However, we show that RIM does not need Munc13s to provide high probability of release, as RIM regulates P_{vr} via its direct interactions with Ca^{2+} channels and presynaptic membrane (Kaeser, 2011; de Jong et al., 2018). We have also reported that the Rab3 binding site of RIM, is essential

for the P_{vr} (Brockmann et al., 2020). Overall, despite the tightly related functions of RIM and isoforms of Munc13s, they regulate some synapse functions independent from each other.

5. Conclusions

The molecular processes that coordinate the steps of synaptic vesicle cycle ultimately influence neurotransmission. As a result, any impairment in these processes may cause synapse-associated diseases. This study identifies functions of RIM and Munc13 that differentially affect the fate of synaptic vesicles. Based on our current findings and previous studies, we conclude that RIM modulates two consecutive functions in the presynaptic terminal: First, RIM mediates membrane-proximal vesicle localization independent of Munc13-1 (Zarebidaki et al., 2020). Second, RIM regulates vesicle docking/priming via activation and recruitment of Munc13-1 (Andrews-Zwilling et al., 2006; Deng et al., 2011). In addition, RIM is essential to provide high-release efficient synaptic vesicles but its interaction with Munc13-1 is not necessary to maintain this function. Although the majority of neurons utilize RIM and Munc13-1 for priming and release processes, at least 10% of glutamatergic synapses use bMunc13-2 (Rosenmund et al., 2002; Kawabe et al., 2017). The bMunc13-2 isoform is responsible for low-release efficient synaptic vesicles and post-HFS RRP augmentation, but its role in synapse is only unmasked by almost complete deletion of RIM and Munc13-1. Therefore, we conclude that not only the intrinsic properties of Munc13 isoforms, but also their expression relative to each other defines the P_{vr} and activity-dependent RRP dynamics. Since the expression of synaptic proteins are cell- and synapse-type specific, our findings are important to understand the synaptic heterogeneity and neuronal behavior in different brain regions. We hope that our approach and results pave the way toward a more comprehensive understanding of how protein expression levels and isoforms contribute to synaptic diversity.

6. Outlook

Investigating the individual function of presynaptic proteins is essential to understand the physiology of neurons and the synaptopathies associated with protein malfunctions. Here, we focused on the roles of RIM and Munc13 in the synapse, as both proteins are key regulatory elements in the AZ. We found a Munc13-1-independent vesicle tethering by RIM. In the next step, we will investigate how RIM-mediated vesicle tethering affects the synaptic output. Moreover, in this study and in our recent work (Brockmann et al., 2020), we noted that glutamatergic neurons are more sensitive to the alterations of RIM's function, compared to the previous studies in GABAergic neurons (Deng et al., 2011; Kaeser et al., 2011). The possibility of cell-type specific effect of RIM on neurotransmission motivates us to take a further step and explore the molecular

mechanisms governing the vesicle priming and release probability in excitatory and inhibitory neurons. It is known that in GABAergic neurons, Munc13-1 and Munc13-2 redundantly prime vesicles (Augustin et al., 1999a). Given the small contribution of Munc13-2 to the glutamatergic neurotransmission, it is unclear how GABAergic synapses redundantly use Munc13-2 for the priming process. Therefore, first, we should do structure-functional experiments to investigate the molecular mechanisms that differentiate the priming functions of Munc13-2 and Munc13-1, and second, we should study the differential molecular priming mechanisms that regulate inhibitory and excitatory neurotransmission. We hope that our approach helps further research in the field to investigate the role of synaptic proteins in each step of neurotransmitter release.

7. Bibliography

Acuna C, Liu X, Sudhof TC (2016) How to Make an Active Zone: Unexpected Universal Functional Redundancy between RIMs and RIM-BPs. Neuron 91:792-807.

Andrews-Zwilling YS, Kawabe H, Reim K, Varoqueaux F, Brose N (2006) Binding to Rab3A-interacting molecule RIM regulates the presynaptic recruitment of Munc13-1 and ubMunc13-2. J Biol Chem 281:19720-19731.

Augustin I, Rosenmund C, Sudhof TC, Brose N (1999a) Munc13-1 is essential for fusion competence of glutamatergic synaptic vesicles. Nature 400:457-461.

Augustin I, Betz A, Herrmann C, Jo T, Brose N (1999b) Differential expression of two novel Munc13 proteins in rat brain. Biochem J 337 (Pt 3):363-371.

Basu J, Betz A, Brose N, Rosenmund C (2007) Munc13-1 C1 domain activation lowers the energy barrier for synaptic vesicle fusion. J Neurosci 27:1200-1210.

Bekkers JM, Stevens CF (1991) Excitatory and inhibitory autaptic currents in isolated hippocampal neurons maintained in cell culture. Proc Natl Acad Sci U S A 88:7834-7838.

Betz A, Thakur P, Junge HJ, Ashery U, Rhee JS, Scheuss V, Rosenmund C, Rettig J, Brose N (2001) Functional interaction of the active zone proteins Munc13-1 and RIM1 in synaptic vesicle priming. Neuron 30:183-196.

Bohme MA, Beis C, Reddy-Alla S, Reynolds E, Mampell MM, Grasskamp AT, Lutzkendorf J, Bergeron DD, Driller JH, Babikir H, Gottfert F, Robinson IM, O'Kane CJ, Hell SW, Wahl MC, Stelzl U, Loll B, Walter AM, Sigrist SJ (2016) Active zone scaffolds differentially accumulate Unc13 isoforms to tune Ca(2+) channel-vesicle coupling. Nat Neurosci 19:1311-1320.

Brockmann MM, Zarebidaki F, Camacho M, Grauel MK, Trimbuch T, Sudhof TC, Rosenmund C (2020) A Trio of Active Zone Proteins Comprised of RIM-BPs, RIMs, and Munc13s Governs Neurotransmitter Release. Cell Reports 32.

Camacho M, Basu J, Trimbuch T, Chang S, Pulido-Lozano C, Chang SS, Duluvova I, Abo-Rady M, Rizo J, Rosenmund C (2017) Heterodimerization of Munc13 C2A domain with RIM regulates synaptic vesicle docking and priming. Nat Commun 8:15293.

de Jong APH, Roggero CM, Ho MR, Wong MY, Brautigam CA, Rizo J, Kaeser PS (2018) RIM C2B Domains Target Presynaptic Active Zone Functions to PIP2-Containing Membranes. Neuron 98:335-349 e337.

Deng L, Kaeser PS, Xu W, Sudhof TC (2011) RIM proteins activate vesicle priming by reversing autoinhibitory homodimerization of Munc13. Neuron 69:317-331.

Dulubova I, Lou X, Lu J, Huryeva I, Alam A, Schneggenburger R, Sudhof TC, Rizo J (2005) A Munc13/RIM/Rab3 tripartite complex: from priming to plasticity? EMBO J 24:2839-2850.

Fernandez-Busnadiego R, Asano S, Oprisoreanu AM, Sakata E, Doengi M, Kochovski Z, Zurner M, Stein V, Schoch S, Baumeister W, Lucic V (2013) Cryo-electron tomography reveals a critical role of RIM1alpha in synaptic vesicle tethering. J Cell Biol 201:725-740.

Fukuda M (2003) Distinct Rab binding specificity of Rim1, Rim2, rabphilin, and Noc2. Identification of a critical determinant of Rab3A/Rab27A recognition by Rim2. J Biol Chem 278:15373-15380.

Gracheva EO, Hadwiger G, Nonet ML, Richmond JE (2008) Direct interactions between C. elegans RAB-3 and Rim provide a mechanism to target vesicles to the presynaptic density. Neurosci Lett 444:137-142.

Gundelfinger ED, Kessels MM, Qualmann B (2003) Temporal and spatial coordination of exocytosis and endocytosis. Nat Rev Mol Cell Biol 4:127-139.

Han Y, Kaeser PS, Sudhof TC, Schneggenburger R (2011) RIM determines Ca(2)+ channel density and vesicle docking at the presynaptic active zone. Neuron 69:304-316.
Heuser JE, Reese TS (1973) Evidence for Recycling of Synaptic Vesicle Membrane during Transmitter Release at Frog Neuromuscular Junction. Journal of Cell Biology 57:315-344.
Junge HJ, Rhee JS, Jahn O, Varoqueaux F, Spiess J, Waxham MN, Rosenmund C, Brose N (2004) Calmodulin and Munc13 form a Ca2+ sensor/effector complex that controls short-term synaptic plasticity. Cell 118:389-401.
Kaeser PS (2011) Pushing synaptic vesicles over the RIM. Cell Logist 1:106-110.
Kaeser PS, Deng L, Wang Y, Dulubova I, Liu X, Rizo J, Sudhof TC (2011) RIM proteins tether Ca2+ channels to presynaptic active zones via a direct PDZ-domain interaction. Cell 144:282-295.
Kawabe H, Mitkovski M, Kaeser PS, Hirrlinger J, Opazo F, Nestvogel D, Kalla S, Fejtova A, Verrier SE, Bungers SR, Cooper BH, Varoqueaux F, Wang Y, Nehring RB, Gundelfinger ED, Rosenmund C, Rizzoli SO, Sudhof TC, Rhee JS, Brose N (2017) ELKS1 localizes the synaptic vesicle priming protein bMunc 13-2 to a specific subset of active zones. Journal of Cell Biology 216:1143-1161.
Korogod N, Petersen CC, Knott GW (2015) Ultrastructural analysis of adult mouse neocortex comparing aldehyde perfusion with cryo fixation. Elife 4.
Landis DM, Hall AK, Weinstein LA, Reese TS (1988) The organization of cytoplasm at the presynaptic active zone of a central nervous system synapse. Neuron 1:201-209.
Lipstein N, Schaks S, Dimova K, Kalkhof S, Ihling C, Kolbel K, Ashery U, Rhee J, Brose N, Sinz A, Jahn O (2012) Nonconserved Ca(2+)/calmodulin binding sites in Munc13s differentially control synaptic short-term plasticity. Mol Cell Biol 32:4628-4641.
Mukherjee K, Yang X, Gerber SH, Kwon HB, Ho A, Castillo PE, Liu X, Sudhof TC (2010) Piccolo and bassoon maintain synaptic vesicle clustering without directly participating in vesicle exocytosis. Proc Natl Acad Sci U S A 107:6504-6509.
Rizo J, Chen X, Arac D (2006) Unraveling the mechanisms of synaptotagmin and SNARE function in neurotransmitter release. Trends Cell Biol 16:339-350.
Rosenmund C, Stevens CF (1996) Definition of the readily releasable pool of vesicles at hippocampal synapses. Neuron 16:1197-1207.
Rosenmund C, Sigler A, Augustin I, Reim K, Brose N, Rhee JS (2002) Differential control of vesicle priming and short-term plasticity by Munc13 isoforms. Neuron 33:411-424.
Sakamoto H, Ariyoshi T, Kimpara N, Sugao K, Taiko I, Takikawa K, Asanuma D, Namiki S, Hirose K (2018) Synaptic weight set by Munc13-1 supramolecular assemblies. Nat Neurosci 21:41-49.
Siksou L, Varoqueaux F, Pascual O, Triller A, Brose N, Marty S (2009) A common molecular basis for membrane docking and functional priming of synaptic vesicles. Eur J Neurosci 30:49-56.
Stevens DR, Wu ZX, Matti U, Junge HJ, Schirra C, Becherer U, Wojcik SM, Brose N, Rettig J (2005) Identification of the minimal protein domain required for priming activity of Munc13-1. Curr Biol 15:2243-2248.
Sudhof TC (2004) The synaptic vesicle cycle. Annu Rev Neurosci 27:509-547.
Sudhof TC (2012) The presynaptic active zone. Neuron 75:11-25.
Varoqueaux F, Sons MS, Plomp JJ, Brose N (2005) Aberrant morphology and residual transmitter release at the Munc13-deficient mouse neuromuscular synapse. Mol Cell Biol 25:5973-5984.
Varoqueaux F, Sigler A, Rhee JS, Brose N, Enk C, Reim K, Rosenmund C (2002a) Total arrest of spontaneous and evoked synaptic transmission but normal synaptogenesis in the absence of Munc13-mediated vesicle priming. Proc Natl Acad Sci U S A 99:9037-9042.
Varoqueaux F, Sigler A, Rhee JS, Brose N, Enk C, Reim K, Rosenmund C (2002b) Total arrest of spontaneous and evoked synaptic transmission but normal synaptogenesis in the absence of Munc13-mediated vesicle priming. P Natl Acad Sci USA 99:9037-9042.
Wang SSH, Held RG, Wong MY, Liu C, Karakhanyan A, Kaeser PS (2016) Fusion Competent Synaptic Vesicles Persist upon Active Zone Disruption and Loss of Vesicle Docking. Neuron 91:777-791.
Wang Y, Okamoto M, Schmitz F, Hofmann K, Sudhof TC (1997) Rim is a putative Rab3 effector in regulating synaptic-vesicle fusion. Nature 388:593-598.
Zarebidaki F, Camacho M, Brockmann MM, Trimbuch T, Herman MA, Rosenmund C (2020) Disentangling the Roles of RIM and Munc13 in Synaptic Vesicle Localization and Neurotransmission. The Journal of Neuroscience 40:9372-9385.

8. Statutory Declaration

I, Fereshteh Zarebidaki, by personally signing this document in lieu of an oath, hereby affirm that I prepared the submitted dissertation on the topic "The roles of RIM and Munc13 in the presynaptic terminal of murine hippocampal neurons", independently and without the support of third parties, and that I used no other sources and aids than those stated.

All parts which are based on the publications or presentations of other authors, either in letter or in spirit, are specified as such in accordance with the citing guidelines. The sections on methodology (in particular regarding practical work, laboratory regulations, statistical processing) and results (in particular regarding figures, charts and tables) are exclusively my responsibility.

Furthermore, I declare that I have correctly marked all of the data, the analyses, and the conclusions generated from data obtained in collaboration with other persons, and that I have correctly marked my own contribution and the contributions of other persons (cf. declaration of contribution). I have correctly marked all texts or parts of texts that were generated in collaboration with other persons.

My contributions to any publications to this dissertation correspond to those stated in the below joint declaration made together with the supervisor. All publications created within the scope of the dissertation comply with the guidelines of the ICMJE (International Committee of Medical Journal Editors; www.icmje.org) on authorship. In addition, I declare that I shall comply with the regulations of Charité – Universitätsmedizin Berlin on ensuring good scientific practice.

I declare that I have not yet submitted this dissertation in identical or similar form to another Faculty.

The significance of this statutory declaration and the consequences of a false statutory declaration under criminal law (Sections 156, 161 of the German Criminal Code) are known to me.

_____

Date and Signature

9. Detailed Declaration of Contribution

Fereshteh Zarebidaki contributed the following to the below listed publication:

Fereshteh Zarebidaki, Marcial Camacho, Marisa M. Brockmann, Thorsten Trimbuch, Melissa A. Herman, Christian Rosenmund. Disentangling the roles of RIM and Munc13 in synaptic vesicle localization and neurotransmission (2020). *Journal of Neuroscience*. 40 (49) 9372-9385; DOI: https://doi.org/10.1523/JNEUROSCI.1922-20.2020

Contribution in detail:

Design of research:

C. Rosenmund, F. Zarebidaki, M. Camacho, and M. M. Brockmann, conceived the idea and designed the experiments.

Execution of experiments and data analysis:

F. Zarebidaki performed all hippocampal culture preparation and R. Danneberg, M. Petzold, and H. Lerch prepared the astrocytic cultures. T. Trimbuch, B. Brokowski and K. Pötschke prepared the Lentivirus (Figure 1 to 7).

F. Zarebidaki performed all electrophysiological recordings (Figures 3, 5, 6, and 7).

F. Zarebidaki performed confocal microscopy and B. Söhl-Kielczynski helped with all immunostainings (Figures 3 and 4).

F. Zarebidaki performed high-pressure freezing, sample embedding, and transmission electron microscopy and B. Söhl-Kielczynski performed all sample cuttings (Figures 1, 2, 1-2, 2-2).

F. Zarebidaki performed the western blots and imaging of the blots (Figures 1, 2, 4).

F. Zarebidaki collected all data, performed all data analysis, data visualization, and the statistical tests for all experiments (Figure 1 to 7 and Extended data Figure 1-1 to 7-1).

F. Zarebidaki prepared all figures and tables (Figure 1 to 7 and Extended data Figure 1-1 to 7-1).

Manuscript preparation:

F. Zarebidaki together with C. Rosenmund and M. Camacho wrote the manuscript. C. Rosenmund, F. Zarebidaki, M. Camacho, M. M. Brockmann, and M. A. Herman edited the manuscript.

_____

Signature of doctoral candidate

10. Excerpt from the Journal Summary List (ISI Web of Knowledge)

InCites Journal Citation Reports — Clarivate Analytics

Journal Data Filtered By: Selected JCR Year: 2018 Selected Editions: SCIE Selected Categories: 'NEUROSCIENCES' Selected Category Scheme: WoS

Rank	Full Journal Title	Total Cites	Journal Impact Factor	Eigenfactor Score
1	NATURE REVIEWS NEUROSCIENCE	43,107	33.162	0.068470
2	NATURE NEUROSCIENCE	63,390	21.126	0.164630
3	ACTA NEUROPATHOLOGICA	20,206	18.174	0.041640
4	BEHAVIORAL AND BRAIN SCIENCES	9,377	17.194	0.010250
5	TRENDS IN COGNITIVE SCIENCES	27,095	16.173	0.040040
6	JOURNAL OF PINEAL RESEARCH	10,695	15.221	0.010560
7	NEURON	95,348	14.403	0.218590
8	TRENDS IN NEUROSCIENCES	20,163	12.314	0.024470
9	Annual Review of Neuroscience	14,042	12.043	0.015010
10	MOLECULAR PSYCHIATRY	20,353	11.973	0.049280
11	BRAIN	52,970	11.814	0.073990
12	BIOLOGICAL PSYCHIATRY	43,122	11.501	0.053290
13	PROGRESS IN NEUROBIOLOGY	12,929	10.658	0.013220
14	Nature Human Behaviour	1,230	10.575	0.006540
15	SLEEP MEDICINE REVIEWS	6,920	10.517	0.010910
16	ANNALS OF NEUROLOGY	37,336	9.496	0.048610
17	Molecular Neurodegeneration	4,248	8.274	0.011350
18	NEUROSCIENCE AND BIOBEHAVIORAL REVIEWS	26,724	8.002	0.051570
19	FRONTIERS IN NEUROENDOCRINOLOGY	4,196	7.852	0.005490
20	Neurology-Neuroimmunology & Neuroinflammation	1,996	7.353	0.008220
21	NEUROPSYCHOPHARMACOLOGY	25,672	7.160	0.039080
22	Brain Stimulation	5,457	6.919	0.014460
23	NEUROPATHOLOGY AND APPLIED NEUROBIOLOGY	3,876	6.878	0.006420
24	NEUROENDOCRINOLOGY	5,046	6.804	0.005700
25	NEUROSCIENTIST	4,986	6.791	0.008510
26	BRAIN PATHOLOGY	5,263	6.352	0.007880
27	BRAIN BEHAVIOR AND IMMUNITY	14,533	6.170	0.025680
28	Alzheimers Research & Therapy	3,160	6.142	0.010700
29	JOURNAL OF NEUROSCIENCE	175,046	6.074	0.233380
30	JOURNAL OF CEREBRAL BLOOD FLOW AND METABOLISM	19,766	6.040	0.028040

11. Printed copy of selected publication

Fereshteh Zarebidaki, Marcial Camacho, Marisa M. Brockmann, Thorsten Trimbuch, Melissa A. Herman, Christian Rosenmund. Disentangling the roles of RIM and Munc13 in synaptic vesicle localization and neurotransmission (2020). *Journal of Neuroscience*. 40 (49) 9372-9385; DOI: https://doi.org/10.1523/JNEUROSCI.1922-20.2020

Cellular/Molecular

Disentangling the Roles of RIM and Munc13 in Synaptic Vesicle Localization and Neurotransmission

Fereshteh Zarebidaki, Marcial Camacho, Marisa M. Brockmann, Thorsten Trimbuch, Melissa A. Herman, and Christian Rosenmund
Institute of Neurophysiology and NeuroCure Cluster of Excellence, Charité-Universitätsmedizin, Berlin, 10117, Germany

Efficient neurotransmitter release at the presynaptic terminal requires docking of synaptic vesicles to the active zone membrane and formation of fusion-competent synaptic vesicles near voltage-gated Ca^{2+} channels. Rab3-interacting molecule (RIM) is a critical active zone organizer, as it recruits Ca^{2+} channels and activates synaptic vesicle docking and priming via Munc13-1. However, our knowledge about Munc13-independent contributions of RIM to active zone functions is limited. To identify the functions that are solely mediated by RIM, we used genetic manipulations to control RIM and Munc13-1 activity in cultured hippocampal neurons from mice of either sex and compared synaptic ultrastructure and neurotransmission. We found that RIM modulates synaptic vesicle localization in the proximity of the active zone membrane independent of Munc13-1. In another step, both RIM and Munc13 mediate synaptic vesicle docking and priming. In addition, while the activity of both RIM and Munc13-1 is required for Ca^{2+}-evoked release, RIM uniquely controls neurotransmitter release efficiency. However, activity-dependent augmentation of synaptic vesicle pool size relies exclusively on the action of Munc13s. Based on our results, we extend previous findings and propose a refined model in which RIM and Munc13-1 act in overlapping and independent stages of synaptic vesicle localization and release.

Key words: active zone; electron microscopy; Munc13; RIM; synaptic transmission; synaptic vesicle

Significance Statement

The presynaptic active zone is composed of scaffolding proteins that functionally interact to localize synaptic vesicles to release sites, ensuring neurotransmission. Our current knowledge of the presynaptic active zone function relies on structure-function analysis, which has provided detailed information on the network of interactions and the impact of active zone proteins. Yet, the hierarchical, redundant, or independent cooperation of each active zone protein to synapse functions is not fully understood. Rab3-interacting molecule and Munc13 are the two key functionally interacting active zone proteins. Here, we dissected the distinct actions of Rab3-interacting molecule and Munc13-1 from both ultrastructural and physiological aspects. Our findings provide a more detailed view of how these two presynaptic proteins orchestrate their functions to achieve synaptic transmission.

Introduction

At presynaptic terminals, neurotransmitter release occurs at specific regions known as active zones (AZ). AZs are morphologically characterized by a complex network of proteins (Gundelfinger et al., 2003). The proteins that constitute the cytomatrix of the AZ (CAZ) play a central role in neurotransmitter release by localizing and clustering Ca^{2+} channels, and by regulating the stages of the synaptic vesicle (SV) cycle, such as tethering, docking, priming, and fusion (Sudhof, 2012). Among these functions, dissecting the role of specific molecular components in different steps of the SV cycle has presented technical challenges: (1) vesicle tethering and docking can only be distinguished from the downstream physiological events of vesicle priming and release by ultrastructure (Verhage and Sorensen, 2008); and (2) the individual protein components of the CAZ may contribute to more than one stage of neurotransmitter release (Ackermann et al., 2015).

Received July 23, 2020; revised Sep. 22, 2020; accepted Oct. 15, 2020.

Author contributions: C.R., F.Z., M.C., and M.M.B. designed research; C.R., F.Z., M.C., M.M.B., and M.A.H. edited the paper; F.Z. performed research; F.Z. analyzed data; F.Z. and M.C. wrote the first draft of the paper; F.Z. and M.C. wrote the paper; T.T. contributed unpublished reagents/analytic tools.

This work was supported by German Research Council Grant CRC 958 and Reinhart Koselleck project. We thank Berit Söhl-Kielczynski, Bettina Brokowski, Katja Pötschke, Sabine Lenz, Heike Lerch, Miriam Petzold, and Rike Dannenberg for excellent technical support; Charité Viral core facility for virus production and characterization; and Electron Microscopy and AMBIO imaging core facilities at the Charité Campus Mitte for services.

The authors declare no competing financial interests.

Correspondence should be addressed to Christian Rosenmund at christian.rosenmund@charite.de.

https://doi.org/10.1523/JNEUROSCI.1922-20.2020

Because CAZ proteins are densely positioned at the AZ, with many putative interaction sites between them, disentangling the functions of individual AZ proteins requires a multitude of genetic ablation and rescue analyses. The AZ protein core consists of Rab3-interacting molecule (RIM), Munc13, RIM-binding protein (RIM-BP), ELKS, α-Liprins, Piccolo, and Bassoon (Schoch and Gundelfinger, 2006; Sudhof, 2012). RIM is of particular interest, as investigations have shown its extensive interaction and regulatory effect on other AZ proteins. The two mammalian genes, *Rims1* and *Rims2*, synthesize five RIM isoforms, RIM1α/β, and RIM2$\alpha/\beta/\gamma$, whose domain content varies their interactions with Rab3, Munc13, and Ca^{2+} channels (Kaeser et al., 2008, 2012). Genetic deletion of both *Rim* genes shows that α- and β-RIMs directly interact with Ca^{2+} channels, and indirectly, via RIM-BP, target Ca^{2+} channels to release sites, as the absence of RIMs leads to an impaired presynaptic Ca^{2+} channel function, Ca^{2+} channel-vesicle coupling, Ca^{2+}-evoked release, and vesicular release probability (Hibino et al., 2002; Kiyonaka et al., 2007; Han et al., 2011, 2015; Kaeser et al., 2011; Graf et al., 2012; Hirano et al., 2017). In addition, α-RIMs and RIM1β promote the activity of the priming factor, Munc13, by interfering with priming-impeding Munc13 homodimerization (Betz et al., 2001; Deng et al., 2011; Camacho et al., 2017) and by recruiting Munc13 to the presynaptic AZ (Andrews-Zwilling et al., 2006). As Munc13s play a key role in determining the number of release sites and fusion-competent vesicles (Augustin et al., 999a,b; Sakamoto et al., 2018; Bohme et al., 2019), it is challenging to deconvolve the direct role of RIM1/2 in the SV cycle from its role in stabilizing Munc13 at the AZ.

RIM also ensures the integrity of AZ scaffolds with its large molecular interactors, such as RIM-BP (Acuna et al., 2016; Wu et al., 2019) and ELKS (S. S. Wang et al., 2016). RIM's role in determining AZ scaffold integrity manifest on an ultrastructural level. Cryo-electron tomographic experiments revealed fewer tethered vesicles and a lower vesicle density in RIM1α KO synaptosomes, suggesting a distinct role for RIM in vesicle localization close to the AZ membrane (Fernández-Busnadiego et al., 2013). This effect may be mediated by the dynamic tripartite complex of α-RIMs, Rab3, and Munc13 that targets vesicles to the release sites (Dulubova et al., 2005). Therefore, comparative ultrastructural evidence in RIM and Munc13-deficient neurons is necessary to dissect the Munc13-dependent and -independent roles of RIM in SV localization and docking at the AZ.

In our study, we aimed to disentangle RIM's direct role in the SV cycle at the AZ from its role in enabling the function of Munc13. Using genetic deletions, we systematically compared murine hippocampal synapses lacking RIM1/2 and/or Munc13-1, the predominant isoform of Munc13 in mouse CNS. Comparative analysis of neurotransmission by electrophysiology, as well as ultrastructural analysis by electron microscopy, revealed a Munc13-1-independent contribution of RIM to vesicular release probability and SV localization. Together, our results provide a deeper understanding of key AZ proteins function individually and in concert to ensure efficient neurotransmission.

Materials and Methods

Animals and maintenance. All animal experiments and maintenance were approved by Animal Welfare Committee of Charité-Universitätsmedizin Berlin and the Berlin state government agency for Health and Social Services (license no. T 0220/09). The *RIM1*^{flox}/*RIM2*^{flox} and *RBP1*^{flox}/*RBP2*^{flox} mouse line, a gift from the Thomas C. Südhof laboratory (Acuna et al., 2016), was crossed with C57BL/6N mice to generate the *RIM1*^{flox}/*RIM2*^{flox} mouse line (called RIM1/2^{flox}). The RIM1/2^{flox} animals were interbred, and the offspring at postnatal (P) days 0-2 were used to obtain the RIM1/2 control and conditional double KO (cDKO) neurons. *Munc13-1*$^{-/-}$ and *Munc13-1*$^{+/+}$ littermates at embryonic (E) day 18 were obtained by interbreeding of *Munc13-1*$^{+/-}$ mouse line on an FVB/N background. Here, we referred to *Munc13-1*$^{+/+}$ as Munc13-1 WT and to *Munc13-1*$^{-/-}$ as Munc13-1 KO. Moreover, the mouse line of *Munc13-2*$^{-/-}$/*Munc13-1*$^{+/-}$ on an FVB/N background (Camacho et al., 2017) was interbred to produce *Munc13-2*$^{-/-}$/*Munc13-1*$^{+/+}$ animals at E18. Gender of the animals used for experimentation was not distinguished.

Neuronal cultures and lentiviral infections. Micro-islands and continental astrocyte feeder layers were generated from cortices of P0-P1 C57BL/6N mice 2 weeks before the neuronal culture preparations as described previously (Arancillo et al., 2013). To generate neuronal cultures, the hippocampi from either P0-P2 RIM1/2^{flox} pups, or Munc13-1 WT, Munc13-1 KO, Munc13-2 KO embryos at E18 were dissected. After enzymatic digestion with papain solution (Worthington), neurons were mechanically dissociated. Neurons were counted and seeded on astrocytic feeder layers in Neurobasal-A medium (Invitrogen) supplemented with B-27 (Invitrogen), 50 IU/ml penicillin, and 50 μg/ml streptomycin (Invitrogen). For autaptic cultures, 3500 cells were seeded on coverslip glasses (30 mm) containing an astrocytic micro-island pattern to perform immunocytochemistry and electrophysiological recordings. For the mass cultures, 100,000 cells were plated on 6-well plates with astrocytic feeder layers to perform Western blot, and 100,000 cells were seeded on sapphire glasses (6 mm) with an astrocytic feeder layer for high-pressure freezing experiments.

After 1-2 DIV, neurons were transduced with lentiviral particles. RIM1/2 control and cDKO were generated from RIM1/2^{flox} hippocampal neurons infected with lentivirus containing inactive and active Cre recombinase tagged with EGFP (Kaeser et al., 2011). Short hairpin RNA (shRNA) target sequence (5′-GCCTGAGATCTTCGAGCTTAT-3′) for Munc13-1 was previously described (Deng et al., 2011). The shRNA sequence was cloned into a lentiviral shuttle vector that controlled its expression via a U6 promoter. A further human synapsin-1 promoter controlled the expression of an NLS-RFP protein to label infected neurons. The viral production was performed by the Viral Core Facility of the Charité-Universitätsmedizin Berlin. The titer of Munc13-1 KD shRNA was assessed by qPCR using LV900 Lentivirus Titration Kit (Applied Biological Materials).

Electrophysiology in the hippocampal autaptic culture. Whole-cell voltage-clamp recordings were performed on autaptic hippocampal neurons at DIV 15-20. Single neurons on micro-islands were selected and recorded at room temperature using Multiclamp 700B amplifier (Molecular Devices) under the control of Clampex 10.5 software. Axon Digidata 1550 digitizer (Axon Instruments) was used for data acquisition at 10 kHz sample rate with a low-pass Bessel filter at 3 kHz. Borosilicate glass pipettes with resistance between 2 and 4 MΩ were pulled with a micropipette puller device (Sutter Instruments). The pipettes were filled with intracellular solution containing the following (in mM): 136 KCl, 17.8 HEPES, 1 EGTA, 4.6 $MgCl_2$, 4 Na_2ATP, 0.3 Na_2GTP, 12 creatine phosphate, and 50 U ml^{-1} phosphocreatine kinase (~300 mOsm, pH 7.4). The extracellular solution contained the following (in mM): 140 NaCl, 2.4 KCl, 10 HEPES, 10 glucose, 2 $CaCl_2$, and 4 $MgCl_2$ (~300 mOsm, pH 7.4) and was permanently exchanged with a fast flow system. During the recordings, the access resistance was compensated at 70%. The neurons with <10 MΩ series resistance were used for the recordings. The EPSCs were induced by 2 ms depolarization from holding potential of −70 to 0 mV. Extracellular solution containing 3 μM NBQX was used to distinguish glutamatergic from GABAergic neurons. To identify spontaneous events, traces recorded at a holding potential of −70 mV were filtered at 1 kHz, and mEPSCs were detected by a template algorithm in Axograph X (Axograph Scientific). False-positive events were excluded by subtracting events detected from traces in the presence of NBQX. The readily releasable pool (RRP) of SVs was estimated by application of 500 mM sucrose solution for 5 s. The charge of the transient response component was used to determine the RRP size (Rosenmund and Stevens, 1996). The vesicular release probability (P_{vr}) was determined by dividing the EPSC charge by the sucrose-induced charge.

Paired-pulse protocol was induced by two sequential action potentials (APs) with 25 ms interstimulus interval. Paired-pulse ratio was calculated by dividing the amplitude of the second EPSC by the amplitude of the first EPSC. The RRP augmentation was assessed by calculating the ratio of the sucrose-induced charge 2 s after 10 Hz stimulation with 50 APs to the baseline sucrose-induced charge. Electrophysiological recordings were analyzed using Axograph X (Axograph Scientific). Standard Hill equation $Y = M/[1 + (K_d/X)^n]$ was performed to fit the dose–response relationship of electrophysiological parameters as a function of the protein expression (Arancillo et al., 2013). In the equation, Y is response amplitude, X is Munc13-1 relative expression to VGLUT1, M is the maximum response, K_d is the dissociation constant, and n is cooperativity.

High-pressure freezing and transmission electron microscopy. The 6 mm carbon-coated sapphire glass-containing neurons (DIV 15-16) were frozen in high-pressure freezing device (Leica Microsystems, EM ICE or HPM100). After freezing, the samples were transferred into a liquid nitrogen chamber. Each sample was moved inside the AFS2 automated freeze-substitution device (Leica Microsystems) containing cryovials for each sapphire with the following solution: 1% osmium tetroxide, 1% glutaraldehyde, 1% ddH_2O in anhydrous acetone. The AFS2 device was programmed for a 2 d protocol with a stepwise heating starting at −90° C for 4-5 h, −90°C to −20°C for 14 h, −20°C for 12 h, and −20°C to 20° C for 8 h. Subsequently, samples were washed with anhydrous acetone and were treated for 1 h with 0.1% uranyl acetate to get contrast enhancement. In the last step, samples were embedded in EPON and baked at 60°C for 48 h to polymerize. The serial sectioning was performed with an ultramicrotome (Leica Microsystems) to obtain 40 nm sample thickness. Samples were collected in formvar-coated single-slot grids (Science Services). Just before the imaging, samples were contrasted for 3-5 min in 2% uranyl acetate and for 30 s in 0.3% lead citrate in ddH_2O. The images were obtained with a FEI Tecnai G20 transmission electron microscopy operating at 200 keV. Synapses were selected based on detectable postsynaptic density (PSD). For each experiment, ~50 profiles per group were imaged with (2048 - × 2048 pixels) CCD camera (Olympus) at 0.73 nm pixel size. The analysis was performed blind using ImageJ software and MATLAB. AZ length was defined as the membrane opposite to the PSD. SVs were identified as visible circular membranes structures with a diameter of ~25-50 nm in a single plane of a 2D micrograph. The visualization of membranes was aided by increasing contrast. To avoid bias, the analysis for each experiment was performed by one person who was blind to the experimental groups. The SVs that were directly in contact with the AZ membrane were marked as docked SVs. SVs not directly in contact with the AZ membrane, but residing within 100 nm of the AZ, were identified and their shortest distance to the AZ membrane was measured (Watanabe et al., 2013). To facilitate the presentation and discussion of our findings with regard to changes in SV localization as a function of RIM/Munc13-1 protein level manipulations, we used the term "proximal" to refer to the SVs up to 20 nm from the AZ membrane, whereas the SVs at >20-100 nm from the AZ were referred to as "distal."

Immunostaining and quantification. Autaptic neurons at DIV 15-20 were fixed for 10 min in 4% PFA, permeabilized with 0.1% PBS-Tween-20 solution and blocked with 5% normal donkey serum. Rabbit anti-VGLUT1 (SYSY 135302) and Guinea-pig anti-Munc13-1 (SYSY 126104) primary antibodies were used for coimmunostaining to detect Munc13-1 presynaptic expression. The primary antibodies were labeled with AlexaFluor-488 anti-rabbit IgG, as well as AlexaFluor-647 anti-guinea pig both in donkey serum (Jackson ImmunoResearch Laboratories), respectively. Single neurons on the astrocytic micro-islands were imaged using a Nikon scanning confocal microscopy A1Rsi with a × 60 oil immersion objective. The z-series images at 0.3 µm depth were obtained at equal exposure times with 1024 × 1024 pixels resolution and at the pixel size of 0.2 µm. The analysis was performed blind in ImageJ software by drawing ROIs of 50 synapses per neuron. ROIs were defined by staining for the SV marker VGLUT1. Munc13-1 fluorescence intensity for each synapse was divided to the corresponding fluorescence intensity of VGLUT1; ~30 neurons per group were analyzed in three independent cultures, and the data were normalized to the control of each experiment.

Western blot. Protein lysates for Western blot were obtained from mass culture neurons at DIV 15-20. The lysis solution contained 50 mM Tris/HCl, pH 7.6, 150 mM NaCl, 1% Nonidet P-40, 0.5% sodium deoxycholate, and 4% of Complete Protease Inhibitor (Roche Diagnostics). Lysed cells were scrubbed from plates and centrifuged to remove the debris from the protein-content supernatant; 30 µg of proteins was loaded to SDS-polyacrylamide gel, separated after electrophoresis, and transferred to nitrocellulose paper (Bio-Rad). The proteins were labeled with primary antibodies during overnight incubation at 4°C. The mouse anti-Tubulin III antibody (Sigma Millipore, T8660) was used to label Tubulin III as a loading control. Rabbit anti-Munc13-1 (SYSY 126103) or rabbit anti-RIM1/2 (SYSY 140203) was used to label Munc13-1 and RIM1/2, respectively. Goat IgG HRP-conjugated antibody (Jackson ImmunoResearch Laboratories) was used for the labeling of primary antibodies and was detected by ECL solution (GE Healthcare Biosciences). To quantify the proteins' expression level, the ratio of either Munc13-1 or RIM1/2 signal density to the corresponding Tubulin III signal density was normalized to the control group in three independent cultures.

Statistical analysis. All data were plotted with GraphPad Prism 7, and represented in bar plots as mean ± SEM. First, the data were tested for normality with D'Agostino-Pearson test. If they did not pass the parametric assumption, Kruskal–Wallis test followed by Dunn's test was performed for multiple comparison, and Mann–Whitney U test was applied for comparison of two unpaired datasets. In case the parametric assumption was passed, ordinary one-way ANOVA followed by Tukey's test for the multiple comparison, and Student's t test for two datasets were applied. The α level was set at 0.05. In the manuscript, the absolute values are shown as mean ± SEM, and n is the number of data points/number of cultures. The overview statistics including sample size, mean, SEM, p value, and result statistics for each figure are shown in Extended Data Figure 1-1 to Figure 7-1.

Results

RIM1/2 and Munc13-1 differentially contribute to SV distribution at the AZ

In order to investigate the expression levels of RIM1/2 and Munc13-1 in our experimental system, we generated RIM1/2 control and cDKO neurons by transducing continental hippocampal cultures from RIM1/2^{flox} mice (Kaeser et al., 2011) with either inactivated Cre-recombinase (ΔCre) or Cre-recombinase (Cre), respectively. After 14 DIVs, we assessed protein expression of RIM1/2 and Munc13-1 in RIM1/2 control (ΔCre) and RIM1/2 cDKO (Cre) using Western blot analysis. We found that Cre expression in RIM1/2^{flox} neurons leads to undetectable RIM1/2 levels, verifying successful removal of RIM1/2 proteins (Fig. 1*A*, left). Consistent with the previous reports (Deng et al., 2011), loss of RIM1/2 also resulted in severely reduced Munc13-1 protein levels (Fig. 1*A*, right), confirming the necessity of RIM in recruiting and stabilizing Munc13-1 at the AZ (Andrews-Zwilling et al., 2006).

To identify the specific effects of RIM1/2 and Munc13-1 on synapse ultrastructure, we cryo-preserved cultures derived from *Munc13-1*$^{-/-}$ and *Munc13-1*$^{+/+}$ neurons and RIM1/2 cDKO and control neurons under high pressure. We imaged 40 nm sections of synaptic profiles at high magnification in transmission electron microscopy (TEM) (Fig. 1*C*) and analyzed standard ultrastructure parameters, including PSD length, number of SVs docked at the AZ membrane (defined as the membrane opposite to the PSD), and the shortest distance of undocked vesicles to the AZ membrane (Fig. 1*B*). The AZ length was not different between the KO groups and their controls (Fig. 1*F*,*G*; RIM1/2 ΔCre: 281.8 ± 12.8 nm, $n = 153/3$; RIM1/2 Cre: 286.7 ± 8.95 nm, $n = 161/3$, $p = 0.094$; Munc13-1 WT: 312.3 ± 10.72 nm, $n = 148/3$;

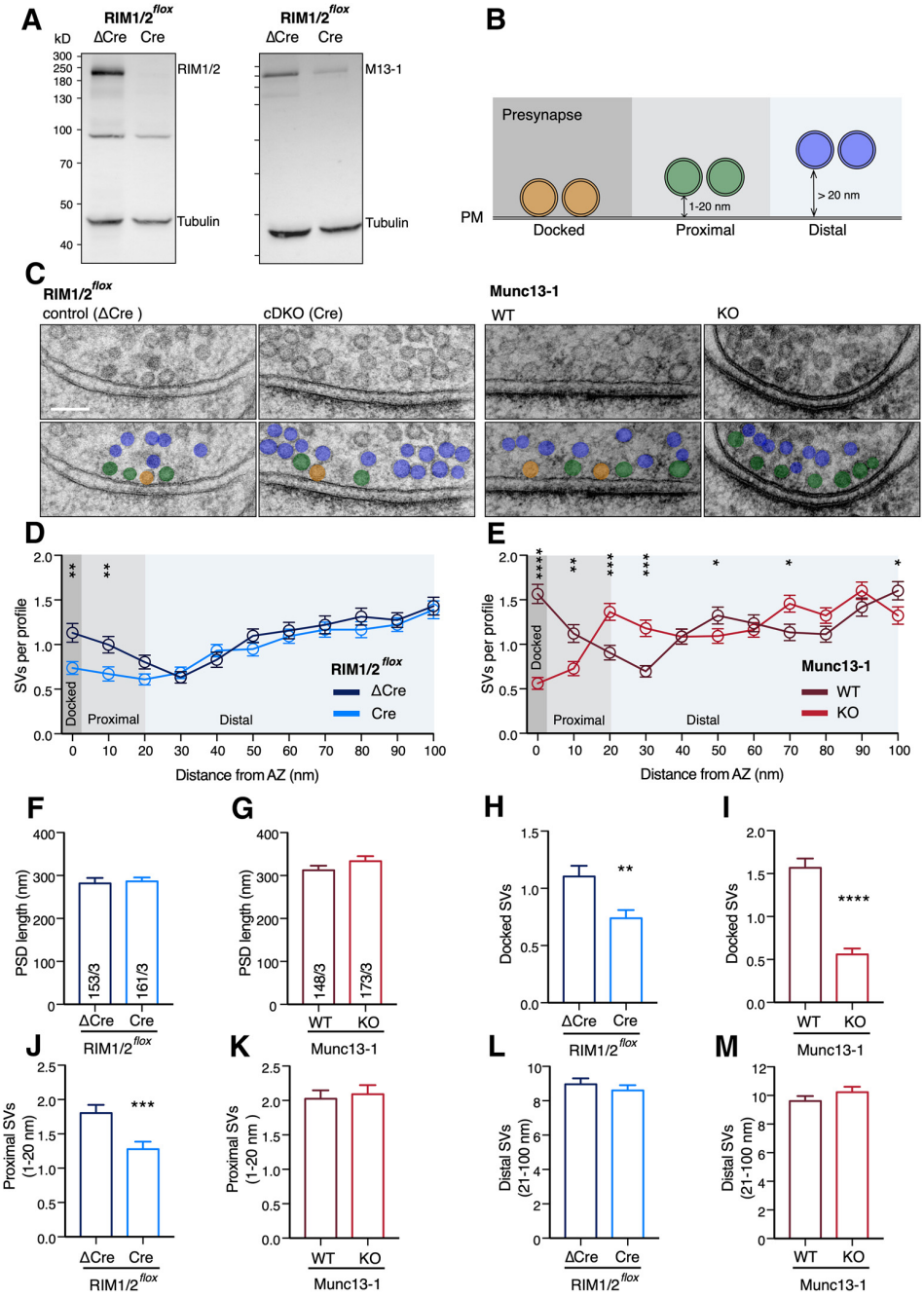

Figure 1. RIM1/2 and Munc13-1 differentially affect SV distribution and docking. ***A***, Immunoblots of lysates from RIM1/2^{flox} hippocampal neurons infected with ΔCre (control) and Cre recombinase (cDKO) detecting RIM1/2 (left) and Munc13-1 (right) expression. Tubulin expression was used as a loading control. Left, Markers designate the molecular weight. ***B***, Diagram represents the analysis of SVs based on their distance from AZ membrane. P.M., plasma membrane. ***C***, Example TEM images displaying the presynaptic area of RIM1/2 control and cDKO (left), as well as Munc13-1 WT and KO (right). Top, Raw images. Bottom, Vesicles are color-coded according to their distance to the AZ membrane: docked SVs (orange), proximal SVs (green), and distal SVs (blue). Scale bar, 100 nm. Additional example pictures are represented in Extended Data Figure 1-2. ***D***, ***E***, Plots represent the number of SVs as a function of distance from the AZ membrane for RIM1/2 cDKO (***D***) and Munc13-1 KO (***E***) synapses, compared with their corresponding control (binned to 10 nm). ***F-M***, Bar plots represent the mean PSD length (***F***,***G***), docked SVs (***H***, ***I***), proximal SVs (1-20 nm) (***J***,***K***), and distal SVs (21-100 nm) (***L***,***M***) for RIM1/2 cDKO and Munc13-1 KO synapses compared with their corresponding controls. The data are obtained from the same experimental settings for all the electron microscopy analysis (RIM1/2 control: 153/3 and RIM1/2 cDKO: 161/3; Munc13-1 WT: 148/3 and Munc13-1 KO: 173/3) indicated in ***F*** and ***G***. The numbers are obtained from three independent cultures. Values indicate mean ± SEM. $*p \leq 0.05$; $**p \leq 0.01$; $***p \leq 0.001$; $****p \leq 0.0001$; nonparametric *t* test, followed by Mann–Whitney test. For the statistical overview, see also the table in Extended Data Figure 1-1.

Munc13-1 KO: 333.4 ± 12.03 nm, $n = 173/3$, $p = 0.382$, Mann–Whitney test). RIM1/2 cDKO presynaptic terminals showed a 30% reduction in docked SVs per AZ compared with controls (Fig. 1*H*; RIM1/2 ΔCre: 1.10 ± 0.09, $n = 153/3$; RIM1/2 Cre: 0.73 ± 0.07, $n = 161/3$, $p = 0.002$, Mann–Whitney test). On the other hand, Munc13-1 KO synapses displayed a ~70% reduction in SV docking (Fig. 1*I*; Munc13-1 WT: 1.57 ± 0.10, n = 148/3; Munc13-1 KO: 0.56 ± 0.07, $n = 173/3$, $p < 0.0001$, Mann–Whitney

test). Thus, high-pressure freezing and TEM experiments revealed SV docking deficits in cultures lacking either Munc13-1 or RIM1/2, albeit to a different extent.

Earlier studies have proposed a role for RIM in tethering SVs close to the AZ membrane (Fernández-Busnadiego et al., 2013). While we cannot assess tethers in our high-pressure frozen samples, we investigated the respective roles of RIM1/2 and Munc13-1 in the localization of nondocked SVs within 100 nm of the AZ membrane. RIM1/2 cDKO presynaptic terminals displayed a reduced number of SVs within the first 20 nm of the AZ membrane (Fig. 1*D*,*J*; RIM1/2 ΔCre: 1.80 ± 0.12, $n = 153/3$; RIM1/2 Cre: 1.28 ± 0.10, $n = 161/3$, $p = 0.0004$, Mann–Whitney test), but no change in density of SVs from >20 nm up to 100 nm from the AZ membrane (Fig. 1*D*,*L*; RIM1/2 ΔCre: 8.96 ± 0.35, $n = 153/3$; RIM1/2 Cre: 8.60 ± 0.3, $n = 161/3$, $p = 0.675$, Mann–Whitney test). Therefore, to facilitate the discussion about the relative SV localization, we defined 20 nm as a border to separate "proximal" SVs (1-20 nm) from the "distal" SVs (21-100 nm) to the AZ membrane (Fig. 1*B*).

On the other hand, Munc13-1-deficient presynaptic terminals showed no change in AZ-proximal SV number because of a significant SV accumulation near the AZ membrane (Fig. 1*E*,*K*; Munc13-1 WT: 2.03 ± 0.12, $n = 148/3$; Munc13-1 KO: 2.09 ± 0.13, $n = 173/3$, $p = 0.853$, Mann–Whitney test). The different phenotype of two KOs in localization of SVs at the AZ-proximal region relative to their controls proposes that RIM localizes vesicles in the proximity to the AZ. Similar to RIM1/2 cDKO synapses, Munc13-1 KO synapses showed no change in distal SVs (Fig. 1*E*,*M*; Munc13-1 WT: 9.61 ± 0.34, $n = 148/3$; Munc13-1 KO: 10.23 ± 0.38, $p = 0.677$, $n = 173/3$, Mann–Whitney test). Therefore, neither RIM1/2 nor Munc13-1 is specifically involved in distal SV localization.

RIM1/2 localizes SVs in the AZ proximity independent of Munc13-1

Since RIM1/2 deletion also results in a partial reduction of Munc13-1 protein levels (Deng et al., 2011), we aimed to separate RIM1/2 and Munc13-1 function by further reducing Munc13-1 protein in the RIM1/2 cDKO and control neurons using an shRNA knockdown (KD) approach (Fig. 2). Western blot analysis revealed a nearly complete abolishment of Munc13-1 protein in neuronal lysates infected with the shRNA (Fig. 2*A*). As expected, RIM1/2 proteins were diminished by ~90% in RIM1/2 cDKO lysates (Fig. 2*B*). We also noted that KD of Munc13-1 in control neurons displayed a small but detectable reduction in RIM1/2 protein levels (Fig. 2*B*).

The KD of Munc13-1 in control neurons resulted in a decreased number of docked SVs compared with its control (Fig. 2*F*; RIM1/2 ΔCre + Scramble: 2.13 ± 0.11, $n = 157/3$; RIM1/2 ΔCre + Munc13-1 KD: 1.42 ± 0.09, $n = 148/3$, $p = 0.0002$, Kruskal–Wallis test). While SV docking was reduced by 30% in RIM1/2 cDKO synapses, the additional KD of Munc13-1 in RIM1/2 cDKO caused a more severe docking impairment (Fig. 2*F*; RIM1/2 Cre + Scramble: 1.61 ± 0.1, $n = 168/3$; RIM1/2 Cre + Munc13-1 KD: 0.95 ± 0.07, $n = 167/3$, $p < 0.0001$, Kruskal–Wallis test). Hence, both RIM and Munc13-1 play a substantial role in SV docking. Moreover, while the total number of SVs within AZ-proximal region of Munc13-1 KD in control neurons did not alter (Fig. 2*D*,*E*,*G*), it decreased in RIM1/2 cDKO synapses compared with the control (Fig. 2*D*,*E*,*G*; RIM1/2 ΔCre + Scramble: 2.53 ± 0.13, $n = 157/3$; RIM1/2 ΔCre + Munc13-1 KD: 2.95 ± 0.18, $n = 148/3$, $p > 0.999$; RIM1/2 Cre + Scramble: 1.95 ± 0.13, $n = 168/3$, $p = 0.002$, Kruskal–Wallis test). Interestingly, Munc13-1 KD had no further effect on AZ-proximal SV number in RIM1/2 cDKO synapses (Fig. 2*D*,*E*,*G*; RIM1/2 Cre + Scramble: 1.95 ± 0.13, $n = 168/3$, RIM1/2 Cre + Munc13-1 KD: 1.98 ± 0.14, $n = 167/3$, $p > 0.999$, Kruskal–Wallis test), illustrating a Munc13-1-independent role of RIM in positioning SVs within close proximity to the AZ. In addition, the SV number in the AZ-distal region was not affected by the loss of RIM1/2, Munc13-1, or both (Fig. 2*D*,*E*,*H*; Kruskal–Wallis (H) = 1.92, $p = 0.587$). Overall, our data demonstrate that RIM localizes SVs in proximity to the AZ in a Munc13-1-independent manner, while both RIM1/2 and Munc13-1 are required for SV docking.

Deletion of RIM1/2 severely impairs SV priming and neurotransmitter release in glutamatergic hippocampal autaptic neurons

Based on our findings that RIM1/2 influences SV docking and SV localization near the AZ membrane, we asked how RIM1/2 and Munc13-1 contribute to SV priming and neurotransmitter release in RIM1/2 or Munc13-1-deficient glutamatergic autaptic neurons. To examine how loss of RIM1/2 affects Munc13-1 protein levels at the synapse, we performed quantitative immunocytochemistry. By normalizing Munc13-1 immunofluorescence intensity to the corresponding signals from the SV marker VGLUT1 (Camacho et al., 2017), we found that Munc13-1 levels were reduced by ~70% in the presynaptic terminals of autaptic RIM1/2 cDKO neurons (Fig. 3*B*; $t_{(38)} = 9.25$, $p < 0.0001$, Student's *t* test). This supports the notion that RIM1/2 stabilizes Munc13-1 at the AZ (Andrews-Zwilling et al., 2006).

To compare the roles of RIM and Munc13-1 in SV priming activity, we estimated the size of the RRP of SVs. RRP of RIM1/2 cDKO or Munc13-1 KO autaptic neurons and their respective controls was estimated by measuring the transient postsynaptic charge component evoked by the pulsed application of hypertonic sucrose (Rosenmund and Stevens, 1996) (Fig. 3*C*). Compared with the control neurons, RRP size was severely reduced by Munc13-1 deletion (~95%) or RIM1/2 deletion (~88%) (Fig. 3*D*; RIM1/2 ΔCre: 0.7 ± 0.1 nC, $n = 41/5$; RIM1/2 Cre: 0.08 ± 0.01 nC, $n = 51/5$, $p < 0.0001$; Munc13-1 WT: 0.69 ± 0.09 nC, $n = 27/3$; Munc13-1 KO: 0.04 ± 0.006 nC, $n = 35/3$, $p < 0.0001$, Mann–Whitney test). Thus, the presence of RIM1/2 and Munc13-1 is required for efficient SV priming to occur, which goes in line with the SV docking role of RIM1/2 and Munc13-1 (Fig. 1). However, the impairment of SV priming was more drastic than the impairment in SV docking in both KOs.

To address the impact of RIM1/2 on Ca^{2+}-evoked release in autaptic neurons, we analyzed the AP-evoked EPSCs (Fig. 3*E*). The EPSC amplitude in RIM1/2 cDKO autaptic neurons was reduced by ~97%, similar to the loss of EPSC amplitude observed in Munc13-1 KO neurons (Fig. 3*F*; RIM1/2 ΔCre: 6.3 ± 0.72 nA, $n = 59/5$; RIM1/2 Cre: 0.18 ± 0.05 nA, $n = 56/5$, $p < 0.0001$; Munc13-1 WT: 7.1 ± 0.89 nA, $n = 32/3$; Munc13-1 KO: 0.19 ± 0.03 nA, $n = 46/3$, $p < 0.0001$, Mann–Whitney test). While a large portion of the EPSC amplitude decrease in the absence of RIM1/2 is likely attributable to reduced SV priming activity, it is known that RIM1/2 also regulates Ca^{2+} channel recruitment (Han et al., 2011; Kaeser et al., 2011). We thus predicted that RIM1/2 cDKO autaptic neurons also had less efficacious Ca^{2+} secretion-coupling than Munc13-1 KO neurons, affecting vesicular release probability (P_{vr}). We computed the P_{vr} by calculating the ratio of the EPSC charge to the sucrose-induced charge. P_{vr} was decreased by ~82% for RIM1/2 cDKO,

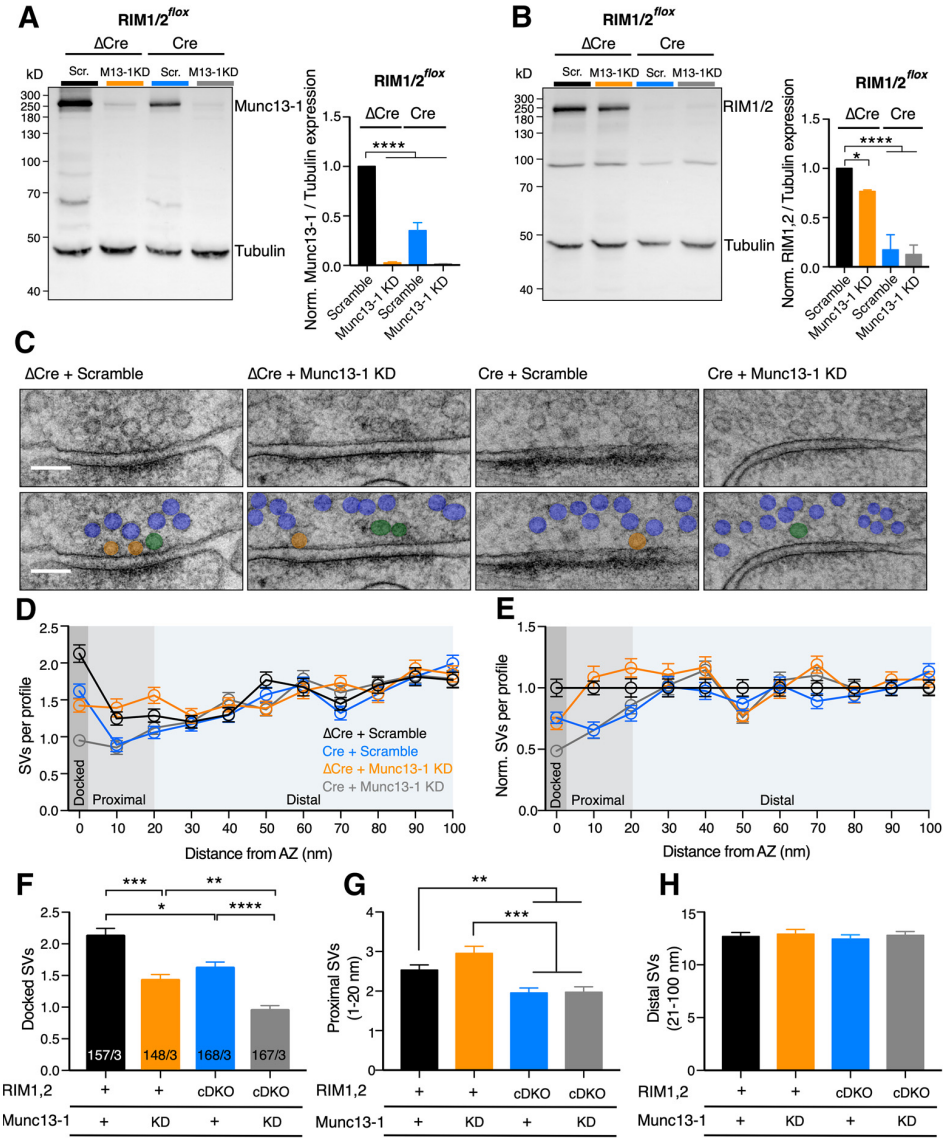

Figure 2. Munc13-1-independent impact of RIM on SV localization. ***A***, ***B***, Immunoblots (left) and bar plots (right) represent the expression of Munc13-1 (***A***) and RIM1/2 (***B***) in RIM1/2^{flox} cultures infected with ΔCre + Scramble (Scr.) shRNA (black), ΔCre + 40 × 10^5 infectious units (IU) Munc13-1 KD shRNA (orange), Cre + Scramble shRNA (blue), and Cre + 40 × 10^5 Munc13-1 shRNA (gray). Tubulin expression was used as a loading control. Molecular weight markers are indicated on blots. The analysis was performed from three independent cultures. Significance was calculated using one-way ANOVA followed by Tukey's *post hoc* test (***A***: $F_{(3,8)} = 133.8$, $p < 0.0001$; ***B***: $F_{(3,8)} = 48.07$, $p < 0.0001$). ***C***, Example TEM images of RIM1/2^{flox} hippocampal cultures infected as in ***A*** and ***B***. Top, Raw images. Bottom, Vesicles are color-coded according to their distance to the AZ membrane: docked SVs (orange), proximal SVs (green), distal SVs (blue). Scale bar, 100 nm. Additional example pictures are represented in Extended Data Figure 2-2. ***D***, ***E***, Plot represents the SV number as a function of distance from the AZ membrane (binned 10 nm; ***D***) and the same values normalized to the control (binned to 10 nm; ***E***). ***F–H***, Bar plots displaying the mean number of docked SVs (***F***), proximal SVs (1-20 nm) (***G***), and distal SVs (21-100 nm) (***H***). Bar graph label "+" indicates endogenous expression of RIM1/2 or Munc13-1. "KD" refers to Munc13-1 KD. "cDKO" refers to RIM1/2-deficient neurons. Number of synaptic profiles for ***D–H*** are indicated in ***F***. Values indicate mean ± SEM. $*p \leq 0.05$; $**p \leq 0.01$; $***p \leq 0.001$; $****p \leq 0.0001$; nonparametric one-way ANOVA with Kruskal–Wallis test followed by Dunn's *post hoc* test. For the statistical overview, see also the table in Extended Data Figure 2-1.

while the loss of Munc13-1 led to a reduction of P_{vr} by only ~56% (Fig. 3*G*; RIM1/2 ΔCre: 6.4 ± 0.56%, $n = 41/5$; RIM1/2 Cre: 1.11 ± 0.3%, $n = 50/5$, $p < 0.0001$; Munc13-1 WT: 8.08 ± 0.74%, $n = 27/3$; Munc13-1 KO: 3.50 ± 0.63%, $n = 35/3$, $p < 0.0001$, Mann–Whitney test). We independently probed the efficiency of release by recording postsynaptic responses to paired-pulse stimulation protocols. Consistent with our observations of P_{vr} changes, we noticed a strong facilitation in the RIM1/2-deficient neurons (Fig. 3*H*), which confirms the stark decrease in release probability. Munc13-1-deficient neurons, in line with the less drastic P_{vr} loss, showed a moderate increase in facilitation (Fig. 3*H*; RIM1/2 ΔCre: 1.13 ± 0.05, $n = 57/5$; RIM1/2 Cre: 1.63 ± 0.11, $n = 54/5$, $p < 0.0001$; Munc13-1 WT: 1.13 ± 0.06, $n = 32/3$; Munc13-1 KO: 1.34 ± 0.06, $n = 43/3$, $p = 0.01$, Mann–Whitney test).

We also examined the impact of RIM1/2 and Munc13-1 on spontaneous release by analyzing the frequency of mEPSCs (Fig. 3*I*). Consistent with the reduced priming function, loss of both RIM and Munc13-1 proteins strongly impaired mEPSC frequency (Fig. 3*J*; RIM1/2 ΔCre: 6.67 ± 0.72 Hz, $n = 48/5$; RIM1/2 Cre: 1.48 ± 0.33 Hz, $n = 49/5$, $p < 0.0001$; Munc13-1 WT: 8.62 ± 0.92 Hz, $n = 31/3$; Munc13-1 KO: 0.72 ± 0.23 Hz, $n = 42/3$, $p < 0.0001$, Mann–Whitney test).

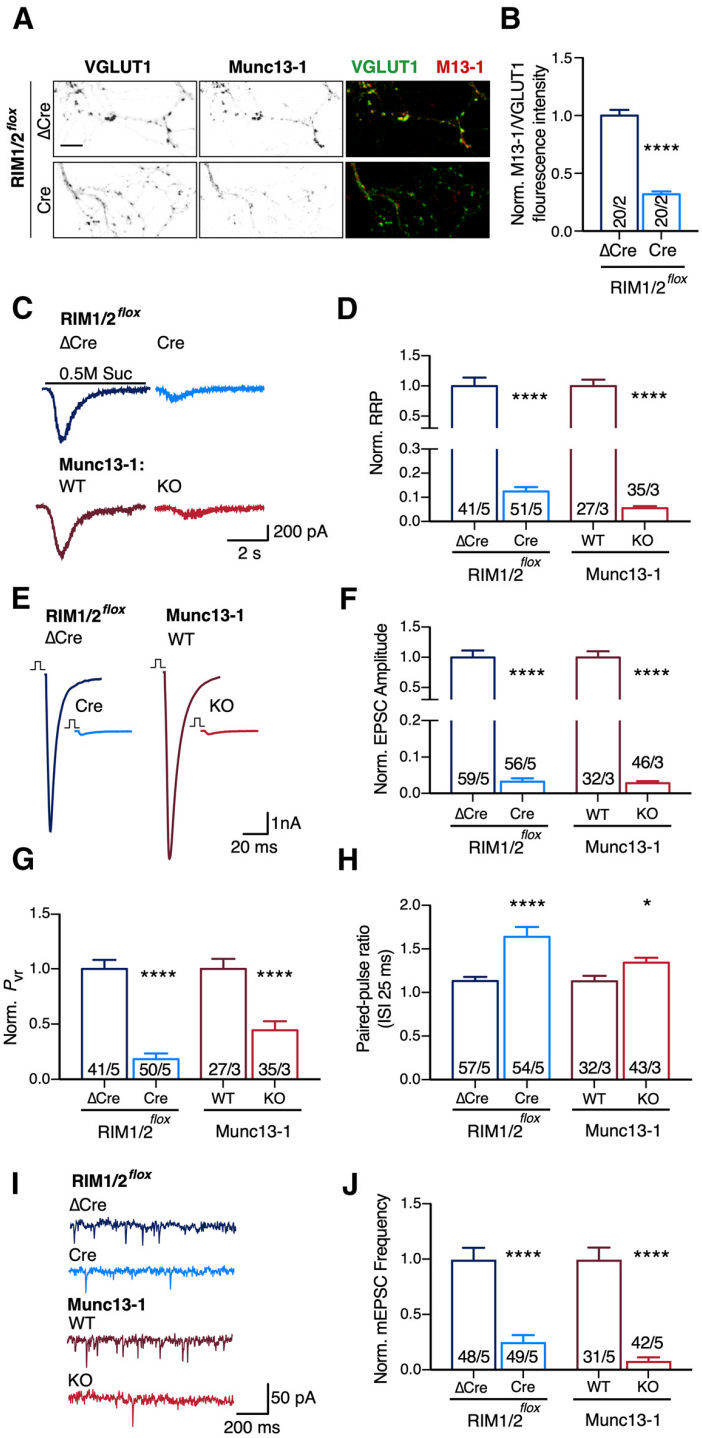

Figure 3. Comparison of synaptic properties of murine RIM1/2- and Munc13-1 KOs in autaptic hippocampal neurons. ***A***, Representative confocal microscopy projections display the immunofluorescence for Munc13-1 and VGLUT1 in RIM1/2 control and cDKO autaptic neurons. Scale bar, 10 µm. ***B***, Bar plot represents the ratiometric fluorescence intensity levels of Munc13-1 to VGLUT1 normalized to the control. Significance was calculated using Student's *t* test ($t_{(38)} = 9.25$, $p < 0.0001$). ***C***, Example traces of current induced by application of hypertonic solution (0.5 M sucrose [Suc], 5 s) to estimate the size of RRP in neurons derived from RIM1/2 control (navy blue), RIM1/2 cDKO (light blue), Munc13-1 WT (dark red), and Munc13-1 KO (light red). ***D***, Bar plots represent the normalized mean of RRP size (sucrose charge transfer). ***E***, Example traces of EPSCs from the same experimental groups as in ***C***. ***F***, Bar plot represents the normalized mean of EPSC amplitude. ***G***, Bar plot represents the normalized vesicular release probability calculated by dividing the charge of EPSC to the sucrose charge. ***H***, Bar plot represents the paired-pulse ratio (with an interstimulus interval of 25 ms). ***I***, Example traces of spontaneous release events from the same experimental groups as in ***C***. ***J***, Bar plot represents the normalized mean frequency of mEPSCs. All of the bar plots are normalized to the corresponding controls, except the paired-pulse ratio. Significances were calculated between the RIM1/2 control and cDKO (navy blue and light blue), and between Munc13-1 WT and KO (dark red and light red) using nonparametric *t* tests, followed by a Mann–Whitney test. All numbers in bars indicate the cell number/culture number. Data indicate normalized mean ± SEM. $*p \leq 0.05$. $****p \leq 0.0001$. For the absolute values and statistical overview, see also the table in Extended Data Figure 3-1.

These results confirm that both RIM1/2 and Munc13-1 are required for neurotransmission. While our data verify previous findings that both RIM1/2 and Munc13-1 regulate SV priming and release efficiency, we extend these findings by demonstrating the relative contributions of RIM1/2 and Munc13-1 to each of these processes. We found that RIM plays a major role in determining vesicular release probability and Munc13 predominantly controls vesicle priming.

RIM1/2 cDKO loss of function does not depend on Munc13-1 concentrations

RIM influences Munc13-1 function by maintaining overall Munc13-1 protein levels in the synapse (Fig. 3*A*) and by activating Munc13-1 through disrupting the Munc13-1 homodimers (Deng et al., 2011; Camacho et al., 2017). To better understand the relative weight of these two functions of RIM and to gain a better mechanistic understanding of RIM's role in Munc13-1-mediated vesicle priming, we performed a graded shRNA-mediated KD of Munc13-1. To do so, cultures were infected with five doses of Munc13-1 shRNA ranging from 2 to 40×10^5 infectious units (IU). KD efficiency was assessed by both immunoblotting the hippocampal lysates (Fig. 4*A*) and immunocytochemistry on autaptic hippocampal cultures (Fig. 4*C*). Both analyses confirmed that by elevating the concentration of shRNA, Munc13-1 protein level was reduced in a dose-dependent manner, ranging from 70% to 95% (Fig. 4*B*,*D*).

We then proceeded by comparing RRP sizes between the groups and the control (Fig. 5*A*,*B*). Strikingly, despite similar Munc13-1 levels (30% of control) in both RIM1/2 cDKO and lowest dose of Munc13-1 shRNA, the 2×10^5 IU Munc13-1 shRNA did not significantly alter the RRP size (Fig. 5*B*; RIM1/2 ΔCre + Scramble: 0.42 ± 0.05 nC, $n = 60/6$; RIM1/2 ΔCre + Munc13-1 shRNA 2×10^5 IU: 0.40 ± 0.06, $n = 44/4$, $p > 0.999$, Kruskal–Wallis test). Only at higher doses of shRNA, when Munc13-1 protein levels were reduced by 80%-95%, the deficit in SV priming reached similar

←

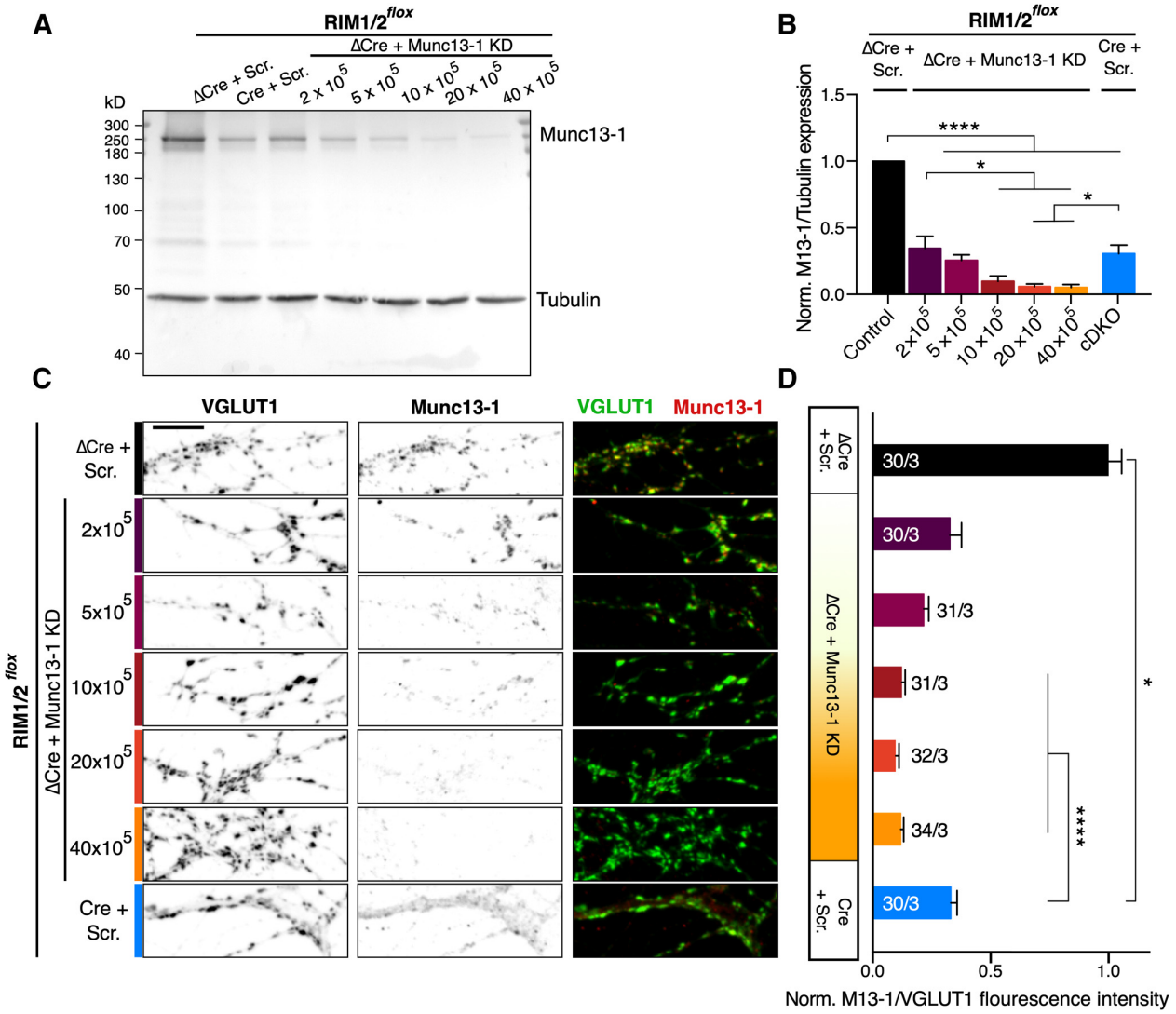

Figure 4. Munc13-1 titration in hippocampal neurons. ***A***, Immunoblot detecting Munc13-1 expression in RIM1/2^{flox} lysates from cultured hippocampal neurons infected with ΔCre + Scramble (Scr.) shRNA as control, ΔCre + Munc13-1 KD shRNAs (2-40 × 10^5 IU) to produce Munc13-1 dose gradients, and Cre recombinase + Scramble shRNA to create RIM1/2 cDKO. Tubulin expression was used as a loading control. Left, Molecular weight markers. ***B***, Bar plot represents ratiometric quantification of Munc13-1 expression levels to tubulin. Data were collected from three independent cultures and normalized to the corresponding control. Significances were calculated using one-way ANOVA followed by Tukey's *post hoc* test ($F_{(6,14)} = 46.79$, $p < 0.0001$). $*p \leq 0.05$. $****p \leq 0.0001$. ***C***, Representative confocal microscopy projections display immunofluorescence intensity of Munc13-1 and VGLUT1 in the same experimental groups as in ***A***. Scale bar, 10 µm. ***D***, Horizontal bar plot represents the ratiometric fluorescence intensity levels of Munc13-1 to VGLUT1 normalized to the control. For each neuron, ~50 synapses were measured and averaged. Statistical significances are represented only in comparison with RIM1/2 cDKO. Significances and *p* values were calculated with a nonparametric one-way ANOVA with Kruskal–Wallis test followed by Dunn's *post hoc* test ($H = 128.2$, $p < 0.0001$). $*p \leq 0.05$. $****p \leq 0.0001$. Data indicate normalized mean ± SEM. For the statistical overview, see also the table in Extended Data Figure 4-1.

levels to RIM1/2 cDKO (Fig. 5*B*). Assuming that the role of RIM in priming is confined to Munc13-1 activation (Deng et al., 2011), our data indicate that RIM1/2 increases the effectiveness of Munc13-1 in SV priming by approximately fourfold.

When we compared the effect of graded Munc13-1 KD on evoked responses and spontaneous release events, we found that EPSC amplitudes and mEPSC frequency followed the reduction of RRP size (Fig. 5*A–D*). However, only with the KD of Munc13-1 protein level by >90%, the EPSC amplitude and mEPSC frequency reached the reduced level of the RIM1/2 cDKO neurons (Fig. 5*C*,*D*). Thus, RIM1/2 cDKO revealed the most severe phenotype in both parameters of EPSC amplitude and mEPSC frequency compared with the control.

In turn, P_{vr} was not majorly affected by Munc13-1 levels, whereas we observed a significant reduction in P_{vr} in RIM1/2 cDKO neurons (Fig. 5*E*). This suggests that reducing Munc13-1 levels does not impair Ca^{2+}-secretion coupling, in contrast to the effect of eliminating RIM1/2.

By plotting SV priming and release as a function of Munc13-1 protein levels at the presynapse, we created dose–response plots of Munc13-1 for RRP size, EPSC amplitude, mEPSC frequency, and P_{vr} (Fig. 5*F–I*). We fitted the data from RRP size, EPSC amplitude, and mEPSC frequency measurements with a standard Hill equation (Arancillo et al., 2013) (see also Materials and Methods) to determine the relative sensitivity of synaptic function to Munc13-1 protein level and to define putative cooperativities. The fits show that the half-maximal SV priming,

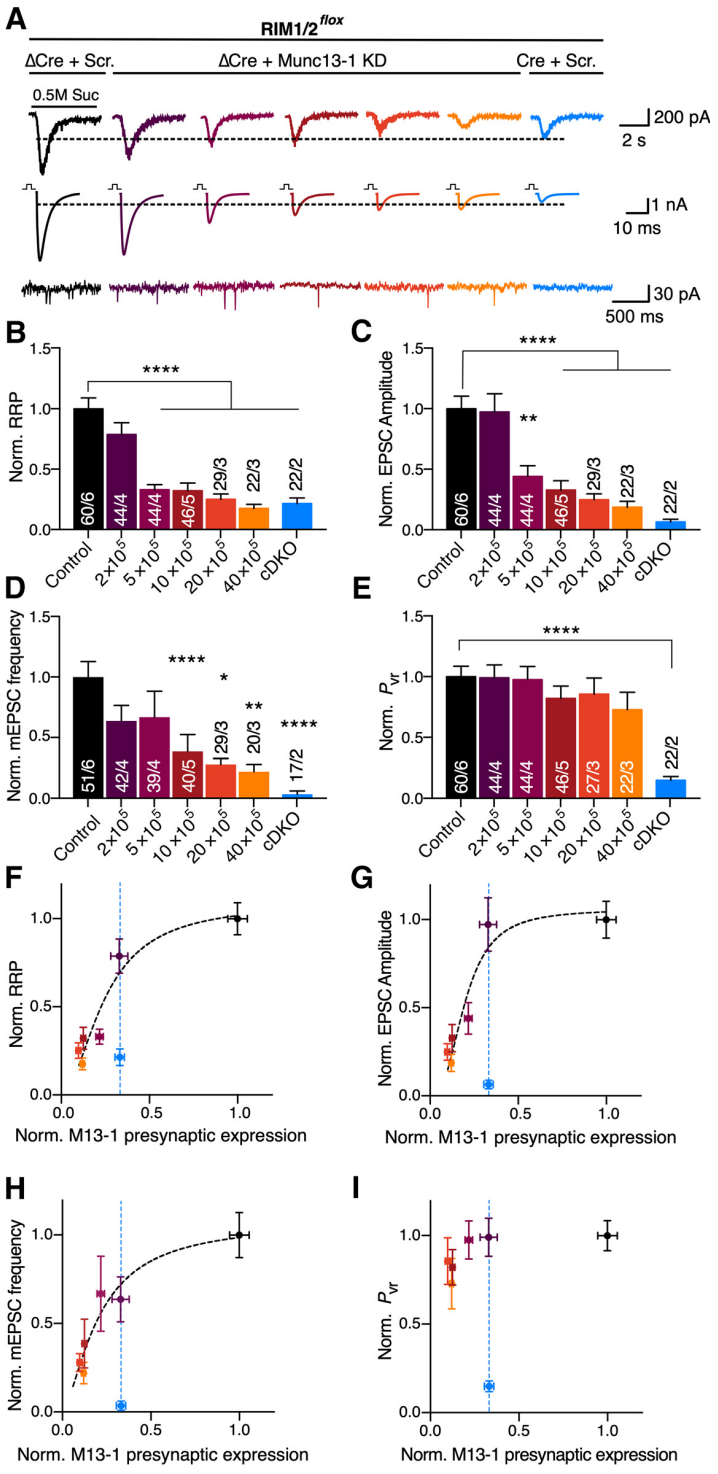

Figure 5. Quantification of RIM-dependent loss of Munc13-1 activity on synaptic properties. ***A***, Sample traces of current induced by hypertonic sucrose to estimate the RRP size (top), sample traces of EPSCs (middle), and mEPSCs (bottom). Autaptic hippocampal neurons were infected with ΔCre + Scramble (Scr.) shRNA as control, ΔCre + Munc13-1 KD shRNAs (2-40 × 10^5 IU) to produce Munc13-1 dose gradients, and Cre recombinase + Scramble shRNA to create RIM1/2 cDKO. Dashed lines indicate the maximum current amplitude of RIM1/2 cDKO. ***B–E***, Bar plots represent the normalized mean RRP defined as a charge measured by hypertonic sucrose application (***B***), normalized EPSC amplitude (***C***), normalized mEPSC frequency (***D***), and normalized P_{vr} (***E***). ***F–I***, Plots represent the normalized RRP size (***F***), EPSC amplitude (***G***), mEPSC frequency (***H***), and P_{vr} (***I***) as a function of normalized Munc13-1/VGLUT1 presynaptic expression. ***F-I***, Black dashed lines indicate fitting with the Hill equation. Blue dashed line indicates Munc13-1/VGLUT1 expression in RIM1/2 cDKO neurons. Data indicate normalized mean ± SEM. *$p \leq 0.05$; **$p \leq 0.01$; ****$p \leq 0.0001$; nonparametric one-way ANOVA with Kruskal–Wallis test followed by Dunn's *post hoc* test. For the absolute values and statistical overview, see also the table in Extended Data Figure 5-1.

Ca^{2+}-evoked release, and mEPSC frequency are achieved at 25%, 19%, and 20% of WT Munc13-1 level, respectively (Fig. 5*F–H*). These processes follow positive cooperativity functions (1.9 for SV priming, 2.6 for Ca^{2+}-evoked release, and 1.6 for mEPSC frequency). The similar sensitivity of Munc13-1 levels on the SV priming and mEPSC frequency functions suggests that the RRP is likely the source of vesicles released during spontaneous miniature events. These data also suggest that, at concentrations <30% of WT levels, Munc13-1 is a rate-limiting factor for priming and release.

Additionally, we observed that the impairment in physiological measurements in RIM1/2 cDKO synapses (which express ~30% of Munc13-1; Fig. 5*F–I*) did not follow the dose–response curves generated by Munc13-1 KD. This indicates that RIM1/2 cDKO loss of function does not only depend on Munc13-1 concentrations.

RIM1/2 controls P_{vr} independent from Munc13-1 but regulates SV docking and priming together with Munc13-1

To further assess the role of RIM independent of Munc13-1 function, we treated RIM1/2 control or deficient neurons with the highest dose Munc13-1 shRNA (40 × 10^5 IU). Near-complete removal of Munc13-1 in RIM1/2 cDKO neurons did not further reduce priming process and mEPSC frequency beyond the level of RIM1/2 cDKO alone (Fig. 6*B*; RIM1/2 Cre + Scramble: 0.12 ± 0.03 nC, $n = 61/5$; RIM1/2 Cre + Munc13-1 KD: 0.05 ± 0.008 nC, $n = 54/5$, $p = 0.057$; Fig. 6*F*; RIM1/2 Cre + Scramble: 0.50 ± 0.12 Hz, $n = 64/5$; RIM1/2 Cre + Munc13-1 KD: 0.50 ± 0.34 Hz, $n = 56/5$, $p > 0.999$, Kruskal–Wallis test), and showed a significant decrease compared with Munc13-1 KD in control neurons (Fig. 6*B*; RIM1/2 ΔCre + Munc13-1 KD: 0.08 ± 0.009 nC, $n = 50/5$; RIM1/2 Cre + Munc13-1 KD: 0.05 ± 0.008 nC, $n = 54/5$, $p = 0.015$; Fig. 6*F*; RIM1/2 ΔCre + Munc13-1 KD: 1.07 ± 0.22 Hz, $n = 55/5$; RIM1/2 Cre + Munc13-1 KD: 0.50 ± 0.34 Hz, $n = 56/5$, $p = 0.026$, Kruskal–Wallis test). These data provide supporting evidence for a function of RIM as an activator of Munc13-1 in SV priming (Deng et al., 2011; Camacho et al., 2017), and suggest that both RIM and Munc13-1 are required for priming function. Moreover, removal of Munc13-1 in the RIM1/2-deficient neurons did not further

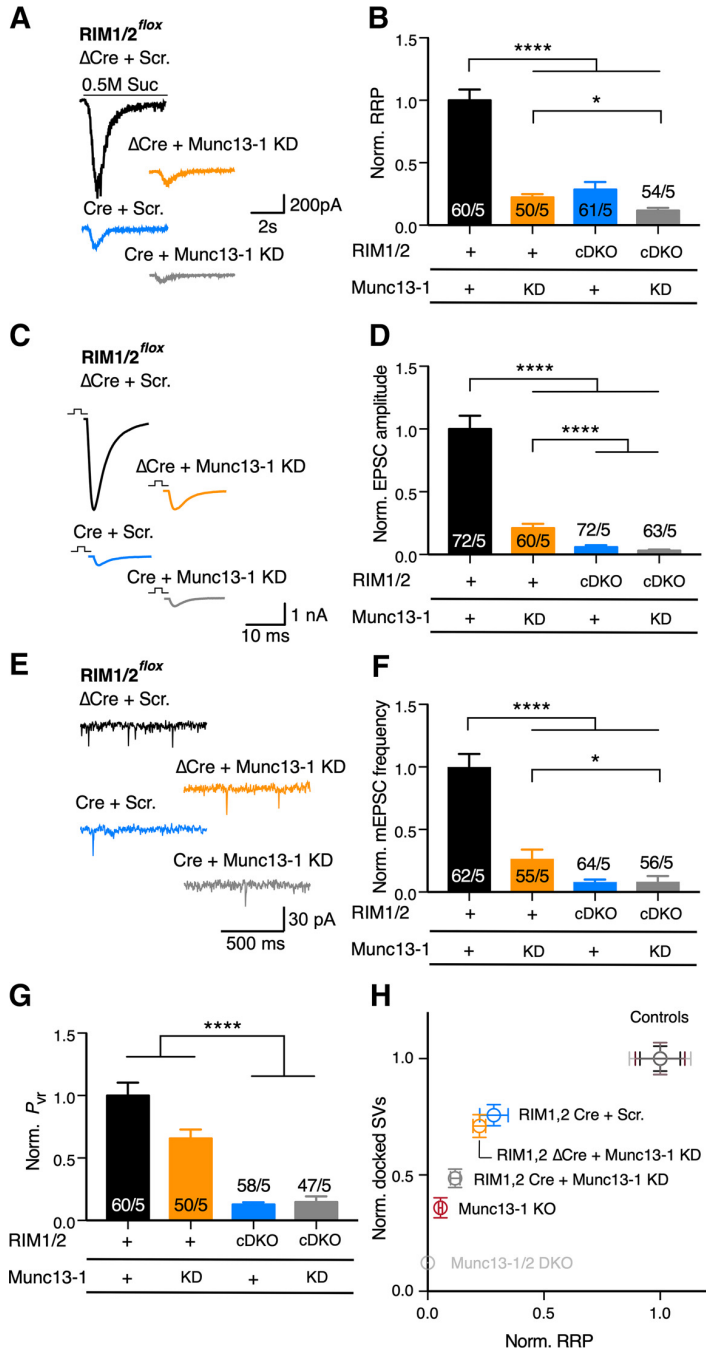

Figure 6. RIM-independent function of Munc13-1 on synaptic properties. ***A***, Sample traces represent the current evoked by hypertonic sucrose as an estimate for RRP in RIM1/2^{flox} cultures infected with ΔCre + Scramble (Scr.) shRNA (black), ΔCre + 40 × 10^5 IU of Munc13-1 KD shRNA (orange), Cre + Scramble shRNA (blue), and Cre + 40 × 10^5 Munc13-1 shRNA (gray). ***B***, Bar plot represents the normalized mean of charge released by hypertonic sucrose (referred to as RRP). ***C***, ***D***, Sample traces of EPSC (***C***) and bar plot of normalized EPSC amplitude. ***E***, ***F***, Sample traces of spontaneous release events (***E***), and the bar plot represents the normalized mean mEPSC frequency (***F***). ***G***, Bar plot represents the normalized P_{vr}. Normalization in all of the bar plots is performed relative to the corresponding control (ΔCre + scramble; black). In graph labels, "+" refers to the endogenous expression. "KD" refers to the Munc13-1 KD. "cDKO" refers to RIM1/2 deficiency. Numbers in bars indicate the cell number/culture number. Data indicate normalized mean ± SEM. *$p \leq 0.05$; ****$p \leq 0.0001$; nonparametric one-way ANOVA with Kruskal–Wallis test followed by Dunn's *post hoc* test. For the absolute values and statistical overview, see also the table in Extended Data Figure 6-1. ***H***, Plot represents the SV docking/priming relationship. Munc13-1/2 DKO data are adapted from Camacho et al. (2017). Controls represent ΔCre + Scr., Munc13-1 WT, and Munc13-1/2 DKO rescue with WT Munc13-1 (Camacho et al., 2017).

impair the EPSC amplitude (Fig. 6*D*; RIM1/2 Cre + Scramble: 0.23 ± 0.06 nA, $n = 72/5$; RIM1/2 Cre + Munc13-1 KD: 0.13 ± 0.04 nA, $n = 63/5$, $p = 0.745$, Kruskal–Wallis test) and P_{vr} (Fig. 6*G*; RIM1/2 Cre + Scramble: 0.8 ± 0.11%, $n = 58/5$; RIM1/2 Cre + Munc13-1 KD: 0.95 ± 0.29%, $n = 47/5$, $p > 0.999$, Kruskal–Wallis test), again emphasizing that RIM predominantly controls the Ca^{2+}-triggered release and P_{vr}.

Recent studies correlated SV docking to the priming process, where the loss of SV docking was accompanied by loss of SV priming (Siksou et al., 2009; Imig et al., 2014). As our molecular and genetic manipulations of RIM1/2 and Munc13-1 protein levels provided a range of SV docking and priming impairments, we used these data to obtain the levels of SV priming as a function of the SV docking activity. When plotting these two functions (Fig. 6*H*), we found that Munc13- and RIM-dependent docking and priming function did not show a linear correlation. Indeed, vesicle priming was more sensitive to protein levels than SV docking in all RIM and Munc13 KOs/KDs. This may indicate either a lower stoichiometry of RIM and Munc13 for SV docking than priming, or that the 2D ultrastructural image analysis has lower resolution for detecting an SV docking deficit. Furthermore, the effect on SV docking/priming observed in the absence of RIM illustrated a sensitivity defined by the reduction of Munc13-1 protein levels. This supports the notion that the role of RIM1/2 in SV docking and priming can be simply explained by its role in recruiting and activating Munc13-1, as previously proposed (Andrews-Zwilling et al., 2006; Deng et al., 2011; Camacho et al., 2017).

RIM1/2 does not contribute to activity-dependent RRP augmentation

Our ultrastructural results suggested that RIM recruits SVs to the proximity of AZ membrane (Fig. 2); therefore, we investigated whether this function of RIM supplies SVs to the activity-dependent RRP augmentation that occurs in the absence of Munc13-1 (Rosenmund et al., 2002). To do so, we probed the RRP size by hypertonic sucrose application before and 2 s after 50 APs at 10 Hz high-frequency stimulation (Rosenmund et al., 2002) (Fig. 7*A*). Munc13-1 KD in either control or RIM1/2 cDKO synapse exhibited an activity-dependent augmentation of RRP size (RRP ratio: Fig. 7*B*; RIM1/2 ΔCre + Scramble: 0.89 ± 0.03, $n = 31/4$; RIM1/2 ΔCre + Munc13-1 KD: 1.33 ± 0.08,

$n = 28/4$, $p < 0.0001$; RIM1/2 Cre + Munc13-1 KD: 1.45 ± 0.11, $n = 23/4$, $p < 0.0001$, Kruskal–Wallis test). This suggests that activity-dependent RRP augmentation occurs in the absence of RIM1/2, only when Munc13-1 levels are extremely low or completely abolished. Consistent with this, elimination of RIM1/2 alone, a condition in which Munc13-1 levels are reduced but not absent, did not result in high-frequency stimulation-mediated RRP augmentation (Fig. 7*B*; RIM1/2 ΔCre + Scramble: 0.89 ± 0.03, $n = 31/4$; RIM1/2 Cre + Scramble: 1.07 ± 0.08, $n = 29/4$, $p = 0.854$, Kruskal–Wallis test). Hence, RRP augmentation requires the absence of Munc13-1 but does not rely on the proximal localization of SVs to the AZ membrane by RIM1/2.

Which molecule underlies activity-dependent RRP size augmentation in the absence of Munc13-1? In hippocampal neurons, Munc13-2 is expressed at low, but detectable, levels and is responsible for the remaining synaptic transmission in Munc13-1-deficient glutamatergic neurons (Rosenmund et al., 2002). The brain-specific isoform of Munc13-2 (bMunc13-2), in particular, has been postulated to participate in augmentation (Lipstein et al., 2012). To examine whether Munc13-2 is indeed responsible for RRP augmentation, we used Munc13-2-deficient neurons (Munc13-2 KO) and reduced Munc13-1 expression levels by shRNA-mediated KD (40×10^5 IU) and examined activity-dependent RRP augmentation (Fig. 7*C*,*D*). We found that even with Munc13-1 KD, which revealed high-frequency stimulation-dependent RRP augmentation in control and RIM1/2 cDKO neurons, no RRP augmentation was observed in the absence of Munc13-2 (Fig. 7*D*; Scramble: 0.88 ± 0.06, $n = 25/2$; Munc13-1 KD: 0.99 ± 0.11, $n = 15/2$, $p = 0.7$, Mann–Whitney test). These data demonstrate that (1) Munc13-2 does indeed mediate RRP augmentation, (2) the absence of Munc13-1 is necessary to unmask RRP augmentation, and (3) RIM1/2 is not necessary for Munc13-2's priming activity or contribution to RRP augmentation.

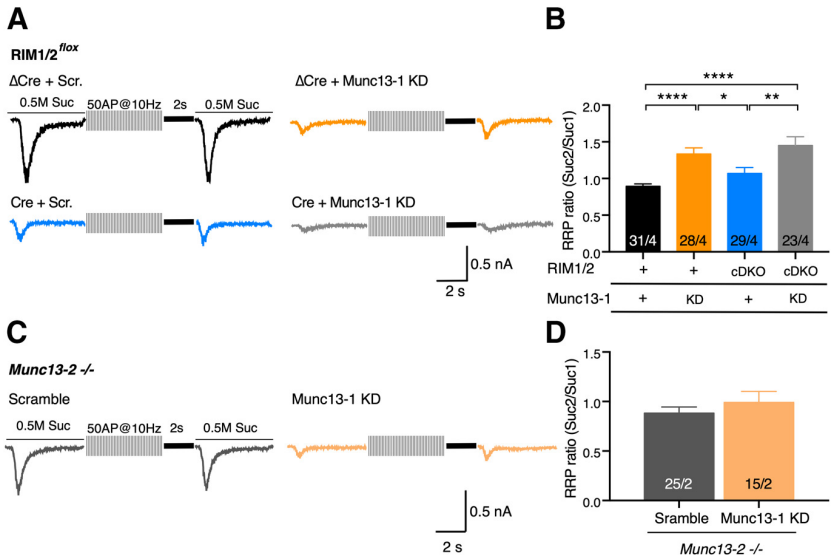

Figure 7. The regulation of RRP augmentation in the absence of RIM and Munc13-1. ***A***, Sample traces represent RRP augmentation protocol in RIM1/2^{flox} cultures infected with ΔCre + Scramble (Scr.) shRNA (black), ΔCre + 40×10^5 IU Munc13-1 KD shRNA (orange), Cre + Scramble shRNA (blue), and Cre + 40×10^5 Munc13-1 shRNA (gray). After initial sucrose-evoked charge measurement (Suc1), 50 APs at 10 Hz were applied followed by another sucrose-evoked charge measurement 2 s after (Suc2). ***B***, Bar plot represents the mean RRP augmentation (ratio of Suc2 to Suc1) in neurons described in ***A***. Graph labels indicate endogenous expression "+." "KD" refers to the Munc13-1 KD. "cDKO" refers to RIM1/2-deficient neurons; nonparametric one-way ANOVA with Kruskal–Wallis test followed by Dunn's *post hoc* test. ***C***, Sample traces of RRP augmentation protocol applied on Munc13-2 KO neurons with Munc13-1 KD (40×10^5 shRNA IU). ***D***, Bar plot represents the measurement of RRP augmentations (Suc2/Suc1) in neurons as described in ***C***. The nonparametric *t* test, followed by Mann–Whitney test, did not show differences between Munc13-2 KO with Scramble and Munc13-1 KD. Numbers in bar plots indicate the cell number/culture number. Data indicate mean ± SEM. $*p \leq 0.05$; $**p \leq 0.01$; $****p \leq 0.0001$. For the statistical overview, see also the table in Extended Data Figure 7-1.

Discussion

Many proteins in the AZ work in concert to efficiently transduce presynaptic APs into neurotransmitter release. To understand how the AZ mediates presynaptic function, it is crucial to consider individual proteins in conjunction with their interaction partners. Here, we explored the extent to which RIM individually plays direct roles in SV localization and neurotransmission, versus its secondary roles through interactions with Munc13-1. We find that loss of RIM1/2 causes two effects on ultrastructure: impaired AZ-proximal localization of SVs and reduced SV docking. The docking deficit, in the absence of RIM, likely stems from a lack of activation and stabilization of Munc13-1. However, reduction of AZ-proximal SVs, which did not occur in Munc13-1 KO, reflects RIM's independent role in SV localization. Similar to the RIM's docking function, electrophysiological analysis showed that priming function of RIM depends on Munc13-1. However, the role of RIM in SV localization does not affect activity-dependent RRP augmentation. This work provides a finer view of the extent to which RIM and Munc13 cooperate to achieve SV recruitment, docking, priming and fusion.

Role of RIM and Munc13-1 in SV localization

Recent advances in cryofixation techniques of neuronal tissue have emphasized the connection between synaptic ultrastructure and function, such as revealing the morphologic equivalent of SV priming as SV docking using high-pressure freezing fixation (Siksou et al., 2009; Imig et al., 2014). Therefore, we examined SV docking and distribution in high-pressure frozen synapses of RIM and/or Munc13-1-deficient synapses and achieved two important findings:

First, we show that RIM influences vesicle docking, which is consistent with the previous reports in murine synapses (Han et al., 2011; Kaeser et al., 2011; S. S. Wang et al., 2016) and in *Caenorhabditis elegans* (Gracheva et al., 2008). Nevertheless, the effect of RIM on SV docking is only attributable to Munc13-1 activation. This largely confirms the dogma of RIM acting upstream of Munc13-1 in SV docking (Han et al., 2011; Camacho et al., 2017).

Second, we find that RIM influences the distribution of SVs near the plasma membrane. This is different from Munc13-1 KO (Fig. 1) and Munc13-1/2-deficient synapses (Siksou et al., 2009; Imig et al., 2014), which demonstrated an enriched density of SVs near to the plasma membrane, but revealed severe docking deficits. The accumulation of SVs at AZ-proximal regions, which

disappears with loss of RIM, demonstrates that the AZ-proximal SV localization relies on RIM, independent of Munc13-1. This finding extends the observations from cryo-electron tomographic studies in synaptosomes, where SVs connected with short protein "tethers" to the AZ membrane depend partially on RIM1α (Fernández-Busnadiego et al., 2010, 2013). We believe that these findings are not affected by synapse size, as previous studies reported that RIM1/2 cDKO does not impair total SV number, PSD length, or bouton size (Kaeser et al., 2011; Acuna et al., 2016) and Munc13-1/2 DKO does not affect SV number per terminal and PSD length (Imig et al., 2014). In neuromuscular junction synapses of *C. elegans*, RIM homolog, Unc10, deficiency also impairs SV localization to the dense projections (Weimer et al., 2006), suggesting an evolutionarily conserved role for RIM in SV localization. While SV localization near the AZ membrane is mediated by RIM, other AZ proteins, such as Piccolo, Bassoon, Liprin-α3, and Liprin-α2, influence the long-range SV distribution by modulating early stages of AZ assembly and vesicle formation (Mukherjee et al., 2010; Spangler et al., 2013; Wong et al., 2018; Ackermann et al., 2019). Thus, AZ proteins act in a hierarchical order by determining the precise SV localization.

What is the physiological relevance of vesicle tethering? One hypothesis is that tethering brings SVs in close proximity to the plasma membrane to make SVs readily available for entrance into the RRP (Hallermann and Silver, 2013). However, when we examined activity-dependent changes in RRP size, a condition that shows RRP augmentation in Munc13-1-deficient synapses (Rosenmund et al., 2002), we find that RIM does not affect this phenomenon. This argues that the physiological role of RIM in tethering function manifests by different means. Essentially, the function of tethers depends on their molecular composition and interactions with scaffolds. Bassoon, a protein that modulates long-range vesicle localization, tethers SVs by reloading SVs into the pool (Hallermann et al., 2010). Nevertheless, the fact that RIM-Rab3 complex anchors SVs close to both Ca^{2+} channels and plasma membrane (Han et al., 2011; Kaeser et al., 2011; de Jong et al., 2018) may indicate that RIM's tethering function is a product of several molecular interactions. Therefore, the functional role of RIM in SV localization may be resolved by other electrophysiological measurements as well as by providing identity to the composition of tethers at the AZ.

Role of RIM and Munc13 isoforms in vesicular release probability

RIM defines the efficiency of release by recruiting Ca^{2+} channels (Han et al., 2011; Kaeser et al., 2011), binding to PIP2 rich membranes (de Jong et al., 2018) and interacting with Rab3 (Y. Wang et al., 1997; X. Wang et al., 2001; Fukuda, 2003; Schluter et al., 2006). In addition, in *C. elegans*, the interaction of Unc10 with Unc13 modulates P_{vr} (Zhou et al., 2013; Liu et al., 2019). However, we show that, in mammals, the effect of RIM on P_{vr} is independent from Munc13-1. Then what causes loss of P_{vr} in Munc13-1 KO neurons? While previous work has demonstrated that Munc13 KD impairs Ca^{2+} entry in hippocampal mass culture (Calloway et al., 2015), recent work in Munc13-1/2 DKO autaptic neurons shows no effect on presynaptic Ca^{2+} signal (Brockmann et al., 2020). As our data show that Munc13-1 reduction does not have a major effect on vesicular release probability, our findings are consistent with a lack of Munc13-1 effect on Ca^{2+} influx. Since only the total absence of Munc13-1, but not varying Munc13-1 levels, impairs P_{vr}, we presume that priming with the alternative Munc13 isoform, Munc13-2, results in low release efficiency SVs. The function of Munc13-2 is only unmasked in the complete absence of Munc13-1, and not even revealed in the case of drastically reduced Munc13-1 expression levels. Furthermore, while only Munc13-2 is responsible for activity-dependent augmentation of RRP in a RIM- and Munc13-1-independent manner, both Munc13-1 and Munc13-2 contribute to dynamic changes in release probability through short-term plasticity by lowering the energy barrier for vesicle fusion (Rosenmund et al., 2002; Basu et al., 2007). Molecularly, these functions take place by activation of regulatory domains that bind to CaM, DAG (via C1 domain), and Ca^{2+} (via C2B domain) (Rhee et al., 2002; Junge et al., 2004; Shin et al., 2010; Lipstein et al., 2013).

Other pathways of docking/priming parallel to RIM-Munc13-1

While the relevance of RIM-Munc13-1 interactions in SV docking and release at small central synapse is clear, alternative paths exist that allow SVs to become fusion-competent. For example, bMunc13-2 or Munc13-3 does not require RIM and is differentially expressed in specific brain regions (Augustin et al., 1999b). Our ultrastructural and physiological data from Munc13-1 KD in RIM1/2 cDKO neurons, as well as Munc13-1 KO neurons, suggest that bMunc13-2, which does not require activation via RIM, accounts for ~30% of docking and ~5% of priming. Moreover, in invertebrate synapses, long and short Munc13s exist that form distinct complexes with AZ proteins and regulate different forms of release similar to Munc13-1, -2, and -3 (Brose et al., 1995; Aravamudan et al., 1999; Richmond et al., 1999; Kohn et al., 2000; Rosenmund et al., 2002; Bohme et al., 2016; Liu et al., 2019). An interesting observation from our study is that RIM1/2 cDKO shows more severe impact on SV priming in glutamatergic autaptic neurons compared with GABAergic synapses in hippocampal mass culture (Deng et al., 2011). Although these differences could be attributed to the experimental systems, it is known that GABAergic neurons, in contrast to glutamatergic neurons, redundantly use Munc13-2 for priming (Augustin et al., 1999a; Varoqueaux et al., 2002). The synapse-type-specific AZ protein composition is also evident in other vertebrate synapses. For example, in hippocampus mossy fiber synapses, RIM expression is low, and Munc13-1 uses RIM-BP to prime SVs (Brockmann et al., 2019). Overall, it is noteworthy that some synapses are prone to use more than one mode of priming.

Understanding how different synapses encode the incoming AP pattern into release requires studying the unique transduction apparatus expressed in individual synapses. We must dissect not only the individual role of molecules in the synapse but also how these molecules work together. For instance, our experiment examining the Munc13-1 concentration dependency of priming extends the previous studies (Deng et al., 2011) by showing that RIM boosts the Munc13-1 priming function by approximately fourfold. Therefore, we require more sophisticated models than single protein, loss-of-function experiments. In this study, we aimed to investigate how synapses respond to the relative changes in expression of AZ components by modifying the protein expression levels and studying the isoform-specific functions. We provide the first step in characterizing the role of RIM and Munc13 in small synapses to facilitate the understanding of complex molecular functions at the AZ.

References

Ackermann F, Waites CL, Garner CC (2015) Presynaptic active zones in invertebrates and vertebrates. EMBO Rep 16:923–938.

Ackermann F, Schink KO, Bruns C, Izsvak Z, Hamra FK, Rosenmund C, Garner CC (2019) Critical role for Piccolo in synaptic vesicle retrieval. Elife 8:e46629.

Acuna C, Liu X, Sudhof TC (2016) How to make an active zone: unexpected universal functional redundancy between RIMs and RIM-BPs. Neuron 91:792–807.

Andrews-Zwilling YS, Kawabe H, Reim K, Varoqueaux F, Brose N (2006) Binding to Rab3A-interacting molecule RIM regulates the presynaptic recruitment of Munc13-1 and ubMunc13-2. J Biol Chem 281:19720–19731.

Arancillo M, Min SW, Gerber S, Münster-Wandowski A, Wu YJ, Herman M, Trimbuch T, Rah JC, Ahnert-Hilger G, Riedel D, Südhof TC, Rosenmund C (2013) Titration of Syntaxin1 in mammalian synapses reveals multiple roles in vesicle docking, priming, and release probability. J Neurosci 33:16698–16714.

Aravamudan B, Fergestad T, Davis WS, Rodesch CK, Broadie K (1999) *Drosophila* UNC-13 is essential for synaptic transmission. Nat Neurosci 2:965–971.

Augustin I, Rosenmund C, Sudhof TC, Brose N (1999a) Munc13-1 is essential for fusion competence of glutamatergic synaptic vesicles. Nature 400:457–461.

Augustin I, Betz A, Herrmann C, Jo T, Brose N (1999b) Differential expression of two novel Munc13 proteins in rat brain. Biochem J 337:363–371.

Basu J, Betz A, Brose N, Rosenmund C (2007) Munc13-1 C1 domain activation lowers the energy barrier for synaptic vesicle fusion. J Neurosci 27:1200–1210.

Betz A, Thakur P, Junge HJ, Ashery U, Rhee JS, Scheuss V, Rosenmund C, Rettig J, Brose N (2001) Functional interaction of the active zone proteins Munc13-1 and RIM1 in synaptic vesicle priming. Neuron 30:183–196.

Bohme MA, McCarthy AW, Grasskamp AT, Beuschel CB, Goel P, Jusyte M, Laber D, Huang S, Rey U, Petzoldt AG, Lehmann M, Gottfert F, Haghighi P, Hell SW, Owald D, Dickman D, Sigrist SJ, Walter AM (2019) Rapid active zone remodeling consolidates presynaptic potentiation. Nat Commun 10:1085.

Bohme MA, Beis C, Reddy-Alla S, Reynolds E, Mampell MM, Grasskamp AT, Lutzkendorf J, Bergeron DD, Driller JH, Babikir H, Gottfert F, Robinson IM, O'Kane CJ, Hell SW, Wahl MC, Stelzl U, Loll B, Walter AM, Sigrist SJ (2016) Active zone scaffolds differentially accumulate Unc13 isoforms to tune Ca(2+) channel-vesicle coupling. Nat Neurosci 19:1311–1320.

Brockmann MM, Maglione M, Willmes CG, Stumpf A, Bouazza BA, Velasquez LM, Grauel MK, Beed P, Lehmann M, Gimber N, Schmoranzer J, Sigrist SJ, Rosenmund C, Schmitz D (2019) RIM-BP2 primes synaptic vesicles via recruitment of Munc13-1 at hippocampal mossy fiber synapses. Elife 8:e43243.

Brockmann MM, Zarebidaki F, Camacho M, Grauel MK, Trimbuch T, Sudhof TC, Rosenmund C (2020) A trio of active zone proteins comprised of RIM-BPs, RIMs, and Munc13s governs neurotransmitter release. Cell Rep 32:107960.

Brose N, Hofmann K, Hata Y, Sudhof TC (1995) Mammalian homologues of *Caenorhabditis elegans* unc-13 gene define novel family of C2-domain proteins. J Biol Chem 270:25273–25280.

Calloway N, Gouzer G, Xue M, Ryan TA (2015) The active-zone protein Munc13 controls the use-dependence of presynaptic voltage-gated calcium channels. Elife 4:e07728.

Camacho M, Basu J, Trimbuch T, Chang S, Pulido-Lozano C, Chang SS, Duluvova I, Abo-Rady M, Rizo J, Rosenmund C (2017) Heterodimerization of Munc13 C2A domain with RIM regulates synaptic vesicle docking and priming. Nat Commun 8:15293.

de Jong AP, Roggero CM, Ho MR, Wong MY, Brautigam CA, Rizo J, Kaeser PS (2018) RIM C2B domains target presynaptic active zone functions to PIP2-containing membranes. Neuron 98:335–349.e337.

Deng L, Kaeser PS, Xu W, Sudhof TC (2011) RIM proteins activate vesicle priming by reversing autoinhibitory homodimerization of Munc13. Neuron 69:317–331.

Dulubova I, Lou X, Lu J, Huryeva I, Alam A, Schneggenburger R, Sudhof TC, Rizo J (2005) A Munc13/RIM/Rab3 tripartite complex: from priming to plasticity? EMBO J 24:2839–2850.

Fernández-Busnadiego R, Zuber B, Maurer UE, Cyrklaff M, Baumeister W, Lucic V (2010) Quantitative analysis of the native presynaptic cytomatrix by cryoelectron tomography. J Cell Biol 188:145–156.

Fernández-Busnadiego R, Asano S, Oprisoreanu AM, Sakata E, Doengi M, Kochovski Z, Zürner M, Stein V, Schoch S, Baumeister W, Lucić V (2013) Cryo-electron tomography reveals a critical role of RIM1alpha in synaptic vesicle tethering. J Cell Biol 201:725–740.

Fukuda M (2003) Distinct Rab binding specificity of Rim1, Rim2, rabphilin, and Noc2: identification of a critical determinant of Rab3A/Rab27A recognition by Rim2. J Biol Chem 278:15373–15380.

Gracheva EO, Hadwiger G, Nonet ML, Richmond JE (2008) Direct interactions between *C. elegans* RAB-3 and Rim provide a mechanism to target vesicles to the presynaptic density. Neurosci Lett 444:137–142.

Graf ER, Valakh V, Wright CM, Wu C, Liu Z, Zhang YQ, DiAntonio A (2012) RIM promotes calcium channel accumulation at active zones of the *Drosophila* neuromuscular junction. J Neurosci 32:16586–16596.

Gundelfinger ED, Kessels MM, Qualmann B (2003) Temporal and spatial coordination of exocytosis and endocytosis. Nat Rev Mol Cell Biol 4:127–139.

Hallermann S, Silver RA (2013) Sustaining rapid vesicular release at active zones: potential roles for vesicle tethering. Trends Neurosci 36:185–194.

Hallermann S, Fejtova A, Schmidt H, Weyhersmuller A, Silver RA, Gundelfinger ED, Eilers J (2010) Bassoon speeds vesicle reloading at a central excitatory synapse. Neuron 68:710–723.

Han Y, Kaeser PS, Sudhof TC, Schneggenburger R (2011) RIM determines Ca(2)+ channel density and vesicle docking at the presynaptic active zone. Neuron 69:304–316.

Han Y, Babai N, Kaeser P, Sudhof TC, Schneggenburger R (2015) RIM1 and RIM2 redundantly determine Ca^{2+} channel density and readily releasable pool size at a large hindbrain synapse. J Neurophysiol 113:255–263.

Hibino H, Pironkova R, Onwumere O, Vologodskaia M, Hudspeth AJ, Lesage F (2002) RIM binding proteins (RBPs) couple Rab3-interacting molecules (RIMs) to voltage-gated Ca(2+) channels. Neuron 34:411–423.

Hirano M, Takada Y, Wong CF, Yamaguchi K, Kotani H, Kurokawa T, Mori MX, Snutch TP, Ronjat M, De Waard M, Mori Y (2017) C-terminal splice variants of P/Q-type Ca(2+) channel CaV2.1 alpha1 subunits are differentially regulated by Rab3-interacting molecule proteins. J Biol Chem 292:9365–9381.

Imig C, Min SW, Krinner S, Arancillo M, Rosenmund C, Sudhof TC, Rhee J, Brose N, Cooper BH (2014) The morphological and molecular nature of synaptic vesicle priming at presynaptic active zones. Neuron 84:416–431.

Junge HJ, Rhee JS, Jahn O, Varoqueaux F, Spiess J, Waxham MN, Rosenmund C, Brose N (2004) Calmodulin and Munc13 form a Ca^{2+} sensor/effector complex that controls short-term synaptic plasticity. Cell 118:389–401.

Kaeser PS, Kwon HB, Chiu CQ, Deng L, Castillo PE, Sudhof TC (2008) RIM1alpha and RIM1beta are synthesized from distinct promoters of the RIM1 gene to mediate differential but overlapping synaptic functions. J Neurosci 28:13435–13447.

Kaeser PS, Deng L, Wang Y, Dulubova I, Liu X, Rizo J, Sudhof TC (2011) RIM proteins tether Ca^{2+} channels to presynaptic active zones via a direct PDZ-domain interaction. Cell 144:282–295.

Kaeser PS, Deng L, Fan M, Sudhof TC (2012) RIM genes differentially contribute to organizing presynaptic release sites. Proc Natl Acad Sci USA 109:11830–11835.

Kiyonaka S, Wakamori M, Miki T, Uriu Y, Nonaka M, Bito H, Beedle AM, Mori E, Hara Y, De Waard M, Kanagawa M, Itakura M, Takahashi M, Campbell KP, Mori Y (2007) RIM1 confers sustained activity and neurotransmitter vesicle anchoring to presynaptic Ca^{2+} channels. Nat Neurosci 10:691–701.

Kohn RE, Duerr JS, McManus JR, Duke A, Rakow TL, Maruyama H, Moulder G, Maruyama IN, Barstead RJ, Rand JB (2000) Expression of multiple UNC-13 proteins in the *Caenorhabditis elegans* nervous system. Mol Biol Cell 11:3441–3452.

Lipstein N, Schaks S, Dimova K, Kalkhof S, Ihling C, Kolbel K, Ashery U, Rhee J, Brose N, Sinz A, Jahn O (2012) Nonconserved Ca(2+)/calmodulin binding sites in Munc13s differentially control synaptic short-term plasticity. Mol Cell Biol 32:4628–4641.

Lipstein N, Sakaba T, Cooper BH, Lin KH, Strenzke N, Ashery U, Rhee JS, Taschenberger H, Neher E, Brose N (2013) Dynamic control of synaptic vesicle replenishment and short-term plasticity by Ca(2+)-calmodulin-Munc13-1 signaling. Neuron 79:82–96.

Liu H, Li L, Nedelcu D, Hall Q, Zhou L, Wang W, Yu Y, Kaplan JM, Hu Z (2019) Heterodimerization of UNC-13/RIM regulates synaptic vesicle release probability but not priming in *C. elegans*. Elife 8:e40585.

Mukherjee K, Yang X, Gerber SH, Kwon HB, Ho A, Castillo PE, Liu X, Sudhof TC (2010) Piccolo and bassoon maintain synaptic vesicle clustering without directly participating in vesicle exocytosis. Proc Natl Acad Sci USA 107:6504–6509.

Rhee JS, Betz A, Pyott S, Reim K, Varoqueaux F, Augustin I, Hesse D, Sudhof TC, Takahashi M, Rosenmund C, Brose N (2002) Beta phorbol ester- and diacylglycerol-induced augmentation of transmitter release is mediated by Munc13s and not by PKCs. Cell 108:121–133.

Richmond JE, Davis WS, Jorgensen EM (1999) UNC-13 is required for synaptic vesicle fusion in *C. elegans*. Nat Neurosci 2:959–964.

Rosenmund C, Stevens CF (1996) Definition of the readily releasable pool of vesicles at hippocampal synapses. Neuron 16:1197–1207.

Rosenmund C, Sigler A, Augustin I, Reim K, Brose N, Rhee JS (2002) Differential control of vesicle priming and short-term plasticity by Munc13 isoforms. Neuron 33:411–424.

Sakamoto H, Ariyoshi T, Kimpara N, Sugao K, Taiko I, Takikawa K, Asanuma D, Namiki S, Hirose K (2018) Synaptic weight set by Munc13-1 supramolecular assemblies. Nat Neurosci 21:41–49.

Schluter OM, Basu J, Sudhof TC, Rosenmund C (2006) Rab3 superprimes synaptic vesicles for release: implications for short-term synaptic plasticity. J Neurosci 26:1239–1246.

Schoch S, Gundelfinger ED (2006) Molecular organization of the presynaptic active zone. Cell Tissue Res 326:379–391.

Shin OH, Lu J, Rhee JS, Tomchick DR, Pang ZP, Wojcik SM, Camacho-Perez M, Brose N, Machius M, Rizo J, Rosenmund C, Südhof TC (2010) Munc13 C2B domain is an activity-dependent Ca^{2+} regulator of synaptic exocytosis. Nat Struct Mol Biol 17:280–288.

Siksou L, Varoqueaux F, Pascual O, Triller A, Brose N, Marty S (2009) A common molecular basis for membrane docking and functional priming of synaptic vesicles. Eur J Neurosci 30:49–56.

Spangler SA, Schmitz SK, Kevenaar JT, de Graaff E, de Wit H, Demmers J, Toonen RF, Hoogenraad CC (2013) Liprin-alpha 2 promotes the presynaptic recruitment and turnover of RIM1/CASK to facilitate synaptic transmission. J Cell Biol 201:915–928.

Sudhof TC (2012) The presynaptic active zone. Neuron 75:11–25.

Varoqueaux F, Sigler A, Rhee JS, Brose N, Enk C, Reim K, Rosenmund C (2002) Total arrest of spontaneous and evoked synaptic transmission but normal synaptogenesis in the absence of Munc13-mediated vesicle priming. Proc Natl Acad Sci USA 99:9037–9042.

Verhage M, Sorensen JB (2008) Vesicle docking in regulated exocytosis. Traffic 9:1414–1424.

Wang SS, Held RG, Wong MY, Liu C, Karakhanyan A, Kaeser PS (2016) Fusion competent synaptic vesicles persist upon active zone disruption and loss of vesicle docking. Neuron 91:777–791.

Wang X, Hu B, Zimmermann B, Kilimann MW (2001) Rim1 and rabphilin-3 bind Rab3-GTP by composite determinants partially related through N-terminal alpha -helix motifs. J Biol Chem 276:32480–32488.

Wang Y, Okamoto M, Schmitz F, Hofmann K, Sudhof TC (1997) Rim is a putative Rab3 effector in regulating synaptic-vesicle fusion. Nature 388:593–598.

Watanabe S, Rost BR, Camacho-Perez M, Davis MW, Sohl-Kielczynski B, Rosenmund C, Jorgensen EM (2013) Ultrafast endocytosis at mouse hippocampal synapses. Nature 504:242–247.

Weimer RM, Gracheva EO, Meyrignac O, Miller KG, Richmond JE, Bessereau JL (2006) UNC-13 and UNC-10/rim localize synaptic vesicles to specific membrane domains. J Neurosci 26:8040–8047.

Wong MY, Liu CL, Wang SS, Roquas AC, Fowler SC, Kaeser PS (2018) Liprin-alpha 3 controls vesicle docking and exocytosis at the active zone of hippocampal synapses. Proc Natl Acad Sci USA 115:2234–2239.

Wu X, Cai Q, Shen Z, Chen X, Zeng M, Du S, Zhang M (2019) RIM and RIM-BP form presynaptic active-zone-like condensates via phase separation. Mol Cell 73:971–984.e975.

Zhou K, Stawicki TM, Goncharov A, Jin Y (2013) Position of UNC-13 in the active zone regulates synaptic vesicle release probability and release kinetics. Elife 2:e01180.

Extended Data

Figure 1-1. Values and statistics corresponding to Figure 1.

Figure 1	RIM^{flox} + ΔCre	RIM^{flox} + Cre	*p*-value	Munc13-1 WT	Munc13-1 KO	*p*-value
n/N	n= 153/3	n = 161/3		n = 148/3	n = 173/3	
PSD length (nm)	281.8 ± 12.8	286.7 ± 8.95	0.0939	312.3 ± 10.72	333.4 ±12.03	0.3821
Docked SV	1.10 ± 0.09	0.73 ± 0.071	0.0019	1.57 ± 0.10	0.56 ± 0.07	<0.0001
Proximal SV	1.80 ± 0.12	1.28 ± 0.10	0.0004	2.03 ± 0.12	2.09 ± 0.13	0.8534
Distal SV	8.96 ± 0.35	8.60 ± 0.3	0.6746	9.61 ± 0.34	10.23 ± 0.38	0.6771
n = number of synapses; N= number of cultures, Values indicate mean ± SEM, Unpaired t test (Mann-Whitney test)						

Figure 1-2. Exemplary images corresponding to Figure 1. The figure shows raw micrographs (left) and the corresponding micrographs with marked vesicles (right). Vesicles are designated according to their distance to the AZ membrane: docked SVs (orange), proximal SVs (green), distal SVs (blue). Scale bar, 100 nm.

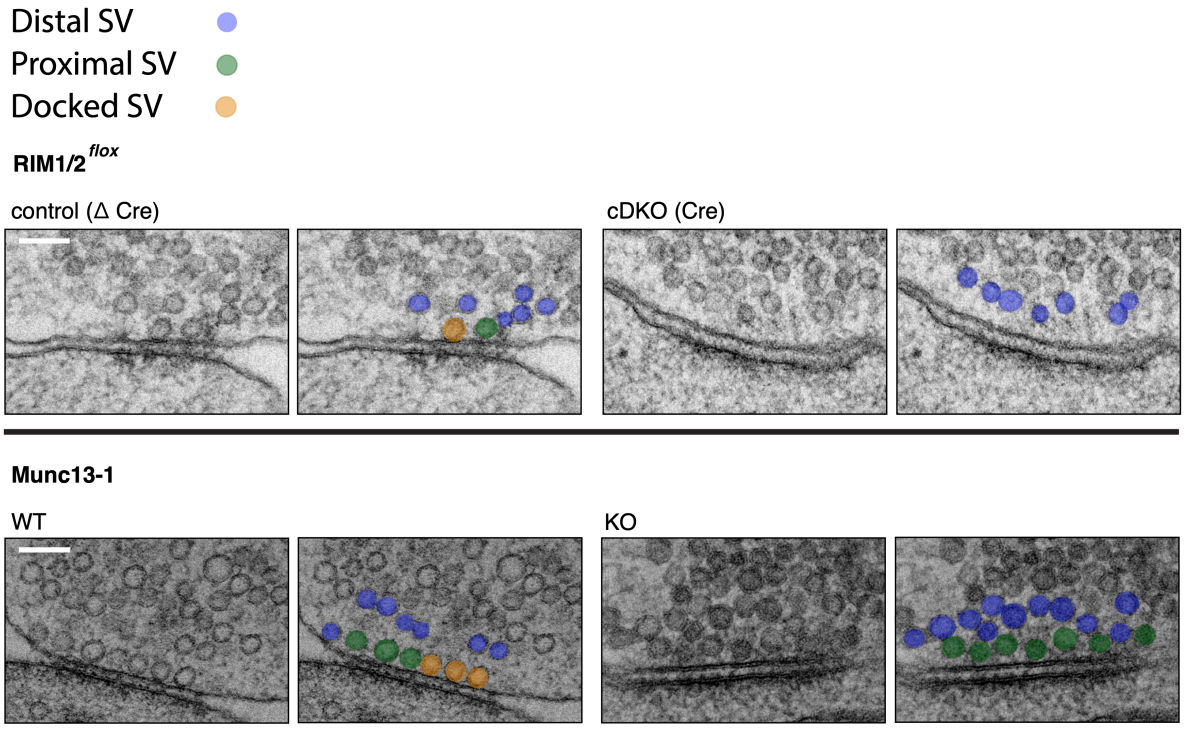

Figure 2-1. Values and statistics corresponding to Figure 2.

Figure 2A, B	ΔCre + Scr.	ΔCre + M13-1 KD	Cre + Scr.	Cre + M13-1 KD	Test statistics
n/N	3/3	3/3	3/3	3/3	
Norm. Munc13-1/Tubulin expression	1	0.02 ± 0.009	0.35 ± 0.08	0.01 ± 0.002	$F(3, 8) = 133.8$, $p < 0.0001$
Norm. RIM/Tubulin expression	1	0.70 ± 0.06	0.14 ± 0.09	0.11 ± 0.06	$F(3, 8) = 48.07$, $p < 0.0001$
n = number of repeats; N= number of cultures, Values indicate mean ± SEM, test: One way ANOVA					

Figure 2C-H	ΔCre + Scr.	ΔCre + M13-1 KD	Cre + Scr.	Cre + M13-1 KD	Test statistics
n/N	157/3	148/3	168/3	167/3	
Docked SVs	2.13 ± 0.11	1.42 ± 0.09	1.61 ± 0.1	0.95 ± 0.07	$H = 64.74$, $p < 0.0001$
Proximal SVs	2.53 ± 0.13	2.95 ± 0.18	1.95 ± 0.13	1.98 ± 0.14	$H = 30.05$, $p < 0.0001$
Distal SVs	12.69 ± 0.38	12.92 ± 0.45	12.45 ± 0.38	12.8 ± 0.36	$H = 1.928$, $p = 0.5874$
n = number of synapses; N= number of cultures, Values indicate mean ± SEM, H test: Kruskal-Wallis test					

Figure 2-2. Exemplary images corresponding to Figure 2. The figure shows raw micrographs (left) and the corresponding micrographs with marked vesicles (right). Vesicles are designated according to their distance to the AZ membrane: docked SVs (orange), proximal SVs (green), distal SVs (blue). Scale bar, 100 nm.

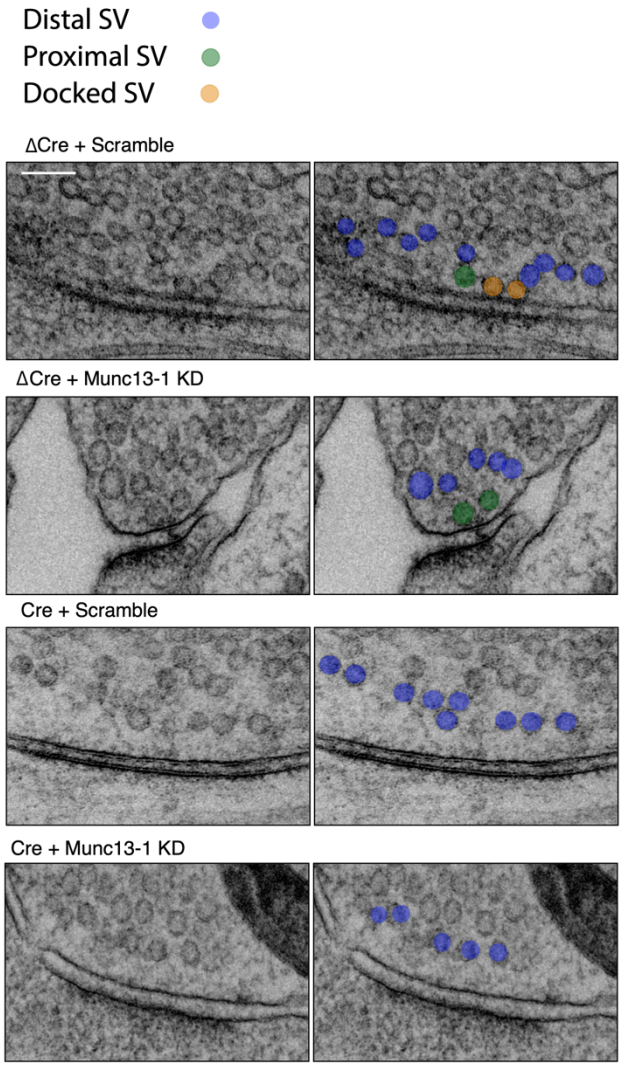

Figure 3-1. Absolute values and statistics corresponding to Figure 3.

Figure 3	RIM^{flox} + ΔCre	RIM^{flox} + Cre	*p*-value	M13-1 WT	M13-1 KO	*p*-value
n/N	41/5	51/5		27/3	35/3	
RRP (nC)	0.7 ± 0.1	0.08 ± 0.01	$p < 0.0001$	0.69 ± 0.09	0.04 ± 0.006	$p < 0.0001$
n/N	59/5	56/5		32/3	46/3	
EPSC amplitude (nA)	6.3 ± 0.72	0.18 ± 0.05	$p < 0.0001$	7.1 ± 0.89	0.19 ± 0.03	$p < 0.0001$
n/N	48/5	49/5		31/3	42/3	
mEPSC frequency (Hz)	6.67 ± 0.72	1.48 ± 0.33	$p < 0.0001$	8.62 ± 0.92	0.72 ± 0.23	$p < 0.0001$
n/N	41/5	50/5		27/3	35/3	
Pvr (%)	6.4 ± 0.56	1.11 ± 0.3	$p < 0.0001$	8.08 ± 0.74	3.50 ± 0.63	$p < 0.0001$
n/N	57/5	54/5		32/3	43/3	
PPR	1.13 ± 0.05	1.63 ± 0.11	$p < 0.0001$	1.13 ± 0.06	1.34 ± 0.06	$p = 0.01$
n = number of cells; N= number of cultures, Values indicate mean ± SEM, Unpaired t test (Mann-Whitney test)						

Figure 4-1. Values and statistics corresponding to Figure 4.

Figure 4 A-B	ΔCre + Scr.	ΔCre + 2×10^5 IU	ΔCre + 5×10^5 IU	ΔCre + 10×10^5 IU	ΔCre + 20×10^5 IU	ΔCre + 40×10^5 IU	Cre + Scr.	test statistics
n/N	3/3	3/3	3/3	3/3	3/3	3/3	3/3	
Norm. Munc13-1/Tubulin expression	1	0.35 ± 0.09	0.25 ± 0.04	0.1 ± 0.04	0.06 ± 0.02	0.05 ± 0.02	0.30 ± 0.06	$F(6, 14) = 46.79$, $p < 0.0001$
n = number of repeats; N= number of cultures, Values indicate mean ± SEM, test: One way ANOVA								

Figure 4 C-D	ΔCre + Scr.	ΔCre + 2×10^5 IU	ΔCre + 5×10^5 IU	ΔCre + 10×10^5 IU	ΔCre + 20×10^5 IU	ΔCre + 40×10^5 IU	Cre + Scr.	test statistics
n/N	30/3	30/3	31/3	31/3	32/3	34/3	30/3	
Norm. Munc13-1/VGLUT1 expression	1 ± 0.06	0.33 ± 0.05	0.22 ± 0.02	0.12 ± 0.01	0.1 ± 0.01	0.11 ± 0.01	0.33 ± 0.03	$H = 128.2$, $p < 0.0001$
n = number of cells; N= number of cultures, Values indicate mean ± SEM, H test: Kruskal-Wallis test								

Figure 5-1. Absolute values and statistics corresponding to Figure 5.

Figure 5	ΔCre + Scr.	ΔCre + 2×10^5 IU	ΔCre + 5×10^5 IU	ΔCre + 10×10^5 IU	ΔCre + 20×10^5 IU	ΔCre + 40×10^5 IU	Cre + Scr.	test statistics
n/N	60/6	44/4	44/4	46/5	29/3	22/3	22/2	
RRP (nC)	0.42 ± 0.05	0.40 ± 0.06	0.16 ± 0.02	1.15 ± 0.03	0.12 ± 0.02	0.09 ± 0.02	0.1 ± 0.02	H = 93.2, $p < 0.0001$
n/N	60/6	44/4	44/4	46/5	29/3	22/3	22/2	
EPSC amplitude (nA)	4.17 ± 0.44	4.04 ± 0.65	1.81 ± 0.37	1.40 ± 0.30	1.04 ± 0.19	0.82 ± 0.21	0.26 ± 0.09	H = 89.7, $p < 0.0001$
n/N	51/6	42/4	39/4	40/5	29/3	20/3	17/2	
mEPSC frequency (Hz)	4.95 ± 0.65	2.50 ± 0.43	2.65 ± 0.71	1.21 ± 0.34	1.42 ± 0.27	1.0 ± 0.26	0.15 ± 0.11	H = 55.46, $p < 0.0001$
n/N	60/6	44/4	44/4	46/5	27/3	22/3	22/2	
Pvr (%)	6.74 ± 0.66	5.58 ± 0.63	5.55 ± 0.65	5.4 ± 0.70	6.40 ± 1.06	4.39 ± 0.80	0.75 ± 0.15	H = 51.42, $p < 0.0001$
n = number of cells; N= number of cultures, Values indicate mean ± SEM, H test: Kruskal-Wallis test								

Figure 6-1. Absolute values and statistics corresponding to Figure 6.

Figure 6A-G	ΔCre + Scr.	ΔCre + M13-1 KD	Cre + Scr.	Cre + M13-1 KD	Test statistics
n/N	60/5	50/5	61/5	54/5	
RRP (nC)	0.42 ± 0.04	0.08 ± 0.009	0.12 ± 0.03	0.05 ± 0.008	H = 110.3, $p < 0.0001$
n/N	72/5	60/5	72/5	63/5	
EPSC amplitude (nA)	4.06 ± 0.48	0.75 ± 0.12	0.23 ± 0.06	0.13 ± 0.04	H = 159.1, $p < 0.0001$
n/N	62/5	55/5	64/5	56/5	
mEPSC frequency (Hz)	5.34 ± 0.60	1.07 ± 0.22	0.50 ± 0.12	0.50 ± 0.34	H = 97.37, $p < 0.0001$
n/N	60/5	50/5	58/5	47/5	
Pvr (%)	6.19 ± 0.65	4.16 ± 0.44	0.8 ± 0.11	0.95 ± 0.29	H = 112.6, $p < 0.0001$
n = number of cells; N= number of cultures, Values indicate mean ± SEM, H test: Kruskal-Wallis test					

Figure 7-1. Values and statistics corresponding to Figure 7.

Figure 7A-B	ΔCre + Scr.	ΔCre + Munc13-1 KD	Cre + Scr.	Cre + Munc13-1 KD	Test statistics
n/N	31/4	28/4	29/4	23/4	
RRP ratio (Suc2/Suc1)	0.89 ± 0.03	1.33± 0.08	1.07 ± 0.08	1.45 ± 0.11	H = 69.03, $p <$ 0.0001
n = number of cells; N= number of cultures, Values indicate mean ± SEM, H test: Kruskal-Wallis test					

Figure 7C-D	Scr.	Munc13-1 KD	*p*-value
n/N	25/2	15/2	
RRP ratio (Suc2/Suc1)	0.88 ± 0.06	0.99 ± 0.11	0.6991
n = number of cells; N= number of cultures, Values indicate mean ± SEM, Unpaired t test (Mann-Whitney test)			

12. Curriculum Vitae

My curriculum vitae does not appear in the electronic version of my paper for reasons of data protection.

13. Complete list of publications

1. **Fereshteh Zarebidaki**, Marcial Camacho, Marisa M. Brockmann, Thorsten Trimbuch, Melissa A. Herman, Christian Rosenmund. Disentangling the roles of RIM and Munc13 in synaptic vesicle localization and neurotransmission (2020). *Journal of Neuroscience*. doi: 10.1523/JNEUROSCI.1922-20.2020
   Impact factor (ISI web of knowledge 2018): 6.0

2. Marisa M. Brockmann, **Fereshteh Zarebidaki**, Marcial Camacho, Katharina M. Grauel, Thorsten Trimbuch, Thomas C. Südhof, Christian Rosenmund. A trio of active zone proteins comprised of RIM-BPs, RIMs, and Munc13s governs neurotransmitter release (2020). *Cell Reports*. doi: 10.1016/j.celrep.2020.107960
   Impact factor (ISI web of knowledge 2018): 7.8

3. Jörg Malsam, Simon Bärfuss, Thorsten Trimbuch, **Fereshteh Zarebidaki**, Andreas F.-P Sonnen, Klemens Wild, Andrea Scheutzow, Lukas Rohland, Matthias P. Mayer, Irmgard Sinning, John A.G. Briggs, Christian Rosenmund, Thomas H. Söllner. Complexin suppresses spontaneous excocytosis by capturing the membrane-proximal regions of VAMP2 and SNAP25 (2020). *Cell Reports*. doi: 10.1016/j.celrep.2020.107926
   Impact factor (ISI web of knowledge 2018): 7.8

14. Acknowledgements

First and foremost, I would like to express my deep and sincere gratitude to my doctoral supervisor *Prof. Christian Rosenmund* for giving me the opportunity to do research in his laboratory. The accomplishments of this project could not be achieved without the inputs from my advisor. His continuous support, guidance, and mentoring was very enlightening and helpful for all phases of my PhD in the laboratory.

I would also like to thank my co-supervisor *Dr. Marcial Camacho* for fruitful discussions on my PhD project and experiments, and for his rigorous and attentive support during the writing and revision of my manuscript. Special thanks to my other co-supervisor *Dr. Marisa Brockmann* for mentoring me during my PhD in the lab and for introducing me to interesting projects that expanded my knowledge.

I am also very grateful to all of my colleagues and friends in Rosenmund lab for their support and inputs during the lab meetings. Special thanks to my kind friends and colleagues *Andrea Salazar Lázaro*, *Foteini Paraskevopoulou*, and *Boris Bouazza Arostegui* for their heart-warming support and warm hugs.

Without the technical support I could not easily make progress with my PhD project. I would like to express my sincere thanks to all the technical support from *Berit Söhl-Kielczynski*, *Bettina Brokowski*, *Katja Pötschke, Rike Dannenberg*, *Miriam Petzold*, *Heike Lerch*, and *Sabine Lenz*.

I would also like to thank the MedNeuro PhD program for offering the opportunity to take part in the program.

I would like to express my gratitude to my family for their unconditional love throughout my life. My studies would not have been possible without the emotional support from my *mother, father*, *sister*, and *brothers*.

Last but not least, I would like to thank my life partner *Soheil Hajian* for standing by my side and for his kindness, patience, and support in the most difficult times and in happiness.